

Middle East Journal of Science

www.dergipark.org.tr/mejs

MEJS

VOLUME 8

ISSUE 1

JUNE

2022

E-ISSN

2618-6136



Copyright © 2022

Email : bilgumus@gmail.com

Visit our home page on www.dergipark.org.tr/mejs

MEJS is an open access journal. This journal licensed under creative common 4.0 International (CC BY 4.0) license. You are free to share and adapt for any purpose, even commercially.

Under the following terms:

Attribution — You must give appropriate credit, provide a link to the license, and indicate if changes were made. You may do so in any reasonable manner, but not in any way that suggests the licensor endorses you or your use.

No additional restrictions — You may not apply legal terms or technological measures that legally restrict others from doing anything the license permits.

Notices:

You do not have to comply with the license for elements of the material in the public domain or where your use is permitted by an applicable exception or limitation.

No warranties are given. The license may not give you all of the permissions necessary for your intended use. For example, other rights such as publicity, privacy, or moral rights may limit how you use the material.



Editor-in-Chief

Zülküf GÜLSÜN

Atomic and Molecular Physics, NMR Spectroscopy
(Prof.Dr., General Director of INSERA, Dicle Teknokent, Dicle University, Diyarbakır, TURKEY))
zulkufgulsun@gmail.com

Language Editor

Dr. Mustafa BULUT

Dicle University Vocational School, Diyarbakır/TURKEY
mbulut@dicle.edu.tr

Co-Editor

Bilal GÜMÜŞ

Dicle University Faculty of Engineering, Dep. of Electrical and Electronics Engineering, Diyarbakır/TURKEY
bilgumus@dicle.edu.tr

Members of Editorial Board and their fields

Abdülkadir MASKAN

Field: Physics Education, Science Education

(Prof.Dr., Dicle University, Faculty of Education, Turkey) akmaskan@dicle.edu.tr

Abduselam ERTAŞ

Field: Natural products, Pharmacognosy (Assoc.Prof.Dr., Dicle University, Faculty of Pharmacy, Department of Pharmacognosy, Turkey) abduselamertas@hotmail.com

Abdullah SESSİZ

Field: Agricultural Machinery and Technologies Engineering

(Prof.Dr., Dicle University, Faculty of Agriculture, Turkey) asesiz@dicle.edu.tr

Ahmad ALI

Field: Biotechnology, DNA Extraction, Molecular Biology, Lifesciences

(PhD., University of Mumbai, Dep. of Life Sciences, Mumbai, INDIA) ahmadali@mu.ac.in

Ahmet ALTINDAL

Field: Condensed Matter Physics, Electronic Structure, Thin Films and Low-Dimensional Structures

(Prof.Dr., YILDIZ Technical University, Faculty of Arts and Sciences, Turkey) altindal@yildiz.edu.tr

Ahmet ONAY

Field: Botany, General Biology

(Prof.Dr., Dicle University, Faculty of Science, Dep. of Biology, Turkey) ahmeto@dicle.edu.tr

Alexander PANKOV

Field: Partial Differential Equations, Nonlinear Analysis and Critical Point Theory, Mathematical Physics, Applied Mathematics

(Prof.Dr., Morgan State University, USA) alexander.pankov@morgan.edu

Ali YILMAZ

Field: Atomic and Molecular Physics, Biophysics, NMR Spectroscopy

(Prof.Dr., Retirad, Turkey) yilmz.ali@gmail.com

Arun Kumar Narayanan NAIR

Field: Polymer Chemistry, Computer Simulation

(PhD., King Abdullah University of Science and Technology, Saudi Arabia) anarayanannair@gmail.com

Azeez Abdullah BARZINJY

Field: Material Science, Physics

(Associate Prof.Dr., Materials Science, Department of Physics, Salahaddin University, IRAQ)

azeez.azeez@su.edu.krd

Bayram DEMİR

Field: Nuclear Physics, Nuclear Medicine, Medical Imaging

(Prof.Dr., İstanbul University, Faculty of Science, Turkey) bayramdemir69@yahoo.com

Birol OTLUDİL

Field: General Biology, Pharmaceutical Biology, Science Education

(Prof.Dr., Dicle University, Faculty of Education, Turkey) birolotludil@dicle.edu.tr

Enver SHERIFI

Field: Herbolgy, Biology, Agricultural Science

(Prof.Dr., University of Prishtina, Kosovo) e_sherifi@yahoo.com

Feyyaz DURAP

Field: Inorganic Chemistry

(Prof.Dr., Dicle University, Faculty of Science, Dep. of Chemistry, TURKEY) fdurap@dicle.edu.tr

Gültekin ÖZDEMİR

Field: Agricultural Science, Horticulture

(Prof.Dr., Dicle University, Faculty of Agriculture, Department of Horticulture, Turkey) gozdemir@gmail.com

Hamdi TEMEL

Field: Pharmaceutical Chemistry

(Prof.Dr., Dicle University, Fac. of Pharmacy, Dep. of Pharmaceutical Chemistry, Turkey)

htemelh@hotmail.com

Hasan Çetin ÖZEN

Field: Botany, General Biology

(Prof.Dr., Dicle University, Faculty of Science, Dep. of Biology, Turkey) hasancetino@gmail.com

Hasan İÇEN

Field: Veterinary Internal Disease

(Prof.Dr., Dicle University, Faculty of Veterinary, Dep. of Internal Disease, TURKEY) hasanicen@dicle.edu.tr

Hasan KÜÇÜKBAY

Field: Organic Chemistry, Peptide Chemistry, Heterocyclic Chemistry, Medicinal Chemistry

(Prof.Dr., İnönü University, Faculty of Science and Letters, Dep. of Chemistry, Turkey)

hkucukbay@gmail.com

Hadice Budak GÜMGÜM

Field: Atomic and Molecular Physics, NMR Spectroscopy

(Prof.Dr., Dicle University, Faculty of Science, Dep. of Physics, TURKEY) hbudak@gmail.com

Hüseyin ALKAN

Field: Protein Separation Techniques, Pharmacy

(Assoc.Prof.Dr., Dicle University Faculty of Pharmacy, Department of Biochemistry, TURKEY)

mhalkan@dicle.edu.tr

Ishtiaq AHMAD

Field: Numerical Analysis, Computer Engineering

(PhD., Austrian Institute of Technology, Austria) ishtiaq.ahmad.fl@ait.ac.at

İlhan DAĞADUR

Field: Mathematics, Analysis and Functions Theory

(Prof.Dr., Mersin University Faculty of Arts and Sciences, Dep. of Mathematics, Turkey)

ilhandagdur@yahoo.com; idagadur@mersin@edu.tr

İsmail YENER

Field: Analytical Techniques, Pharmacy

(PhD., Dicle University, Faculty of Pharmacy, Department of Analytical Chemistry, Turkey)

ismail.yener@dicle.edu.tr

Javier FOMBONA

Field: Science Education

(Prof.Dr., University of Oviedo, Spain) fombona@uniovi.es

Jonnalagadda Venkateswara RAO

Field: Algebra, General Mathematics

(Prof.Dr., School of Science & Technology, United States International University, Nairobi, KENYA)

drjvenkateswararao@gmail.com

Lotfi BENSAPHLA-TALET

Field: Ecology, Hydrobiology

(Assoc. Prof.Dr., Department of Biology, Faculty of Natural Sciences and Life, University Oran1-Ahmed

BENBELLA, Algeria) btlotfi1977@gmail.com

M.Aydın KETANİ

Field: Veterinary, Histology and Embryology

(Prof.Dr., Dicle University, Fac. of Veterinary, Dep. of Histology and Embryology, TURKEY)

Mohammad ASADI

Field: Agriculture, Entomology, Pesticides toxicology

(Dr., Department of Plant Protection, Faculty of Agriculture and Natural Resources,

University of Mohaghegh Ardabili, Ardabil, IRAN) assadi20@gmail.com

Mukadder İĞDİ ŞEN

Field: Astronautics Engineering

(Dr., Trakya University, Edirne Vocational College of Technical Sciences, Turkey)

mukaddersen@trakya.edu.tr

Murat AYDEMİR

Field: Inorganic Chemistry

(Prof.Dr., Dicle University, Faculty of Science, Dep. of Chemistry, TURKEY) aydemir@dicle.edu.tr

Murat HÜDAVERDİ

Field: High Energy and Plasma Physics

(Dr., Yıldız Technical University, Faculty of Science and Letters, Dep. of Physics, TURKEY)

hudaverd@yildiz.edu.tr

Müge SAKAR

Field: General Mathematics

(Assoc.Prof.Dr., Dicle University, Turkey) mugesakar@hotmail.com

Mustafa AVCI

Field: General Mathematics

(Assoc.Prof.Dr., Batman University, Turkey) mustafa.avci@batman.edu.tr

Nuri ÜNAL

Field: High Energy and Plasma Physics

(Retired Prof.Dr., Akdeniz University, Faculty of Science, Turkey) nuriunal@akdeniz.edu.tr

Özlem GÜNEY

Field: Mathematics, Analysis and Functions Theory

(Prof.Dr., Dicle University, Faculty of Science, Dep. of Mathematics, Turkey) ozlemg@dicle.edu.tr

Petrica CRISTEA

Field: Computational Physics, Condensed Matter Physics, Electromagnetism

(Assoc.Prof.Dr., University of Bucharest, Faculty of Physics, Romania) pcristea@fizica.unibuc.ro

Sanaa M. AL-DELAIMY

Field: Atomic and Molecular Physics, General Physics

(Ph.D., Physics Department, Education College for Pure Sciences, Mosul University, Mosul, Iraq)

sadelaimy@yahoo.com

Selahattin GÖNEN

Field: Physics Education, Science Education

(Prof.Dr., Dicle University, Faculty of Education, Turkey) sgonen@dicle.edu.tr

Şemsettin OSMANOĞLU

Field: Atomic and Molecular Physics, ESR Spectroscopy

(Retired Prof.Dr., Dicle University, Faculty of Science, Dep. of Physics) sems@dicle.edu.tr

Sezai ASUBAY

Field: Solid State Physics

(Prof.Dr., Dicle University, Faculty of Science, Dep. of Physics, Turkey) sezai.asubay@gmail.com

Süleyman DAŞDAĞ

Field: Biophysics

(Prof.Dr., İstanbul Medeniyet University, Faculty of Medicine, Dep. of Biophysics, Turkey)

sdasdag@gmail.com

Tamraz H. TAMRAZOV

Field: Biological Sciences

(Assoc.Prof.Dr., Department of Plant Physiology and Biotechnology, Research Institute of Crop Husbandry,
Ministry of Agriculture of the Republic of Azerbaijan)

tamraz.tamrazov@mail.ru

Yusuf ZEREN

Field: Mathematics, Topology

(Assoc.Prof.Dr., Yıldız Technical University, Faculty of Science and Letters, Dep. of Mathematics, TURKEY)

yzeren@yildiz.edu.tr

Z. Gökay KAYNAK

Field: Nuclear Physics

(Retired Prof.Dr., Uludag University, Faculty of Science, Dep. of Physics, Turkey) kaynak@uludag.edu.tr



CONTENTS

Research Articles

- 1- NOVEL MONONUCLEAR METAL-PHOSPHINITE COMPOUNDS AND THEIR CATALYTIC PERFORMANCE IN TRANSFER HYDROGENATION OF KETONES.....1-15
Uğur Işık, Nermin Meriç, Murat Aydemir
- 2 - DFT INVESTIGATION OF TRANSITION METALS ARENE COMPOUNDS WITH FUNCTIONALIZED IONIC LIQUID 16-25
Nermin MERİÇ, Nil ERTEKİN BINBAY, Cezmi KAYAN, Veysel BINBAY, Murat AYDEMİR
- 3- REVERSE-ENGINEERED DBI-ESSENCE FIELD IN THE RAINBOW GRAVITY..... 26-33
Fatma Figen BİNBAŞ
- 4- CHARACTERIZATION OF CU₂MNSNS₄ THIN FILMS FABRICATED BY SPIN COATING.. 34-45
Canan AYTUĞ AVA, Şilan BATURAY
- 5- EXPRESSION PATTERN OF BK CHANNELS UNDER VARIOUS OXIDATIVE STRESS CONDITIONS IN SKELETAL MUSCLES 46-55
Cağır COSKUN, Figen A. CİCEK, Onur TOKGÜN, Isıl OCAK
- 6- INVESTIGATION OF GLOBOZOOSPERMIA'S MORPHOLOGICAL STRUCTURE AND DNA FRAGMENTATION IN OLIGOZOOSPERMIA CASES IN INFERTILE MALES 56- 63
Zuhal ÇANKIRI, Murat AKKUŞ, Eda YILDIZHAN, Dilara AKINCI, Fırat AŞIR, Onur DEDE, Muhamet AFŞİN
- 7- MODELLING OF THE SOLAR CELL BASED ON CU₂SNS₃ THIN FILM PRODUCED BY SPRAY PYROLYSIS64-76
Serap YIGİT GEZGIN, İlhan CANDAN, Silan BATURAY, Hamdi Sukur KILIC

**NOVEL MONONUCLEAR METAL-PHOSPHINITE COMPOUNDS AND THEIR CATALYTIC PERFORMANCE IN TRANSFER HYDROGENATION OF KETONES**Uğur IŞIK¹  Nermin MERİÇ¹  Murat AYDEMİR*¹ ¹Dicle University, Science Faculty, Department of Chemistry, 21280-Diyarbakır, Turkey*Corresponding author: aydemir@dicle.edu.tr

Abstract: Since the obtained chiral alcohols are rather useful as well as biologically active compounds, the reduction of ketones to their respective alcohols is a crucial topic in synthetic chemistry. Thus, a new phosphinite ligand was synthesized by the interaction of cationic species *N*-vinyl imidazolium (**1**) with PCy₂Cl. This phosphinite ligand in combination with [Ru(η^6 -*p*-cymene)(μ -Cl)Cl]₂ and Ir(η^5 -C₅Me₅)(μ -Cl)Cl]₂ gave active catalytic systems for transfer hydrogenation reaction. Under optimum circumstances, ruthenium complex (**3**) showed rather a high conversion in the reduction reaction of acetophenone. Furthermore, reversibility of the transfer hydrogenation reaction was found to be low under these reaction circumstances.

Keywords: Transfer Hydrogenation; Ruthenium Complex; Iridium Complex; Phosphinite; Homogeneous Catalysis.

Received: February 23, 2022

Accepted: April 05, 2022

1. Introduction

Phosphino-imidazolium salts were first designed by Chauvin and Canac to prepare transition metal complexes having ionic character [1,2], and when used in homogeneous catalytic reactions by Zhao et al., [3-6] these complexes exhibited a high activity [7,8]. Afterward, the synthesis and applications of phosphinite-imidazolium salts have also become an effective field of study. Phosphinite-imidazolium salts were used as catalysts in the preparation of phthalate and maleate diesters, 3,4-dihydropyrimidin-2(1H)-(thio)ones, *E*-cinnamates, and coumarin derivatives by Valizadeh et al. [9-12]. Iranpoor et al., using these compounds, investigated the catalytic efficiency of aryl halides in dehalogenation, silylation, and Heck reactions in the presence of PdCl₂ [13-15]. However, the application of complexes of phosphinite compounds based on the ionic liquid in asymmetric transfer hydrogenation reaction was first performed by our study group [16-18].

The reduction of carbonyl compounds using a catalyst, and dihydrogen (H₂), hydrides, or H₂-donors as a source of hydrogen is an important route to obtaining alcohols [19-21]. In molecular hydrogenation, dihydrogen is used as a hydrogenation source, while hydrides are used in metal hydride reduction, and a hydrogen donor is used in transfer hydrogenation. It has shown that transfer hydrogenation is more advantageous than the conventional use of hydrides or direct hydrogen. Among them are (a) equipment is simpler; (b) catalyst loading is lower; (c) handling is safer; (d) solvents are environmentally friendly; (e) by-products are facile removable and volatile; and (f) the process may be used in industrial processes [22,23]. In this reaction, hydrogen is transferred from an organic source (e.g. isopropanol or formic acid) to an unsaturated bond of a compound (e.g. ketone or alkene), a metal is

used as a catalyst, often a base is also required [24]. Metal catalysts such as transition metal complexes (Ru, Ir, or Rh) containing phosphinites displayed high catalytic activity and became the most common organometallic compound employed in the transfer hydrogenation reaction [25-32].

Continuing our previous research, the present study reports the synthesis of an imidazole containing ionic liquid (IL) via the regioselective epoxide ring-opening reaction. The ionic liquid (IL) was converted to the corresponding chiral functionalized ionic liquid-based phosphinite ligand (P-FIL) by adding phosphinite moiety to the ionic liquid through S_N2 reaction, and then the corresponding Ru(II) and Ir(III) transition metal complexes were prepared. Structures of all new compounds were elucidated by ^{31}P , ^1H , ^{13}C NMR, and FT-IR spectroscopies. Afterward, the application of Ru(II) and Ir(III) compounds as catalysts were investigated in the transfer hydrogenation (TH) of acetophenone derivatives to their respective 1-phenylethanol derivatives using isopropanol as a hydrogen source.

2. Materials and Methods

2.1. Materials

If it is not stated otherwise, materials and solvents were employed as received. The reactants 1-vinylimidazole (99%), chlorodicyclohexylphosphine (97%) (PCy_2Cl), n-butyllithium solution (1.6 M in hexane; n-BuLi), (\pm)-epichlorohydrin (99%), dichloro(*p*-cymene)ruthenium(II) dimer, $[\text{Ru}(\eta^6\text{-p-cymene})(\mu\text{-Cl})\text{Cl}]_2$ (99%) and pentamethylcyclopentadienyliridium(III) chloride, dimer, $\text{Ir}(\eta^5\text{-C}_5\text{Me}_5)(\mu\text{-Cl})\text{Cl}]_2$ were purchased from Sigma-Aldrich (Germany). The phosphinite ligand and their complexes were prepared under an inert atmosphere employing standard Schlenk techniques. CaH_2 was used to dry 2-propanol. A Bruker AV400 spectrometer was used to record ^1H , ^{13}C and, ^{31}P - $\{^1\text{H}\}$ nuclear magnetic resonance (NMR) spectra. An Agilent Cary 630 Fourier Transform infrared spectrometer was used to obtain the infrared spectra. A Costech ECS 4010 instrument was used to conduct elemental analysis. Melting points of the products were obtained by means of a Stuart SMP40 apparatus with an open capillary. GC analysis was conducted with a Shimadzu GC 2010 Plus instrument equipped with cyclodex B (Agilent) capillary column (5% biphenyl, 95% dimethylsiloxane; 30 m \times 0.32 mm \times 0.25 μm).

2.2. GC analyses

The GC parameters for TH of acetophenone derivatives are given below; init. temp., 50 $^\circ\text{C}$; init. time, 1.1 min; solv. del., 4.48 min; temp. ramp 15 $^\circ\text{C}/\text{min}$; ending temp., 270 $^\circ\text{C}$; hold time, 5 min; last time, 20.76 min; inj. port temp., 200 $^\circ\text{C}$; det. temp., 200 $^\circ\text{C}$; inj. vol., 2.0 μL .

2.3. A general protocol for the catalytic hydrogen transfer reaction

A representative protocol for TH of ketones is given below: a solution of pre-catalysts (**3-4**) (0.005 mmol), potassium hydroxide (0.025 mmol), and respective ketone (0.5 mmol) in isopropanol that was degassed (5 mL) was heated to reflux until the reactions finished. Then, a specimen was taken from this medium, followed by dilution with acetone and analyzing immediately by GC. The conversions are calculated depending on the remaining ketone. ^1H NMR spectra of the resulting products were as anticipated.

2.4. Preparation and structure elucidation of compounds

2.4.1 Preparation of 3-(3-chloro-2-hydroxypropyl)-1-vinyl-1H-imidazol-3-ium chloride, (1)

Concentrated HCl (10.50 mL, 128 mmol) was cautiously added into an ethanol (20 mL) solution of 1-vinylimidazole (11.30 mL, 11.764 g, 125 mmol), which was stirred at ambient temperature. **Warning:** *The neutralization of a base with a strong acid is rather exothermic.* Having added acid, it

was pending until the medium cooled to ambient temperature. Then, the addition of (\pm)-epichlorohydrin (10.16 mL, 12.027 g, 130 mmol) was carried out dropwise by stirring the solution, meanwhile, temperature of the solution was kept at 25 °C. Afterward, the reaction flask was closed and stirred at ambient temperature for 24 – 48 hours. Then, removal of the solvent of the solution in vacuo with warming at 70 °C, and keep warming under reduced pressure afforded a liquid that became more viscous when dried further, which was then recrystallized from ethyl acetate at 0 °C. The precipitated solid part was filtered and dried under reduced pressure giving **1** as an off-white solid. Yield 27.22 g, 97.6 %, Melting Point = 99-101 °C. **¹H NMR (400.1 MHz, DMSO-*d*₆, ppm):** δ : 9.46 (s, 1H, $-\text{NCHN}^+$), 8.19 and 7.85 (2xs, 2H, $-\text{NCHCHN}^-$), 7.35-7.29 (m, 1H $-\text{CH}=\text{CH}_2$), 6.05 (br, 1H, $-\text{CHOH}$), 5.98-5.94 (m, 1H, $-\text{CH}=\text{CH}_2$ (a)), 5.44-5.40 (m, 1H, $-\text{CH}=\text{CH}_2$ (b)), 4.42-4.39 (m, 1H, $-\text{N}^+\text{CH}_2$ (a)), 4.20-4.15 (m, 1H, $-\text{N}^+\text{CH}_2$ (b)), 4.10 (br, 1H $-\text{CHOH}$), 3.45 (m, 2H, $-\text{CH}_2\text{Cl}$); **¹³C NMR (100.6 MHz, DMSO-*d*₆, ppm):** δ 136.43 ($-\text{NCHN}^+$), 129.22 ($-\text{NCH}=\text{CH}_2$), 124.46, 119.20 ($-\text{NCHCHN}^-$), 109.21 ($-\text{NCH}=\text{CH}_2$), 68.86 ($-\text{CHOH}$), 52.99 ($-\text{N}^+\text{CH}_2\text{CH}(\text{OH})$), 46.91 ($-\text{CH}_2\text{Cl}$); **IR (cm⁻¹):** ν 3369 (O-H), 3116, 3041 (aromatic C-H), 2989, 2888 (aliphatic C-H), 1575 (C=N), 1162 (C-N) cm⁻¹; Analysis results for **C₈H₁₂Cl₂N₂O** (223.10g/mol): calcd. C 43.07, H 5.42, N 12.56; found C 42.98, H 5.36, N 12.51.

2.4.2 Preparation of 3- (3-chloro-2-((dicyclohexylphosphanyl)oxy)propyl)-1-vinyl-1H-imidazol-3-ium chloride, (2)

A CH₂Cl₂ (20 mL) solution of **1** (0.105 g, 0.47 mmol) under an inert atmosphere was cooled to -78 °C in an acetone and dry ice bath. A hexane solution of *n*-BuLi (0.293 mL, 0.47 mmol) was added dropwise into this cooled solution. Followed by the addition, the solution was stirred at -78 °C for 1 h and further 45 minutes at room temperature (RT). Afterward, the reaction solution was cooled to -78 °C again and a solution of dicyclohexylchlorophosphine (0.112 g, 0.47 mmol) in CH₂Cl₂ (10 mL) was added dropwise to this solution, which was stirred for a further 1 h at -78 °C. Having removed the cooling bath, the solution was further stirred for 3 hours at RT and ³¹P NMR spectroscopy was used to follow the progress of the reaction. After ligand formation was observed, removal of the precipitated lithium chloride was performed by filtration under an inert atmosphere, followed by removal of the volatiles in vacuo, which gave a viscous oil phosphinite ligand, **2**. **³¹P-¹H NMR (162.0 MHz, CDCl₃, ppm):** δ 148.99 (s, OPCy₂).

2.5. General protocol for the synthesis of (IL-OPCy₂-Metal) complexes

Metal precursor (0.40 mmol) and [(Cy₂P)-C₈H₁₁Cl₂N₂O], **2** (0.40 mmol) were dissolved in dried CH₂Cl₂ (25 mL) under an inert atmosphere, and then this mixture was stirred for 1 h at RT. The volume of the solution was reduced to 1-2 mL in vacuo, and petroleum ether (15 mL) was added to afford the respective metal complexes as microcrystalline solid. This solid was separated by filtrating the mixture and dried under reduced pressure.

2.5.1 [3-(3-chloro-2-({dichloro(η^6 -*p*-cymene)ruthenium]dicyclohexylphosphanyl)oxy) propyl)-1-vinyl-1H-imidazol-3-ium chloride], (3)

Yield: 280 mg, 96.5%; Melting point: 113-115 °C. **¹H NMR (400.1 MHz, DMSO-*d*₆, ppm):** δ : 9.59 (s, 1H, $-\text{NCHN}^+$), 8.25, 7.91 (2xs, 2H, $-\text{NCHCHN}^-$), 7.40-7.34 (m, 1H, $-\text{CH}=\text{CH}_2$), 5.99 (br, 1H, $-\text{CH}=\text{CH}_2$ (a)), 5.83-5.79 (m, 4H, aromatic protons of *p*-cymene), 5.43 (br, 1H, $-\text{CH}=\text{CH}_2$ (b)), 5.41 (br, 1H, $-\text{CHOP}$), 4.43 (d, 1H, $J=13.23$ Hz, $-\text{N}^+\text{CH}_2$ (a)), 4.19 (d, 1H, $J=13.61$ Hz, $-\text{N}^+\text{CH}_2$ (b)), 3.69 (m, 2H, $-\text{CH}_2\text{Cl}$), 2.84-2.81 (m, 1H, $-\text{CH}(\text{CH}_3)_2$ of *p*-cymene), 2.46 (m, 2H, $-\text{CH}$ of P(C₆H₁₁)₂), 2.08 (s, 3H, $-\text{CH}_3\text{Ph}$ of *p*-cymene), 1.78 + 1.23-1.18 (m, 26H, (CH₃)₂CH Ph of *p*-cymene + CH₂ of P(C₆H₁₁)₂); **¹³C NMR (100.6 MHz, DMSO-*d*₆, ppm):** δ : 136.63 ($-\text{NCHN}^+$), 129.35 ($-\text{NCH}=\text{CH}_2$), 119.20, 124.54 ($-\text{NCHCHN}^-$), 109.10 ($-\text{NCH}=\text{CH}_2$), 106.80, 100.53 (quaternary carbons of *p*-cymene), 86.83, 85.98 (s, aromatic carbons of *p*-cymene), 73.25 (d, $J_{P-C}=6.0$ Hz $-\text{CHOP}$), 53.01 ($-\text{CH}_2\text{Cl}$).

$N^+CH_2CH(OP)$, 46.91 ($-CH_2Cl$), many resonances at between 46.08-45.44 for $-CH$ of $P(C_6H_{11})_2$, 30.43 ($-CH(CH_3)_2$ of *p*-cymene), many signals at between 28.31-26.11 for $-CH_2$ of $P(C_6H_{11})_2$, 21.96 ($-CH(CH_3)_2Ph$ of *p*-cymene), 18.33 ($-CH_3Ph$ of *p*-cymene); $^{31}P\{-^1H\}$ NMR (162.0 MHz, $CDCl_3$, ppm) δ : 156.01 (s, $OPCy_2$); $^{31}P\{-^1H\}$ NMR (162.0 MHz, $DMSO-d_6$, ppm) δ : 158.20 (s, $OPCy_2$); IR (cm^{-1}); ν 3041 (aromatic C-H), 2922, 2851 (aliphatic C-H), 1446 (P-Cy), 1054 (O-P), 533 (Ru-P); **Analytical results for $C_{30}H_{47}Cl_4N_2OPRu$ (725.56 g/mol)**: calcd. C 49.66, H 6.53, N 3.86; found C 49.60; H 6.478; N 3.78 %.

2.5.2 [3-(3-chloro-2-({dichloro(η^5 -pentamethylcyclopentadienyl) iridium] dicyclohexyl phosphanyl)oxy)propyl)-1-vinyl-1H-imidazol-3-ium chloride], (4)

Yield: 310 mg, 94.7 %; m.p.: 124–126 °C; 1H NMR (400.1 MHz, $DMSO-d_6$, ppm): δ : 9.53 (s, 1H, $-NCHN^+$), 8.31, 7.76 (2xs, 2H, $-NCHCHN^+$), 7.39 (br, 1H, $-CH=CH_2$), 6.02 (br, 1H, $-CH=CH_2(a)$), 5.58 (br, 1H, $-CHOP$), 5.41 (br, 1H, $-CH=CH_2(b)$), 3.87 (m, 1H, $-N^+CH_2(a)$), 3.78 (m, 1H, $-N^+CH_2(b)$), 4.49 (br, 2H, $-CH_2Cl$), 1.53 (s, 15H C_5Me_5), 1.98-1.23 (m, 22H, protons of $P(C_6H_{11})_2$); ^{13}C NMR (100.6 MHz, $DMSO-d_6$, ppm): δ : 136.6 ($-NCHN^+$), 129.35 ($-NCH=CH_2$), 124.06, 119.63 ($-NCHCHN^+$), 109.19 ($-NCH=CH_2$), 93.92 (s, C_5Me_5), 73.99 (d, $J_{P-C}=6.0$ Hz, $-CHOP$), 50.02 ($-N^+CH_2CH(OP)$), 45.70 ($-CH_2Cl$), many resonances at between 44.28-43.73 for $-CH$ of $P(C_6H_{11})_2$, many signals at between 28.76-25.54 for $-CH_2$ of $P(C_6H_{11})_2$, 9.45 (C_5Me_5); $^{31}P\{-^1H\}$ NMR (162.0 MHz, $CDCl_3$, ppm) δ : 122.92 (s, $OPCy_2$); $^{31}P\{-^1H\}$ NMR (162.0 MHz, $DMSO-d_6$, ppm) δ : 123.03 (s, $OPCy_2$); IR (cm^{-1}); ν 3097 (aromatic C-H), 2922, 2847 (aliphatic C-H) 1446 (P-Cy), 1058 (O-P); **Analytical results for $C_{30}H_{48}Cl_4N_2OPIr$ (817.72 g/mol)**: calcd.: C 44.07; H 5.92; N 3.43; found C 44.01; H 5.82; N 3.37 %

3. Results and Discussion

3.1. Synthesis and characterization of the ionic liquid, phosphinite ligand, and corresponding complexes

One of the most common techniques for the preparation of hydroxyl-functionalized ionic liquid is the ring-opening of epoxides. Based on this method [33-40], *N*-vinylimidazole was reacted with (\pm)-epichlorohydrin to afford the corresponding functionalized ionic liquid in 97.6 % isolated yield (Scheme 1). The initial formation of a new generation of desired ionic liquid 3-(3-chloro-2-hydroxypropyl)-1-vinyl-1H-imidazol-3-ium chloride, (**1**) was unambiguously confirmed by their spectroscopic analysis. In the 1H NMR spectrum of compound **1**, the $-NCHN^+$ signal of the starting material *N*-vinylimidazole at δ 7.98 ppm shifted to 9.46 ppm due to the formation of the corresponding ionic liquid **1**, which was in agreement with the literature [41,19,42,18 and references therein]. The signal for extra OH proton was observed at around 6.05 (br) ppm, which is good evidence of the success of the alkylation of the imidazole ring with (\pm)-epichlorohydrin. The remaining protons were observed in their respective regions. The $^{13}C\{-^1H\}$ NMR spectrum of (**1**) also shows the presence of the *N*-vinylimidazolium carbons at δ 136.43, 129.22, 124.46, 119.20, and 109.21 ppm. In addition, the signal at 68.86 ppm belongs to $-CHOH$, which is another evidence that the ring-opening reaction has occurred. In the IR spectrum, the signal of the hydroxyl group was observed as expected. Moreover, the elemental analysis result of **1** supports the formation of the compound.

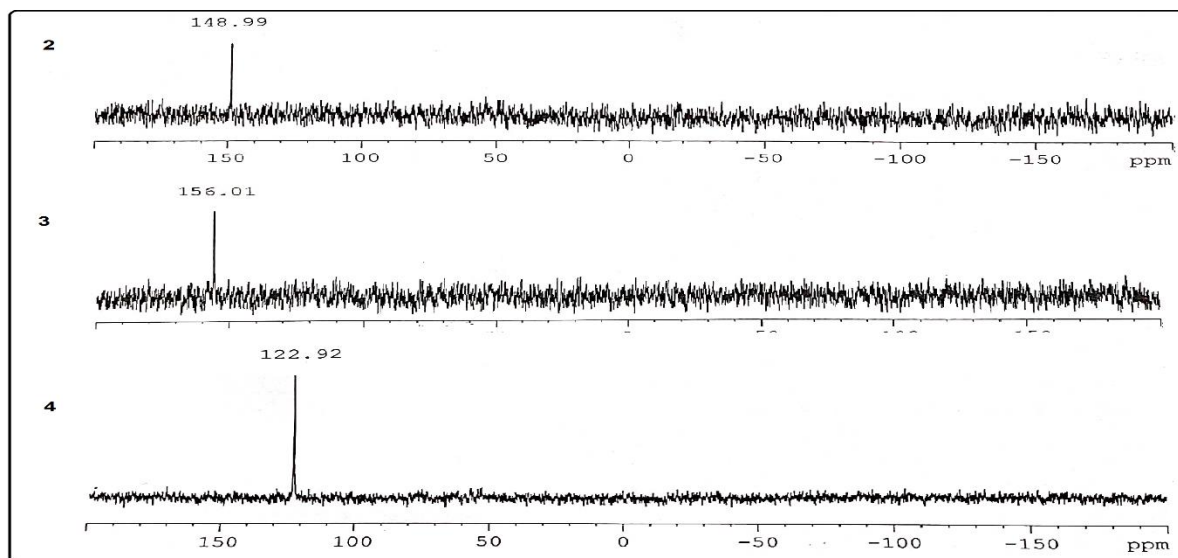
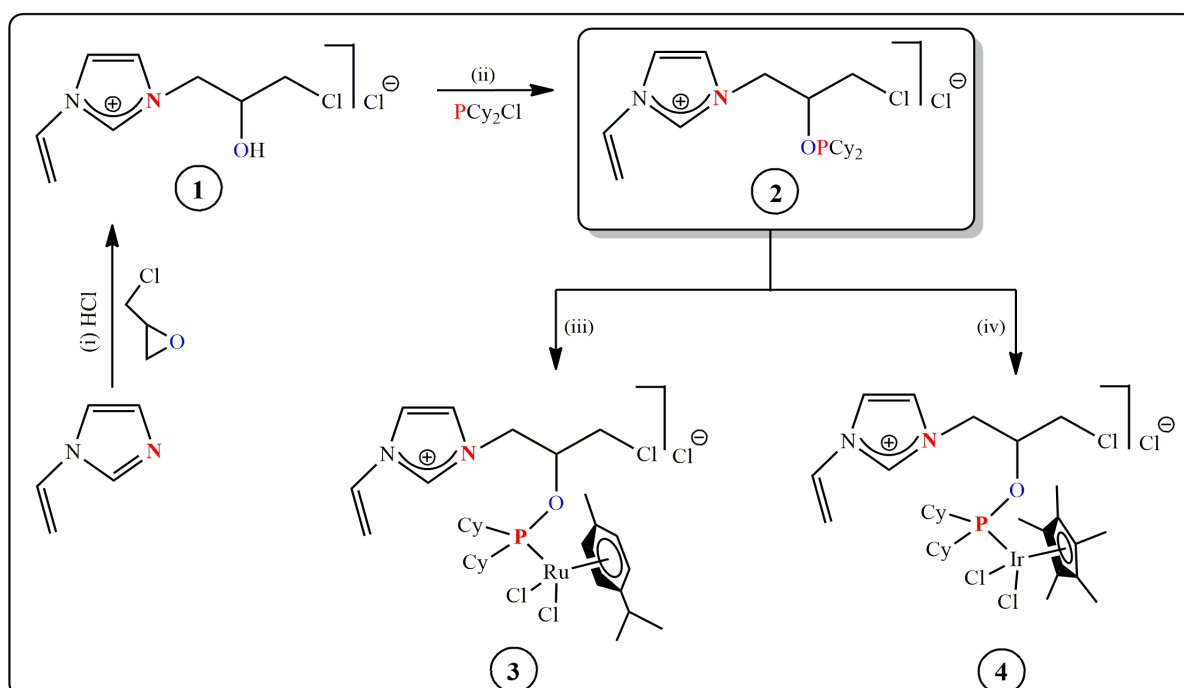


Figure 3. The $^{31}\text{P}\{-^1\text{H}\}$ NMR spectra of ligand (2) and its complexes (3 and 4),



Scheme 1. Synthesis of compounds **1-4**; (i) 1 equiv. (\pm)-Epichlorohydrin, 1 equiv. HCl, $\text{C}_2\text{H}_5\text{OH}$; (ii) 1 equiv. Cy_2PCl , 1 equiv. $n\text{-BuLi}$, CH_2Cl_2 ; (iii) 1/2 equiv. $[\text{Ru}(\eta^6\text{-}p\text{-cymene})(\mu\text{-Cl})\text{Cl}]_2$; (iv) 1/2 equiv. $[\text{Ir}(\eta^5\text{-C}_5\text{Me}_5)(\mu\text{-Cl})\text{Cl}]_2$, CH_2Cl_2 .

The synthetic procedure to prepare the cyclohexyl-containing phosphinite ligand [17,42,43] is shown in Scheme 1. The reaction of the ionic liquid **1** with 1 equiv. of $n\text{-BuLi}$ in CH_2Cl_2 at -78°C for 1 h, and then the addition of 1 equiv. of ClPCy_2 produced phosphinite ligand 3-(3-chloro-2-((dicyclohexylphosphaneyl)oxy)propyl)-1-vinyl-1H-imidazol-3-ium chloride, (**2**). The ^{31}P NMR characterization of the crude reaction presented a signal at δ 148.99 ppm (singlet) attributed to $-\text{OPCy}_2$.

Our result agrees with the values for previously reported phosphinites [44-47] (Fig. 1). Unfortunately, although ligand **2** was clearly present in the crude reaction mixture, it could not be isolated sufficiently pure for characterization studies. Because the phosphinite ligand decomposes gradually to give oxide ~ 44 ppm as singlet ($-\text{OP}(\text{O})\text{Cy}_2$). Furthermore, doublet signals at about $\delta 57.7$ ppm and at $\delta -20.1$ ppm having $^1J_{\text{PP}}$: 285 Hz in the $^{31}\text{P}\{-^1\text{H}\}$ NMR spectrum support the occurrence of $\text{P}(\text{O})\text{Cy}_2\text{PCy}_2$ [48] (Fig. 2).

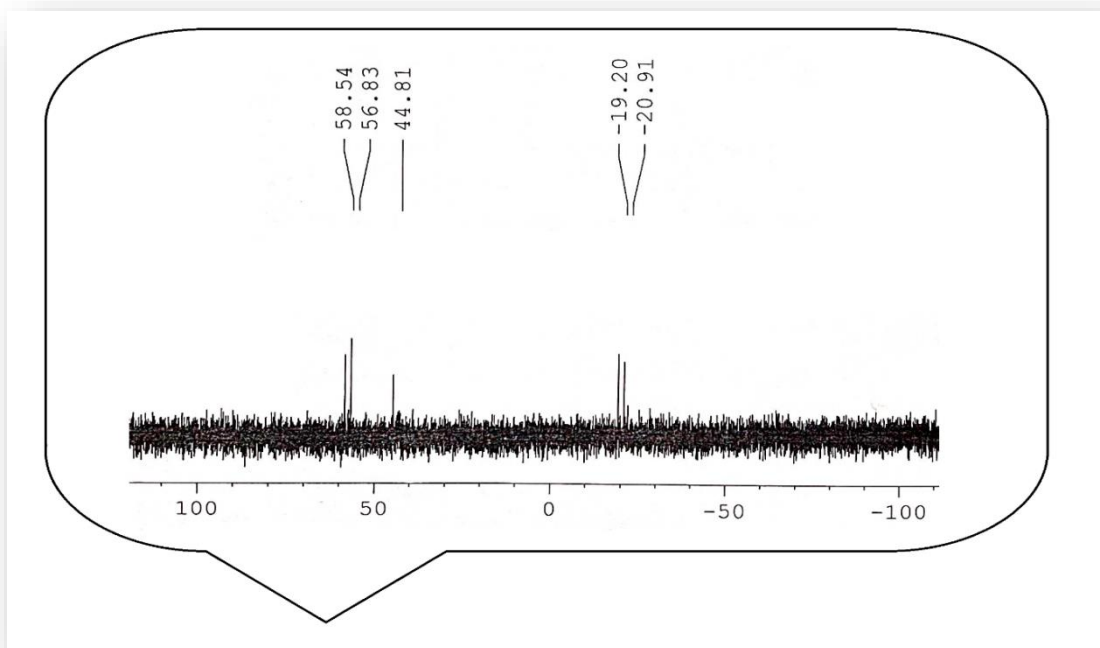


Figure 2. The $^{31}\text{P}\{-^1\text{H}\}$ NMR spectrum of decomposed products $\{(-\text{OP}(\text{O})\text{Cy}_2)$ and $\text{P}(\text{O})\text{Cy}_2\text{PCy}_2\}$.

It is well-known that dimers $\{[\text{Ru}(\text{arene})(\mu\text{-Cl})\text{Cl}]_2\}$ are capable of forming mononuclear complexes possessing a general formula of $[\text{Ru}(\eta^6\text{-arene})\text{Cl}_2\text{L}]$ [49]. Therefore, Ru(II) and Ir(III) complexes were prepared through reactions of metal precursor ($[\text{Ru}(\eta^6\text{-}p\text{-cymene})(\mu\text{-Cl})\text{Cl}]_2$ or $[\text{Ir}(\eta^5\text{-C}_5\text{Me}_5)(\mu\text{-Cl})\text{Cl}]_2$) and phosphinite (**Scheme 1**). All the reactions proceeded very readily in CH_2Cl_2 at RT and were almost quantitative. In contrast to the free ligand, which is quite air-sensitive, the complexes are stable microcrystalline solids and can be kept in the open air for an extended amount of time. The complexes were fully characterized by several spectroscopic techniques such as ^1H NMR, ^{13}C NMR, IR, and elemental analysis. In the $^{31}\text{P}\{-^1\text{H}\}$ NMR spectrum, Ru(II) complex (**3**) exhibits a singlet downfield at $\delta 156.01$ from the position of the free ligand (Fig. 1). Characteristic resonances of *p*-cymene protons for **3** were detected in the ^1H NMR spectrum at 5.82-5.79 ppm range as multiplets. For other characteristic signals of the *p*-cymene protons, the $-\text{CH}$, $-\text{CH}_3$, and $-\text{CH}(\text{CH}_3)_2$ resonances appeared at $\delta 2.84\text{-}2.81$, 2.08, and $1.78 + 1.23\text{-}1.18$ ppm, respectively. Furthermore, the $-\text{CH}$ and CH_2 protons of Cy in the OPCy_2 group gave multiplets at 2.46 and $1.78 + 1.23\text{-}1.18$ ppm, respectively. ^{13}C NMR spectrum of Ru (II) complex displays *p*-cymene signals, in addition to the resonances from the ligand. The IR spectrum of the Ru(II) complex **3** exhibits one new absorption peak at 553 cm^{-1} for Ru-P stretching vibration, indicating that phosphinite binds to the complex. So, we can conclude that our P-O donor ligand was bound to the Ru atom with a *p*-cymene group.

Simple coordination chemistry of (**2**) with $[\text{Ir}(\eta^5\text{-C}_5\text{Me}_5)(\mu\text{-Cl})\text{Cl}]_2$ precursors was investigated as well. The ^{31}P NMR signal of the Ir(III) complex obtained from the interaction of the phosphinite and iridium precursor was observed at 122.92 ppm as a singlet. The existence of a single signal at 1.53 ppm in the ^1H NMR spectrum of the Ir(III) complex (**4**) indicates that Ir(III) complex is formed. In the ^{13}C NMR spectrum of the Ir(III) complex, the luminous signals at 44.28–43.73 and 28.76–25.54 ppm belong to the $-\text{CH}$ and $-\text{CH}_2$ groups of the $-\text{OP}(\text{C}_6\text{H}_{11})$, respectively, and help illuminate the structure. In addition, the 9.45 and 93.92 ppm signals corresponded to the methyl and aromatic carbons of the Cp^* coordinated complex **4**, respectively. Extra the aliphatic and *N*-vinylimidazole ring carbon signals of complex **4** appeared, as expected. The infrared spectrum of (**4**) exhibits the bands at 3097, 2922, 2847, 1446, and 1058 cm^{-1} are due to $\nu(\text{aromatic C-H})$, $\nu(\text{aliphatic C-H})$, $\nu(\text{P-Cy})$, and $\nu(\text{O-P})$, respectively. Additionally, elemental analysis results also support the proposed structures.

3.2. Transfer hydrogenation of ketones

The transition metal catalyzed-hydrogen transfer process is usually assumed to include metal hydrides as important intermediates. Both complexes **3** and **4** most probably follow a well-known mechanism that includes a metal-alkoxide intermediate and β -elimination [50,51]. It has been shown that the replacement of chlorides by a hydride is easy through an alkoxide displacement/ β -hydride elimination sequence [52,53]. Ionic-liquid containing phosphinite ligands are indispensable compounds to obtain efficient catalysts that are homogeneous and organometallic [17-19]. The activity of the metal center is highly influenced by ligand choice. Ionic-liquid-based phosphinite complexes with coordination geometries of ruthenium or iridium show good activity in catalytic transfer hydrogenation [17-19,41].

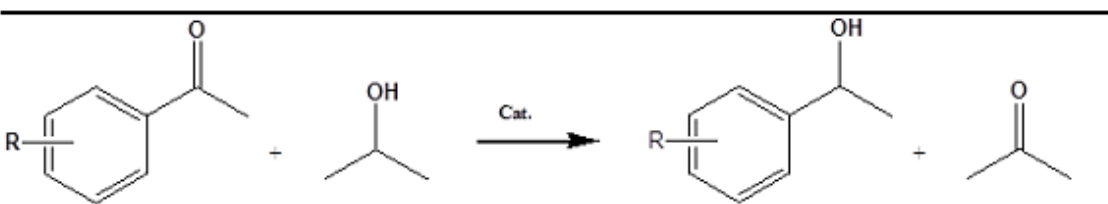
The synthesized Ru(II) and Ir(III) complexes (**3**) and (**4**) were employed as catalysts in the TH of acetophenone and its derivatives. First, as mentioned above, we thought to explore the TH of acetophenone in the existence of iridium and ruthenium-based catalysts. Thus, acetophenone has been hydrogenated in the existence of a catalyst with KOH as a base in 2-propanol. The transfer hydrogenation results are given in Table 1. Isopropanol is used as a hydrogen source in the hydrogenation and in this circumstance, the process occurs under thermodynamic control: when isopropanol gives hydrogen, acetone forms, and this is able to behave as a hydrogen acceptor, so, equilibrium is generated. The boiling point of 2-propanol is $82\text{ }^\circ\text{C}$, which enables it a good option to carry out the process at reflux temperature too [54]. Table 1 (entry 2 and entry 6) obviously depicted that the process cannot happen when a base is not used. Thus, one can conclude that the use of a base is necessary for this reaction [54,30,32,44,55]. The amount of base is generally 5 equivalent with respect to the catalyst [56-58]. Thus, our complexes act as good catalysts in TH reaction of acetophenone when isopropanol is used as a hydrogen donor at $82\text{ }^\circ\text{C}$, in the existence of a base, and after a certain time (1/2 h and 2 h for **3-4**, respectively), (Table 1 entry 1, entry 5). It was found that Ru(II) complex, **3** exhibited better activity in the transfer hydrogen. Because, ruthenium has different oxidation states, and a variety of coordination geometries introduced by various ligands, which render it is a good candidate for the catalyst for transfer hydrogenation as well as for the asymmetric version of transfer hydrogenation [59]. Furthermore, an increase in the amount of substrate increases the reaction time and leads to a reduction in TOF (Table 1 entry 3-4, entry 7-8).

Table 1. Transfer hydrogenation of acetophenone with 2-propanol catalyzed by 3 and 4.

Entry	Catalyst	S/C/KOH	Time	Conversion (%) ^[e]	TOF (h ⁻¹) ^[f]
1	3 ^[a]	100:1:5	1/2 h	99	198
2	3 ^[b]	100:1	12 h	>5	>5
3	3 ^[c]	500:1:5	2 h	98	230
4	3 ^[d]	1000:1:5	9 h	97	108
5	4 ^[a]	100:1:5	2 h	98	49
6	4 ^[b]	100:1	12 h	>5	>5
7	4 ^[c]	500:1:5	8 h	99	62
8	4 ^[d]	1000:1:5	24 h	98	41

Reaction conditions:
^[a] Refluxing in 2-propanol; acetophenone/Ru/KOH, (100:1:5); ^[b] Refluxing in 2-propanol; acetophenone/Ru, in the absence of base; ^[c] Refluxing in 2-propanol; acetophenone/Ru/KOH, (500:1:5); ^[d] Refluxing in 2-propanol; acetophenone/Ru/KOH, (1000:1:5); ^[e] Determined by GC (three independent catalytic experiments); ^[f] Referred at the reaction time indicated in column; TOF= (mol product/mol Ru(II)Cat.)x h⁻¹.

Under optimized conditions at hand, we investigated the extent of this TH reaction of acetophenone derivatives. It was observed that the corresponding alcohol is formed in a shorter time when using an acetophenone derivative that carries an electron-withdrawing moiety such as *p*-fluorine, *p*-chlorine, and *p*-bromine (Table 2, entry 1-3, entry 6-8). Because electron-withdrawing groups reduce the electron density of the C=O bond of the ketone, the ketone is more easily hydrogenated [60-62]. Secondly, TH of acetophenone derivatives containing *o*- and *p*-OCH₃ groups takes a longer reaction time and the TOF values are lower. Also, it was observed that when there is an electron-donating substituent on the *o*-position (-OCH₃), then, TOF value will be lower compared to the *p*-position. Indeed, the reaction time towards the transfer hydrogenation decreased from 9 h to 7 h when 4-MeO was used instead of 2-MeO catalyzed by 4 (Table 2, entry 9-10).

Table 2. Transfer hydrogenation results for substituted acetophenones with the catalyst systems, **3** and **4**^[a].


Entry	R	Time	Conversion(%) ^[b]	TOF(h ⁻¹) ^[c]
Catalyst, 3				
1	4-F	1/4 h	99	396
2	4-Cl	1/3 h	98	294
3	4-Br	1/2 h	99	198
4	2-MeO	3 h	94	31
5	4-MeO	2 h	98	49
Catalyst, 4				
6	4-F	1 h	98	98
7	4-Cl	3/2 h	97	65
8	4-Br	2 h	99	50
9	2-MeO	9 h	93	10
10	4-MeO	7 h	95	14

^[a] Catalyst (0.005 mmol), substrate (0.5 mmol), 2-propanol (5 mL), KOH (0.025 mmol %), 82 °C, the concentration of acetophenone derivatives is 0.1 M; ^[b] Purity of compounds is checked by ¹H NMR and GC (three independent catalytic experiments), yields are based on methyl aryl ketone; ^[c] TOF = (mol product/mol Cat.) x h⁻¹.

4. Conclusions and Perspectives

In conclusion, a new series of phosphinite-based Ru(II) and Ir(III) complexes were synthesized using a precursor of ionic liquid. These complexes were found to be effective catalysts and they are able to be easily applied, resulting in secondary alcohols with good to high yields. Moreover, ruthenium complex (**3**) behaved as a better catalyst for the transfer hydrogenation than the analogous Ir(III) complex. These catalysts are attractive because of their modular design and versatility in terms of transfer hydrogenation and future reports will focus on the use of the complexes that we have synthesized in TH of other activated aryl/alkyl ketones.

Acknowledgment

The authors would like to thank Dicle University Research Fund (Project number: **FEN.20.001**) for its kind support.

The Declaration of Ethics Committee Approval

The author declares that this document does not require an ethics committee approval or any special permission. Our study does not cause any harm to the environment.

Declaration of Competing Interest

The authors declare no potential conflicts of interest related to the research, authorship, and publication of this article.

Authors' Contributions:

U. I: Conceptualization, Methodology, Writing - Original draft preparation (35 %)

N. M.: Conceptualization, Methodology, Resources, Investigation, Writing (30 %)

M. A: Conceptualization, Formal analysis, Writing - Original draft preparation (35 %)

All authors read and approved the final manuscript.

Compliance with research and publication ethics:

This study was performed by complying with research and ethics rules.

References

- [1] Chauvin, R., "Zwitterionic Organometallates", *Eur. J. Inorg. Chem.*, 4, 577–591, 2000.
- [2] Zhang, H., Li, Y.-Q., Wang, P., Lu, Y., Zhao, X.-L., Liu, Y., "Effect of positive-charges in diphosphino- imidazolium salts on the structures of Ir-complexes and catalysis for hydroformylation", *Journal of Molecular Catalysis A: Chemical*, 411, 337–343, 2016.
- [3] Li, Y.Q., Wang, P., Zhang, H., Zhao, X.L., Lu, Y., Popović, Z., Liu, Y., "Influence of electrostatic repulsive force and electron-withdrawing effect in ionic diphosphine on regioselectivity of rhodium-catalyzed hydroformylation of 1-octene", *Journal of Molecular Catalysis A: Chemical*, 402, 37–45, 2015.
- [4] You, H.X., Wang, Y.Y., Zhao, X.L., Chen, S.J., Liu, Y., "Stable Ionic Rh(I,II,III) Complexes Ligated by an Imidazolium-Substituted Phosphine with π -Acceptor Character: Synthesis, Characterization, and Application to Hydroformylation", *Organometallics*, 32(9), 2698–2704, 2013.
- [5] Zhang, J., Wang, Y.Y., Zhao, X.L., Liu, Y., "Phosphane-Ligated Ionic Palladium Complexes: Synthesis, Characterization and Application as Efficient and Reusable Precatalysts for the Homogeneous Carbonylative Sonogashira Reaction under CuI-Free Conditions", *European Journal of Inorganic Chemistry*, 2014 (6), 975–985, 2014.
- [6] Zhou, C.L., Zhang, J., Đaković, M., Popović, Z., Zhao, X.L., Liu, Y., "Synthesis of an Ionic Paramagnetic Ruthenium (III) Complex and Its Application as an Efficient and Recyclable Catalyst for the Transfer Hydrogenation of Ketones", *European Journal of Inorganic Chemistry*, 2012 (21), 3435–3440, 2012.
- [7] Luska, K.L., Demmans, K.Z., Stratton, S.A., Moores, A., "Rhodium complexes stabilized by phosphine-functionalized phosphonium ionic liquids used as higher alkene hydroformylation catalysts: influence of the phosphonium headgroup on catalytic activity", *Dalton Transactions*, 41, 13533–13540, 2012.
- [8] Canac, Y., Maaliki, C., Abdellahab, I., Chauvin, R., "Carbeniophosphanes and their carbon \rightarrow phosphorus \rightarrow metal ternary complexes", *New Journal of Chemistry*, 36, 17–27, 2012.
- [9] Valizadeh, H., Khalili, E., "Efficient synthesis of symmetrical phthalate and maleate diesters using phosphinite ionic liquids", *Journal of the Iranian Chemical Society*, 9, 529–534, 2012.

- [10] Valizadeh, H., Shockravi, A., "Imidazolium-Based Phosphinite Ionic Liquid as Reusable Catalyst and Solvent for One-Pot Synthesis of 3,4-Dihydropyrimidin-2(1H)-(thio)ones", *Heteroatom Chemistry*, 20(5), 284-288, 2009 (a).
- [11] Valizadeh, H., Shockravi, A., "Task-Specific Ionic Liquid as Reagent and Reaction Medium for the One-Pot Horner–Wadsworth–Emmons–Type Reaction Under Microwave Irradiation", *Synthetic Communications*, 39, 4341–4349, 2009 (b).
- [12] Valizadeh, H., Gholipour, H., "Imidazolium-Based Phosphinite Ionic Liquid (ILOPPH₂) as Reusable Catalyst and Solvent for the Knoevenagel Condensation Reaction", *Synthetic Communications*, 40, 1477–1485, 2010.
- [13] Iranpoor, N. Firouzabadi, H., Azadi, R., "Imidazolium-based phosphinite ionic liquid (IL-OPPh₂) as Pd ligand and solvent for selective dehalogenation or homocoupling of aryl halides", *Journal of Organometallic Chemistry*, 693, 2469–2472, 2008.
- [14] Iranpoor, N. Firouzabadi, H., Azadi, R., "Diphenylphosphinite ionic liquid (IL-OPPh₂): A solvent and ligand for palladium-catalyzed silylation and dehalogenation reaction of aryl halides with triethylsilane", *Journal of Organometallic Chemistry*, 695, 887–890, 2010.
- [15] Iranpoor, N. Firouzabadi, H., Azadi, R., "An Imidazolium-Based Phosphinite Ionic Liquid (IL-OPPh₂) as a Reusable Reaction Medium and PdII Ligand in Heck Reactions of Aryl Halides with Styrene and n-Butyl Acrylate", *European Journal of Organic Chemistry*, 2007(13), 2197–2201, 2007.
- [16] Aydemir, M., Rafikova, K., Kystaubayeva, N., Pasa, S., Meriç, N., Ocak, Y. S., Zazybin, A., Temel, H., Gürbüz, N., Özdemir, İ., "Ionic liquid based Ru(II)–phosphinite compounds and their catalytic use in transfer hydrogenation: X-ray structure of an ionic compound 1-chloro-3-(3-methylimidazolidin-1-yl)propan-2-ol", *Polyhedron*, 81, 245–255, 2014.
- [17] Elma Karakaş, D., Durap, F., Baysal, A., Ocak, Y. S., Rafikova, K., Çavus Kaya, E., Zazybin, A., Temel, H., Kayan, C., Meriç, N., Aydemir, M., "Transfer hydrogenation reaction using novel ionic liquid based Rh(I) and Ir(III)-phosphinite complexes as catalyst," *Journal of Organometallic Chemistry*, 824, 25-32, 2016.
- [18] Meriç, N., Arslan, N., Kayan, C., Rafikova, K., Zazybin, A., Kerimkulova, A., Aydemir, M., "Catalysts for the asymmetric transfer hydrogenation of various ketones from [3-[(2S)-2-[(diphenylphosphanyl)oxy]-3-phenoxypropyl]-1-methyl-1H-imidazol-3-ium chloride] and [Ru(eta(6)-arene)(mu-Cl)Cl](2), Ir(eta(5)-C₅Me₅)(mu-Cl)Cl](2) or [Rh(mu-Cl)(cod)](2)", *Inorganica Chimica Acta*, 492, 108-118, 2019.
- [19] Ojima, I., *Catalytic Asymmetric Synthesis*, John Wiley, Hoboken, N.J., ISBN: 978-0-470-17577-4, 2010.
- [20] Baratta, W., Rigo, P., "1-(Pyridin-2-yl)methanamine-Based Ruthenium Catalysts for Fast Transfer Hydrogenation of Carbonyl Compounds in 2-Propanol", *European Journal of Inorganic Chemistry*, 2008, 4041-4053, 2008.
- [21] Cavallo, M., Arnodo, D., Mannu, A., Blangetti, M., Prandi, C., Baratta, W., "Salvatore Baldino Deep eutectic solvents as H₂-sources for Ru(II)-catalyzed transfer hydrogenation of carbonyl compounds under mild conditions", *Tetrahedron* 83, 131997, 2021.

- [22] Breuer, M., Ditrich, K., Habicher, T., Hauer, B., Kebeler, M., Sturmer, R., Zelinski, T., "Industrial methods for the production of optically active intermediates", *Angewandte Chemie International Edition*, 43, 788–824, 2004.
- [23] Foubelo, F., Najera, C., Yus M., "Catalytic asymmetric transfer hydrogenation of ketones: recent advances", *Tetrahedron: Asymmetry*, 26, 769–790, 2015.
- [24] Blanco, C. O., Llovera, L., Herrera, A., Dorta, R., Agrifoglio, G., Venuti, D., Landaeta, V. R., Pastr'an J., "Ruthenium (II) complexes with C₂- and C₁-symmetric bis-(+)-camphopyrazole ligands and their evaluation in catalytic transfer hydrogenation of aldehydes", *Inorganica Chimica Acta*, 524, 120429, 2021.
- [25] Ak, B., Elma, D., Meriç, N., Kayan, C., Işık, U., Aydemir, M., Durap, F., Baysal, A., "New chiral ruthenium(II)–phosphinite complexes containing a ferrocenyl group in enantioselective transfer hydrogenations of aromatic ketones", *Tetrahedron: Asymmetry*, 24, 1257-1264, 2013.
- [26] Ak, B., Aydemir, M., Ocağ, Y. S., Durap, F., Kayan, C., Baysal, A., Temel, H., "Readily available ferrocenyl-phosphinite ligands for Ru(II)-catalyzed enantioselective transfer hydrogenation of ketones and fabrication of hybrid heterojunctions", *Inorganica Chimica Acta*, 409, 244-253, 2014.
- [27] Aydemir, M., Baysal, A., Meric, N., Gümğüm, B., "New active ruthenium(II) complexes based N₃,N₃'-bis(diphenylphosphino)-2,20-bipyridine-3,3'-diamine and P,P'-diphenylphosphinous acid-P,P'-[2,2'-bipyridine]-3,3'-diyl ester ligands for transfer of aromatic ketones by propan-2-ol", *Journal of Organometallic Chemistry*, 694, 2488-2492, 2009.
- [28] Elma, D., Durap, F., Aydemir, M., Baysal, A., Meriç, N., Ak, B., Turgut, Y., Gümğüm, B., "Screening of C₂-symmetric chiral phosphinites as ligands for ruthenium(II)-catalyzed asymmetric transfer hydrogenation of prochiral aromatic ketones", *Journal of Organometallic Chemistry*, 729, 46-52, 2013.
- [29] Aydemir, M., Meric, N., Baysal, A., Gümğüm, B., Toğrul, M., Turgut, Y., "A modular design of ruthenium(II) catalysts with chiral C₂-symmetric phosphinite ligands for effective asymmetric transfer hydrogenation of aromatic ketones", *Tetrahedron: Asymmetry*, 21, 703-710, 2010.
- [30] Aydemir, M., Meric, N., Baysal, A., Kayan, C., Toğrul, M., Gümğüm, B., "New chiral phosphinite ligands with C₂-symmetric axis and their possible applications in Ru-catalyzed asymmetric transfer hydrogenation", *Applied Organometallic Chemistry*, 24, 215-221, 2010.
- [31] Aydemir, M., Meric, N., Durap, F., Baysal, A., Toğrul, M., "Asymmetric transfer hydrogenation of aromatic ketones with the ruthenium(II) catalyst derived from C₂ symmetric N,N'-bis[(1S)-1-benzyl-2-O-(diphenylphosphinite)ethyl]ethanediamide", *Journal of Organometallic Chemistry*, 695, 1392-1398, 2010.
- [32] Aydemir, M., Durap, F., Baysal, A., Meric, N., Buldağ, A., Gümğüm, B., Özkar, S., Yıldırım, L. T., "Novel neutral phosphinite bridged dinuclear ruthenium(II) arene complexes and their catalytic use in transfer hydrogenation of aromatic ketones: X-ray structure of a new Schiff base, N₃,N₃-di-2-hydroxybenzylidene-[2,2]bipyridinyl-3,3-diamine", *Journal of Molecular Catalysis A: Chemical*, 326, 75-81, 2010.
- [33] Holbrey, J. D., Turner, M. B., Reichert W. M., and Rogers 'R. D., "New ionic liquids containing an appended hydroxyl functionality from the atom-efficient, one-pot reaction of 1-methylimidazole and acid with propylene oxide", *Green Chemistry*, 5, 731–736, 2003.

- [34] Glas H., and Thiel, W. R., "Microwave assisted synthesis of chiral imidazolyl and pyrazolyl alcohols", *Tetrahedron Letters*, 39, 5509-5510, 1998.
- [35] Glas, H., Herdtweck, E., Spiegler, M., Pleier, A., Thiel W. R.X, "A simple access to palladium complexes of functionalized heterocyclic carbenes", *Journal of Organometallic Chemistry*, 626, 100–105, 1998.
- [36] Paul C. E., Lavandera I., Gotor-Fernandez V., Gotor V., "Imidazolium-Based Ionic Liquids as Non-conventional Media for Alcohol Dehydrogenase-Catalysed Reactions", *Topics in Catalysis*, 57, 332–338, 2014.
- [37] Arnold, P. L., Scarisbrick, A. C., Blake A. J., Wilson C., "Chelating alkoxy-N-heterocyclic carbene complexes of silver and copper", *Chemical Communications*, 2001, 2340–2341, 2001.
- [38] Allegue, A., Albert-Soriano, M., Pastor, I. M., "A comparative study of hydroxyl- and carboxylate-functionalized imidazolium and benzimidazolium salts as precursors for N-heterocyclic carbene ligands", *Applied Organometallic Chemistry*, 29, 624–632, 2015.
- [39] Chen, C., "A functionalised ionic liquid: 1-(3-chloro-2-hydroxypropyl)-3-methyl imidazolium chloride", *Physics and Chemistry of Liquids*, 48, 298–306, 2010.
- [40] Arslan, N., "Enantioselective transfer hydrogenation of pro-chiral ketones catalyzed by novel ruthenium and iridium complexes of well-designed phosphinite ligand", *Phosphorus, Sulfur, and Silicon and The Related Elements*, 195(8), 628–637, 2020.
- [41] Rafikova, K., Ertekin Binbay, N., Meriç, N., Kerimkulova, A., Zazybin, A., Binbay, V., Okumuş, V., Kayan, C., Işık, U., Arslan, N., Aydemir, M., "Biological assays and theoretical density functional theory calculations of Rh(I), Ir(III), and Ru(II) complexes of chiral phosphinite ligand", *Applied Organometallic Chemistry*, 34, 5658, 2020.
- [42] Meriç, N., Kayan, C., Rafikova, K., Zazybin, A., Okumuş, V., Aydemir, M., Durap, F., "Synthesis of ionic liquid-based Ru(II)-phosphinite complexes and evaluation of their antioxidant, antibacterial, DNA-binding, and DNA cleavage activities", *Chemical Papers*, 73, 1199-1208, 2019.
- [43] Meriç, N., Aydemir, M., Işık, U., Ocak, Y. S., Rafikova, K., Pasa, S., Kayan, C., Durap, F., Zazybin, A., Temel, H., "Cross-coupling reactions in water using ionic liquid-based palladium(II)-phosphinite complexes as outstanding catalysts", *Applied Organometallic Chemistry*, 28, 818–825, 2014.
- [44] Aydemir, M., Meriç, N., Baysal, A., Turgut, Y., Kayan, C., Şeker, S., Toğrul, M., Gümgüm, B., "Asymmetric transfer hydrogenation of acetophenone derivatives with novel chiral phosphinite based η^6 -p-cymene/ruthenium(II) catalysts", *Journal of Organometallic Chemistry*, 696, 1541-1546, 2011.
- [45] Ruhlan, K., Gigler, P., Herdweck, E., "Some phosphinite complexes of Rh and Ir, their intramolecular reactivity and DFT calculations about their application in biphenyl metathesis", *Journal of Organometallic Chemistry*, 693, 874-893, 2008.
- [46] Broger, E.A., Burkart, W., Hennig, M., Scalone, M., Schmid, R., "Some phosphinite complexes of Rh and Ir, their intramolecular reactivity and DFT calculations about their application in biphenyl metathesis" *Tetrahedron: Asymmetry* 9, 4043-4054, 1998.
- [47] Roucoux, A., Thieffry, L., Carpentier, J., Devocelle, M., Méliet, C., Agbossou, F., Mortreux, A., Welch, A. J., "Amidophosphine-Phosphinites: Synthesis and Use in Rhodium-Based

- Asymmetric Hydrogenation of Activated Keto Compounds. Crystal Structure of Bis[(μ -chloro)((S)-2-((diphenylphosphino)oxy)-2-phenyl- N-(diphenylphosphino)-N-methylacetamide)rhodium(I)]”, *Organometallics*, 15, 10, 2440–2449, 1996.
- [48] Meric, N., “Synthesis of heterodonor ligands and investigation of their catalytic applications”, Ph.D. thesis, Dicle University, Diyarbakır, Turkey, 2012.
- [49] Bozec, H. Le, Touchard, D., Dixneuf, P. H., “Organometallic Chemistry of Arene Ruthenium and Osmium Complexes” *Advances in Organometallic Chemistry*, 29, 163-247, 1989.
- [50] Zassinowich, G., Mestroni, G., Gladiali, S., “Asymmetric hydrogen transfer reactions promoted by homogeneous transition metal catalysts”, *Chemical Reviews*, 92, 1051-1069, 1992.
- [51] Palmer, M. J., Wills, M., “Asymmetric transfer hydrogenation of C=O and C=N bonds”, *Tetrahedron: Asymmetry*, 10, 2045-2061, 1999.
- [52] Chaudret, B. N., Cole-Hamilton, D. J., Nohr, R. S., Wilkinson, G., “The reactions of chlorohydrido- and dichloro-tris(triphenylphosphine) ruthenium(II) with alkali hydroxides and alkoxides. Hydridohydroxobis(triphenylphosphine)ruthenium(II) monosolvates, their reactions and related compounds”, *Journal of the Chemical Society, Dalton Transactions* 1546-1557, 1977.
- [53] Vaska, L., Diluzio, J. W., “On the Origin of Hydrogen in Metal Hydride Complexes Formed by Reaction With Alcohols”, *Journal of the American Chemical Society*, 84, 4989-4990, 1962.
- [54] Mannu, A., Grabulosa A., Baldino S., “Transfer Hydrogenation from 2-propanol to Acetophenone Catalyzed by [RuCl₂(η -6-arene)P] (P = monophosphine) and [Rh(PP)₂]X (PP = diphosphine, X = Cl⁻, BF₄⁻) Complexes”, *Catalysts*, 10, 162, 2020. doi:10.3390/catal10020162
- [55] Meriç, N., Durap, F., Aydemir, M., Baysal, A., “The application of tunable tridentate P-based ligands for the Ru(II)-catalysed transfer hydrogenation of various ketones”, *Applied Organometallic Chemistry*, 28, 803–808, 2014.
- [56] Kayan, C., Meriç, N., Rafikova, K., Zazybin, A., Gürbüz, N., Karakaplan, M., Aydemir, M., “A new class of well-defined ruthenium catalysts for enantioselective transfer hydrogenation of various ketones” *Journal of Organometallic Chemistry*, 869, 37-47, 2018.
- [57] Meriç, N., Kayan, C., Gürbüz, N., Karakaplan, M., Erkin Binbay, N., Aydemir, M., "New functional chiral P-based ligands and application in ruthenium-catalyzed enantioselective transfer hydrogenation of ketones", *Tetrahedron: Asymmetry* 28, 1739-1749, 2017.
- [58] Ak, B., Aydemir, M., Durap, F., Meriç, N., Elma, D., Baysal, A., “Highly efficient iridium catalysts based on C₂-symmetric ferrocenyl phosphinite ligands for asymmetric transfer hydrogenations of aromatic ketones”, *Tetrahedron: Asymmetry*, 26, 1307-1313, 2015.
- [59] Tyagi, N., Borah, G., Patel P., Ramaiah, D., Recent Advances in Ru Catalyzed Transfer Hydrogenation and Its Future Perspectives, in: *Ruthenium - An Element Loved by Researchers* (Ed. H. Ishida), Intechopen Book Series, London, pp.99-122. 2022. doi: 10.5772/intechopen.96464
- [60] Faller, J. W., Lavoie, A. R., Catalysts for the Asymmetric Transfer Hydrogenation of Ketones Derived from l-Prolinamide and (p-CymeneRuCl₂)₂ or (Cp*RhCl₂)₂, *Organometallics*, 20, 5245-5247, 2001.
- [61] Özdemir, I., Yaşar, S., Çetinkaya, B., “Ruthenium(II) N-heterocyclic Carbene Complexes in the Transfer Hydrogenation of Ketones”, *Transition Metal Chemistry*, 30, 831-835, 2005.

- [62] Ak, B., Aydemir, M., Durap, F., Meriç, N., Baysal, A., “The first application of C₂-symmetric ferrocenyl phosphinite ligands for rhodium-catalyzed asymmetric transfer hydrogenation of various ketones”, *Inorganica Chimica Acta*, 438, 42–51, 2015.



DFT INVESTIGATION OF TRANSITION METALS ARENE COMPOUNDS WITH FUNCTIONALIZED IONIC LIQUID

Nermin MERİÇ^{*1,2}  **Nil ERTEKİN BINBAY³**  **Cezmi KAYAN^{*1}**  **Veysel BINBAY⁴** 
Murat AYDEMİR¹ 

¹Dicle University, Faculty of Science, Department of Chemistry, 21280, Diyarbakir, Turkey

²Dicle University, Technical Vocational School, Department of Hair Care and Beauty Services, 21280, Diyarbakir, Turkey

³Dicle University, Technical Vocational School, Department of Electronics, 21280, Diyarbakir, Turkey

⁴Dicle University, Institute of Natural Science, Department of Physics, 21280, Diyarbakir, Turkey

*Corresponding author; nmeric@dicle.edu.tr

Abstract: *Electrochemical properties and theoretical DFT computations have been carried out for the cationic parts of complexes of ionic liquid-based phosphinite, (IA-3A). The effects of the chemical structures of cationic parts of three complexes were examined in relation to the variable property of electron-donating ligands for ruthenium and iridium complexes were determined. Their potential energy surfaces in the ground state, electronic densities, and also frontier orbitals HOMO and LUMO have been obtained via DFT calculations. It has been shown that DFT calculations can successfully be used for exploring electrochemical properties of cations, which includes transition metals. It was revealed that complex IA is the chemically softest molecule, while complex 2A is the most electrophilic one.*

Keywords: *Ionic Liquid, HOMO-LUMO, DFT calculation, Iridium, Ruthenium.*

Received: April 05, 2022

Accepted: June 01, 2022

1. Introduction

Computer-based theoretical calculations have become a crucial tool, especially in the last decades [1]. Many theoretical techniques, such as Density Functional Theory (DFT) ab-initio methods, molecular mechanics simulations, and some quasi-experimental methods are often used to study molecular properties in several fields such as pharmacology and materials engineering [2]. Among them, Density Functional Theory (DFT), has proved itself the most effective approach for many chemical calculations, such as optimizing molecular structures, obtaining molecular electrostatic potential (MEP), total electron densities, and energy levels of frontier orbitals (HOMO and LUMO) and also chemical descriptors including chemical hardness, electrophilicity, electronegativity, and chemical potential [3,4,5,6]. Furthermore, DFT technique is also preferred due to its computationally low costs and relatively high performance [1,3].

Within this perspective, we have started to study transition metal complexes containing phosphinite moiety with imidazolium ionic liquids, in order to understand the electrochemical behavior of transition metal complexes of phosphinites better and perform the theoretical calculations of such complexes [7]. In this study, DFT studies of cationic parts of previously synthesized Ru(II)- and Ir(III)-phosphinite compounds based on ionic liquid were reported. Also, the impacts of the

chemical constructions of three phosphinite complexes were selected in relation to the variable property of η^6 -p-cymene, η^6 -benzene and η^5 -C₅Me₅ substituent for **1A**, **2A** and **3A**, respectively and determined their potential energy levels and induced levels HOMO and LUMO. The highest occupied molecular orbital (HOMO) and lowest unoccupied molecular orbital (LUMO) levels were computed by DFT approach.

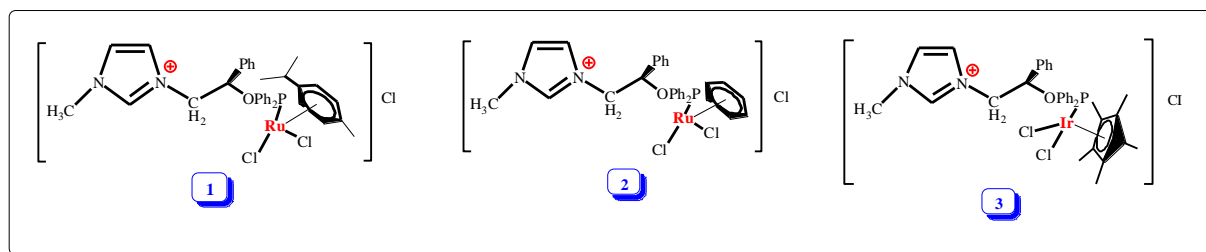
2. Experimental Computational method

All calculations were performed by using DFT (Density Functional Theory) approach. GAMESS (the General Atomic and Molecular Electronic Structure System), which is a general *ab initio* quantum chemistry package, was used for calculations [1,8]. The exchange-correlation functional for calculations was the hybrid Becke, three-parameter, Lee-Yang-Parr, using the coulomb attenuating method (CAM-B3LYP) [9]. And also, the SBKJ (Stevens, Bash, Krauss, Jasien) valance basis set was used with ECP (Effective Core Potential) [10]. There were no imaginary frequencies for any cases, therefore it is confirmed that the optimized molecular structures correspond to real minims on the PES (Potential Energy Surface).

3. Results and Discussion

3.1. DFT Study

DFT method was used to unravel the electrochemical behavior of cationic parts of previously prepared complexes **1-3** (Scheme 1) [11]. Since outer chlorine atom moves freely in the solution, it was excluded in the calculations, and the remaining positively charged part (**1A-3A**) was taken into account.



Scheme 1. [3-[(2R)-2-({[dichloro(η^6 -p-cymene)ruthenium]diphenyl phosphanyl}oxy)-2-phenylethyl]-1-methyl-1H-imidazol-3-ium chloride] (**1**), [3-[(2R)-2-({[dichloro(η^6 -benzene)ruthenium] diphenylphosphanyl}oxy)-2-phenylethyl]-1-methyl-1H-imidazol-3-ium chloride] (**2**), [3-[(2R)-2-({[dichloro(η^5 -pentamethylcyclopentadienyl)iridium] diphenyl phosphanyl}oxy)-2-phenylethyl]-1-methyl-1H-imidazol-3-ium chloride] (**3**).

The optimized molecular structures of cationic parts (**1A-3A**) of complexes **1-3** have been given in Figure 1. As known, optimized molecular structure of a molecule represents the minimal energy conformation of the molecule, and that's why it is important [12].

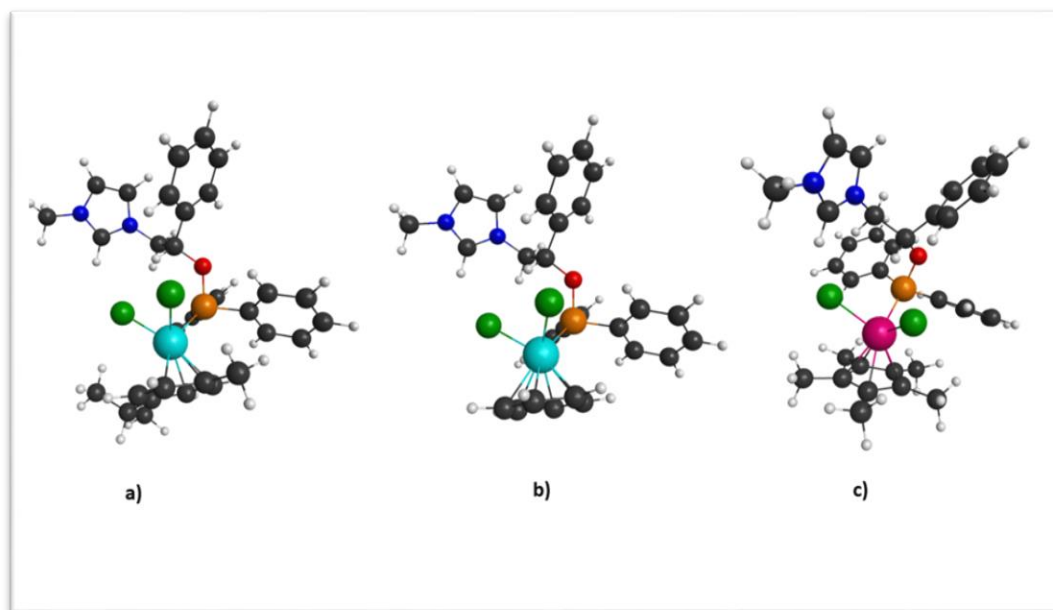


Figure 1. The optimized molecular structure of (a) **1A**, (b) **2A**, and (c) **3A**.

The molecular electrostatic potential (MEP) is helpful to investigate the molecular features including hydrogen bonding, and nucleophilic and electrophilic attacks on the molecule site [13,14]. Since the MEP is basically a three-dimensional map that gives the electrostatic potential for every point all around the molecule, it is a very fruitful source of information to estimate how the molecule responds to other molecules in any possible cases. For instance, it can be used to estimate both possible locations and relative intensities of both nucleophilic and electrophilic attacks by other molecules [15]. The reactivity of molecules can also be predicted by visual inspection of different colors, which represent different values of the MEP [16,17]. The red color corresponds to the positive potential regions, which are localized over the hydrogen atoms, whereas the blue color indicates the high electron density as well as negative potential regions, which are localized over the electronegative atoms (nitrogen, oxygen) [18,19]. As seen in Figure 2, **1A-3A** have dominant positive potential, therefore their MEPs are almost fully red, as expected because they are actually positively charged cations.

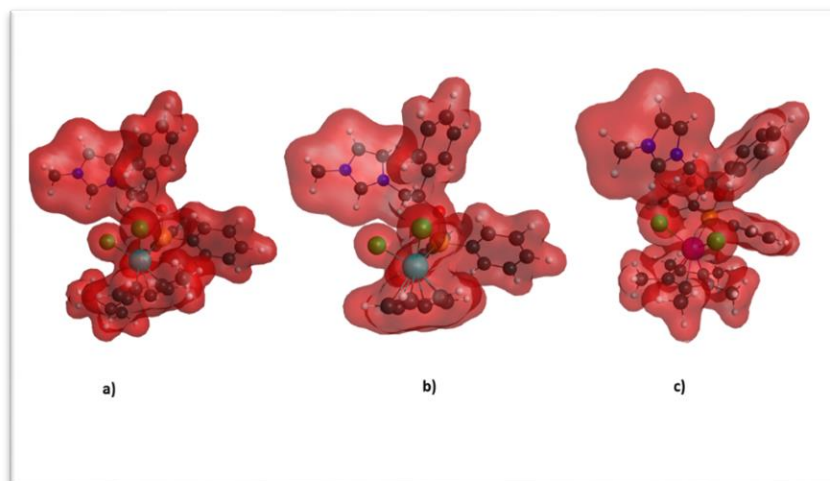


Figure 2. The molecular electrostatic potential of (a) **1A**, (b) **2A**, and (c) **3A**.

As known, the total electronic density is a graph of quantum mechanics probabilities of finding electrons at every given point. It can give us a strong insight into molecules' overall and local polarization. Information on electronic densities also can help to interpret the behavior of the molecule in chemical interactions [20-22]. As it can be seen in Figure 3, while there are no big differences in electronic densities around each atom, still electrons can be found slightly denser around oxygen and chlorine atoms.

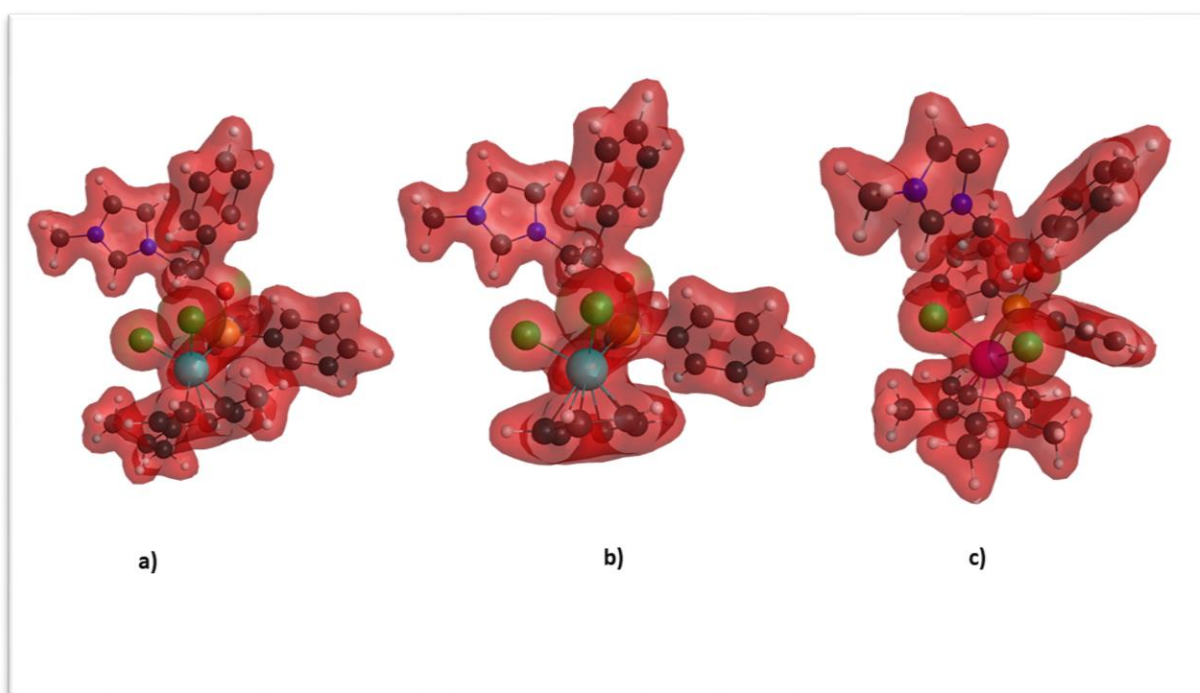


Figure 3. The total electron density of (a) **1A**, (b) **2A**, and (c) **3A**.

Molecular orbital analysis is crucial in establishing the compound's electrical and optical characteristics, as well as its chemical reactions [23]. The energies of HOMOs and LUMOs of **1A-3A** are given in **Figure 4** and Table 1. A substantial E_{HOMO} value indicates a higher ability to donate

electrons, whereas a lower E_{LUMO} value shows a higher tendency to accept electrons [17, 24]. The calculated HOMO energy values tabulated in Table 3 are -9.3607 eV, -9.5784 eV, and -9.4968 eV, for **1A-3A**, respectively. Thus, the ability of **3A** to donate electrons is lower than **1A**, but it is higher than that of **2A**. LUMO energy values of **1A-2A** were found as -2.8028 eV, -2.9116 eV, and -2.6395 eV, respectively. On the contrary, the ability of **1A** to accept electrons is lower than **2A**, but it is higher than that of **3A**. When ΔE values for cationic parts of these complexes were considered, it was observed that they were 6.5579, 6.6668, and 6.8573 eV, respectively (Figure 1 and Table 1), implying that the complexes are rather stable. If we compare ΔE values for the cationic parts of complexes with each other, we realize that the energy gap ($\Delta E = E_{\text{LUMO}} - E_{\text{HOMO}}$) of **1A** is smaller, leading to lower kinetic stability and a higher chemical reactivity than those of **2A** and **3A** [17,25]. Furthermore, considering the type of transition metal in **Figure 4**, one can conclude that cationic parts of Ru(II) complexes **1A** and **2A** are more reactive than those of Ir(III) complex **3A**.

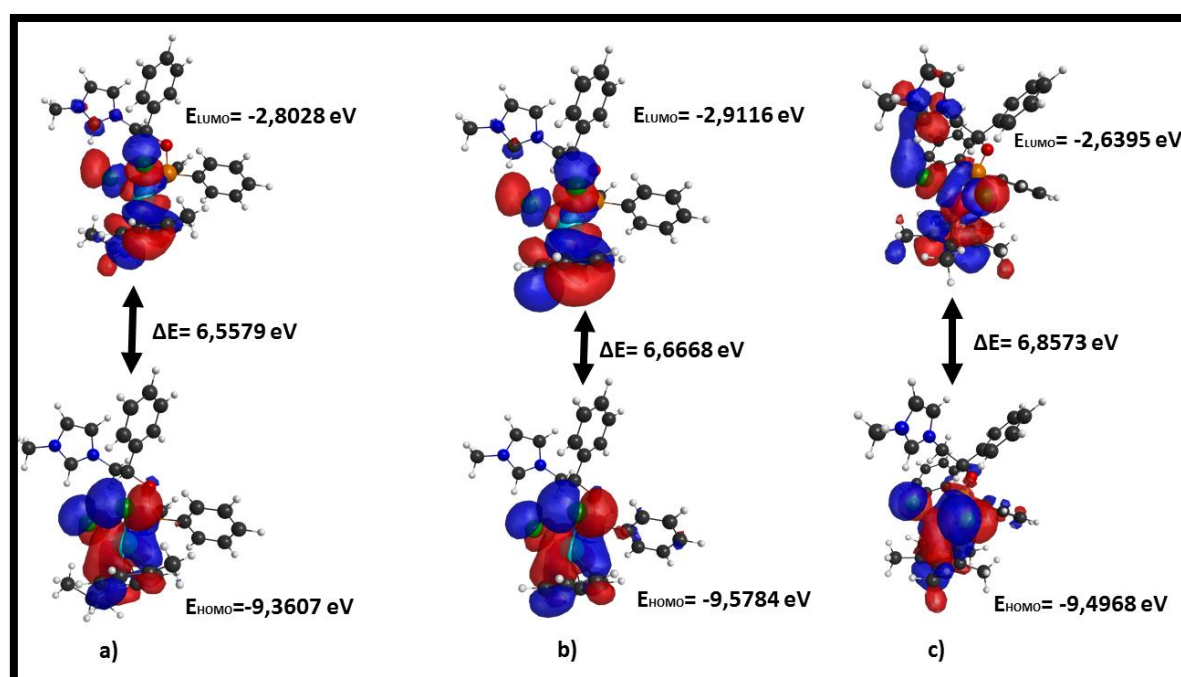


Figure 4. Frontier molecular orbitals (HOMO-LUMO) of **1A-3A** calculated by DFT.

The calculated chemical descriptors for **1A-3A**, χ (electronegativity), η (chemical hardness), ω (electrophilicity), S (softness), and μ (chemical potential) have been given in Table 1 and Figures 5-7. A big ΔE indicates a hard molecule, whereas a small ΔE indicates a soft molecule. Because they could easily supply electrons to an acceptor, soft molecules are more reactive than hard ones [23]. When we look at Figure 5, we see that the hardness of **1A** is lower (softness is higher, Table 1), since it has a lower ΔE value, implying that it is more reactive than the other cationic parts of complexes. Electrophilicity is the other theoretical descriptor that can be used to make a comment about the electron-accepting tendency of a molecule [17, 26]. The electrophilicity indexes of the presented **1A-3A** are 5.6402 eV, 5.8499 eV, and 5.3698 eV respectively, as seen in Figure 6. Electrophilicity indexes of **2A** are higher than that of **1A** and **3A**, indicating that it has the strongest electrophilic character. As DFT calculations showed, **2A** is also the most electronegative one (χ :6.2450 eV, Figure 7, Table 1). Then, its chemical potential becomes -6.2450 eV (Table 1), because chemical potential (μ) is the negative of electronegativity [14].

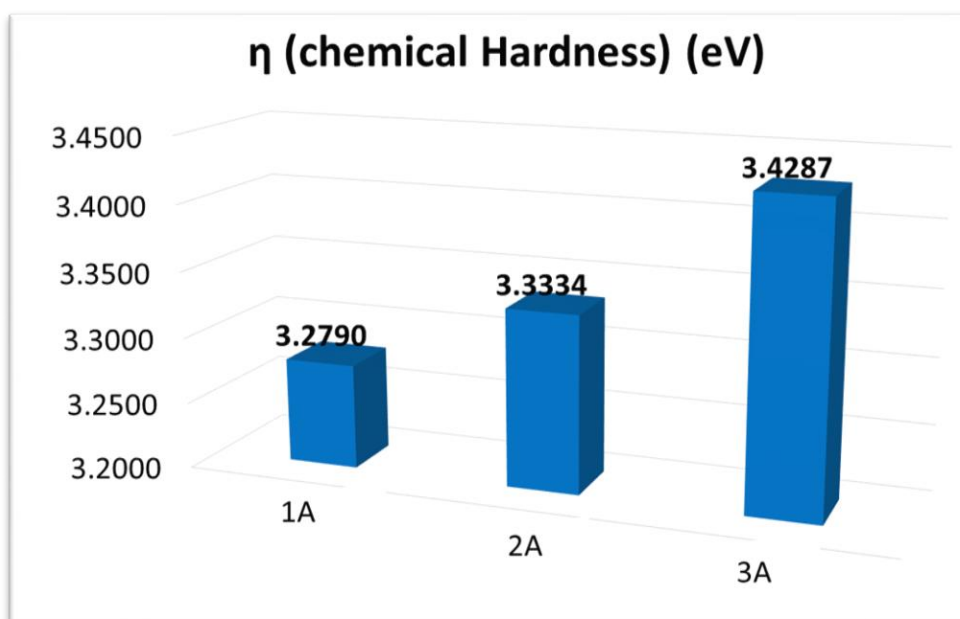


Figure 5. The calculated η (chemical Hardness) values of 1A-3A.

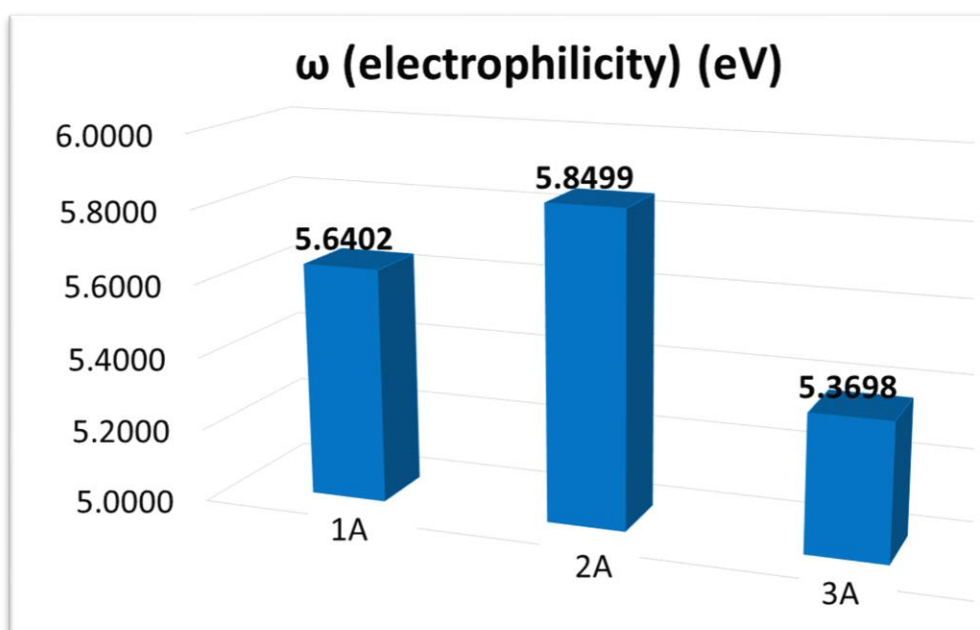


Figure 6. The computed ω (electrophilicity) values of 1A-3A.

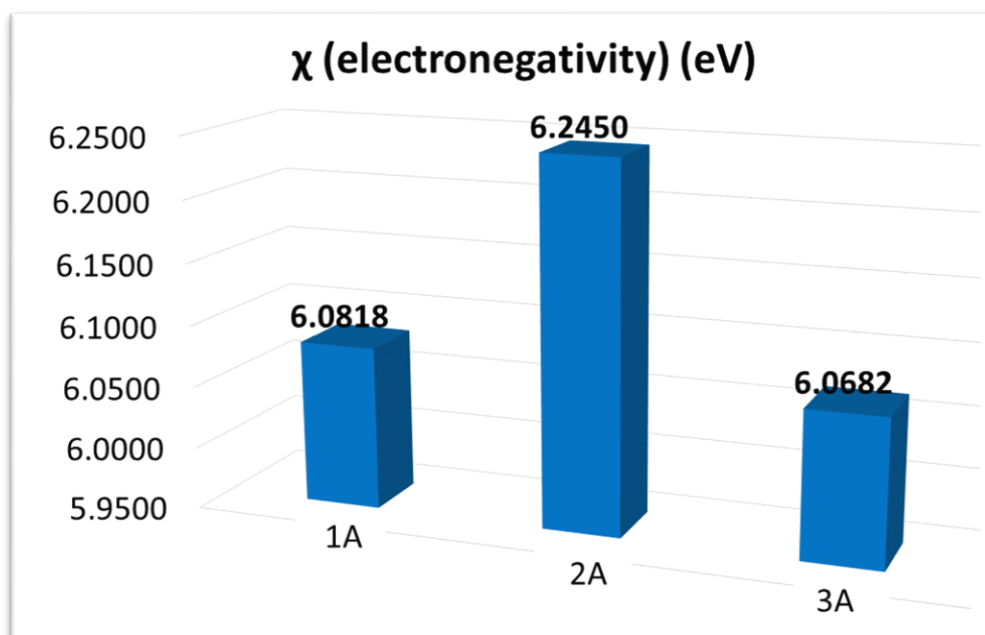


Figure 7. The calculated χ (electronegativity) values of **1A-3A**.

Table 1. The calculated E_{HOMO} , E_{LUMO} , ΔE , and chemical descriptors (η (chemical hardness), S (softness), ω (electrophilicity), χ (electronegativity) and μ (chemical potential)) for cationic parts of complexes **1A-3A**.

Molecules	$E_{\text{(HOMO)}}$ (eV)	$E_{\text{(LUMO)}}$ (eV)	ΔE (eV)	η (eV)	S (eV ⁻¹)	ω (eV)	χ (eV)	μ (eV)
1A	-9.3607	-2.8028	6.5579	3.2790	0.3050	5.6402	6.0818	-6.0818
2A	-9.5784	-2.9116	6.6668	3.3334	0.3000	5.8499	6.2450	-6.2450
3A	-9.4968	-2.6395	6.8573	3.4287	0.2917	5.3698	6.0682	-6.0682

4. Conclusion and Perspectives

In conclusion, the molecular structure of the complexes of an ionic liquid-based chiral phosphinite ligand was successfully examined by using the Density Functional Theory (DFT). Molecular electrostatic potential and total electron density of cationic parts of the studied complexes indicated the existence of proper sites to attack electrophilic and nucleophilic substances. Calculated $E_{\text{(HOMO)}}$ & $E_{\text{(LUMO)}}$ values for three cationic substances are in line with the expectations for free cationic structures. We can see that $E_{\text{(HOMO)}}$ values are deep below zero (around -9.5 eV) while $E_{\text{(LUMO)}}$ values also meaningfully deeper than zero eV (around -2.8 eV). The lowest energy gap (ΔE) for **1A** means that it is expected to behave chemically more reactive than **2A** and **3A** in solution as softer cation. On the other hand, **2A** is the most electrophilic and the most electronegative one, therefore it is more likely become an effective target for nucleophilic attacks. Thus, as a main conclusion, we can say that according to fruitful DFT calculations, we gained further useful insight into the electrochemical behavior of the complexes.

Acknowledgments

Partial support of this work by Dicle University (Project number: **FEN.21.008**) is gratefully acknowledged.

The Declaration of Ethics Committee Approval

The authors declare that this document does not require an ethics committee approval or any special permission. Our study does not cause any harm to the environment.

Declaration of Competing Interest

The authors declare no potential conflicts of interest related to the research, authorship, and publication of this article.

Authors' Contributions

N.M: Conceptualization, Methodology, Formal analysis, Writing - Original draft preparation (20%).

N. E. B: Methodology, Resources, Investigation, Visualization (20%).

C.K: Data curation, Visualization, Investigation, Methodology (20%).

V.B: Conceptualization, Software, Methodology, Investigation (20%).

M.A: Conceptualization, Supervision, Validation, Funding acquisition (20%).

All authors read and approved the final manuscript.

The compliance to research and publication ethics:

This study was performed by complying research and ethics rules.

References

- [1] [1] Gordon M.S., Schmidt M.W., "Advances in electronic structure theory: GAMESS a decade later", In: "Theory and Applications of Computational Chemistry, the first forty years", Dykstra C.E., Frenking G., Kim K.S., Scuseria G.E. (eds) Elsevier, Amsterdam, pp. 1167-1189, 2005.
- [2] Demircioğlu Z., Ersanlı C.C., Alpaslan G., "Calculations of Charge Transfer with DNA bases and Local&Global Chemical Activity by Computational Chemistry Method of (Z)-Ethyl 4-chloro-2-[2-(2-methoxyphenyl)hydrazono]-3-oxobutanoate Crystal", *Sinop University Journal of Natural Science*, 4(2), 93-108, 2019. <https://doi.org/10.33484/sinopfdb.562618>
- [3] Hohenberg P., Kohn W., "Inhomogeneous Electron Gas", *Physical Review*, 136(3B), B864-B871, 1964. <https://doi.org/10.1103/PhysRev.136.B864>
- [4] Obot I.B., Macdonald D.D., Gasem Z.M., "Density functional theory (DFT) as a powerful tool for designing new organic corrosion inhibitors. Part 1: An overview", *Corrosion Science*, 99, 1-30, 2015. <https://doi.org/10.1016/j.corsci.2015.01.037>
- [5] Riley K.E., Merz K.M., "Assessment of Density Functional Theory Methods for the Computation of Heats of Formation and Ionization Potentials of Systems Containing Third Row Transition Metals", *The Journal of Physical Chemistry A*, 111(27), 6044-6053, 2007. <https://doi.org/10.1021/jp0705931>
- [6] Chaquin P. "Absolute electronegativity and hardness: An analogy with classical electrostatics suggests an interpretation of the Parr 'electrophilicity index' as a 'global energy index' leading to the 'minimum electrophilicity principle", *Chemical Physics Letters*, 458(1-3), 231-234, 2008. <https://doi.org/10.1016/j.cplett.2008.04.087>
- [7] Rafikova K., Binbay N.E., Meric N., Kerimkulova A., Zazybin A., Binbay V., Okumus V., Kayan C., Isik U., Arslan N., Aydemir M., "Biological assays and theoretical density functional

- theory calculations of Rh(I), Ir(III), and Ru(II) complexes of chiral phosphinite ligand”, *Applied Organometallic Chemistry*, 34, e5658, 2020. <https://doi.org/10.1002/aoc.5658>
- [8] Schmidt M.W., Baldrige K.K., Boatz J.A., Elbert S.T., Gordon M.S., Jensen J.H., Koseki S., Matsunaga N., Nguyen K.A., Su S., Windus T.L., Dupuis M., Montgomery J.A., “General Atomic and Molecular Electronic Structure System”, *Journal of Computational Chemistry*, 14, 1347-1363, 1993. <https://doi.org/10.1002/jcc.540141112>
- [9] Yanai T., Tew D.P., Handy N.C., “A new hybrid exchange–correlation functional using the Coulomb-attenuating method (CAM-B3LYP)”, *Chemical Physics Letters*, 393(1-3), 51-57, 2004. <https://doi.org/10.1016/j.cplett.2004.06.011>
- [10] Stevens W.J., Krauss M., Bash H., Jasien P.G., “Relativistic compact effective potentials and efficient, shared-exponent basis sets for the third-, fourth-, and fifth-row atoms”, *Canadian Journal of Chemistry*, 70, 612-630, 1992. <https://doi.org/10.1139/v92-085>
- [11] N. Arslan, “Enantioselective transfer hydrogenation of pro-chiral ketones catalyzed by novel ruthenium and iridium complexes of well-designed phosphinite ligand”, *Phosphorus Sulfur Silicon and Related Elements*, 195(8), 628-637, 2020. <https://doi.org/10.1080/10426507.2019.1704285>
- [12] Mashuga M.E., Olasunkanmi L.O., Ebenso E.E., “Experimental and theoretical investigation of the inhibitory effect of new pyridazine derivatives for the corrosion of mild steel in 1 M HCl”, *Journal of Molecular Structure*, 1136, 127-139, 2017. <https://doi.org/10.1016/j.molstruc.2017.02.002>
- [13] Murray J.S., Sen K., “Molecular Electrostatic Potentials, Concepts and Applications”, Elsevier, Amsterdam (1996).
- [14] Khemalpure S.S., Hiremath S.M., Hiremath C.S., Katti V.S., Basanagouda M.M., Khanal G.P., Karthick T., “Structural, spectroscopic and computational investigations on (4,6-dimethyl-benzofuran-3-yl)-acetic acid hydrazide”, *Journal of Molecular Structure*, 1220, 128748, 2020. <https://doi.org/10.1016/j.molstruc.2020.128748>
- [15] Hiremath S.M., Patil A.S., Hiremath C.S., Basanagouda M., Khemalpure S.S., Patil N.R., Radder S.B., Armakovi S.J., Armakovi S., “Structural, spectroscopic characterization of 2-(5-methyl-1-benzofuran-3-yl) acetic acid in monomer, dimer and identification of specific reactive, drug likeness properties: Experimental and computational study”, *Journal of Molecular Structure*, 1178, 1-17, 2019. <https://doi.org/10.1016/j.molstruc.2018.10.007>
- [16] Sebastian Sr. S.H.R., Attia M.I., Almutairi M.S., El-Emam A.A., Panicker C.Y., Van Alsenoy C., “FT-IR, FT-Raman, molecular structure, first order hyperpolarizability, HOMO and LUMO analysis, MEP and NBO analysis of 3-(adamantan-1-yl)-4-(prop-2-en-1-yl)-1H-1,2,4-triazole-5(4H)-thione, a potential bioactive agent”, *Spectrochimica Acta Part A: Molecular and Biomolecular Spectroscopy*, 132, 295-304, 2014. <https://doi.org/10.1016/j.saa.2014.04.177>
- [17] Abad N., Lgaz H., Atioglu Z., Akkurt M., Mague J.T., Ali I.H., Chung Ill.-M., Salghi R., Essassi El M., Ramli Y., “Synthesis, crystal structure, hirshfeld surface analysis, DFT computations and molecular dynamics study of 2-(benzyloxy)-3-phenylquinoxaline”, *Journal of Molecular Structure*, 1221, 128727, 2020. <https://doi.org/10.1016/j.molstruc.2020.128727>
- [18] Bredol M., Micior J., “Preparation and characterization of nanodispersions of yttria, yttrium aluminum garnet and lutetium aluminum garnet”, *Journal of Colloid and Interface Science*, 402, 27-33, 2013. <https://doi.org/10.1016/j.jcis.2013.03.060>

- [19] Howlett P.C., Izgorodina E.I., Forsyth M., MacFarlane D.R., “Electrochemistry at Negative Potentials in Bis(trifluoromethanesulfonyl)amide Ionic Liquids”, *Zeitschrift für Physikalische Chemie*, 220, 1483-1498, 2006. <https://doi.org/10.1524/zpch.2006.220.10.1483>
- [20] Bader R.F.W., Henneker W.H., Cade P.E., “Molecular Charge Distributions and Chemical Binding”, *The Journal of Chemical Physics*, 46, 3341-3363, 1967. <https://doi.org/10.1063/1.1841222>
- [21] Henn J., Leusser D., Stalke D., “Chemical Interpretation of Molecular Electron Density Distributions”, *Journal of Computational Chemistry*. 28, 2317-2324, 2007. <https://doi.org/10.1002/jcc.20747>
- [22] Domingo L.R., “Molecular Electron Density Theory: A Modern View of Reactivity in Organic Chemistry”, *Molecules*, 21(10), 1319, 2016. <https://doi.org/10.3390/molecules21101319>
- [23] Senthilkumar K., Kanagathara N., Natarajan V., Ragavendran V., Srinivasan T., Marchewka M.K., “Single crystal X-ray diffraction, spectral characterization, evaluation of electronic and chemical reactivity of tert-butylammonium N-acetylglycinate monohydrate - A DFT study”, *Journal of Molecular Structure*, 1220, 128764, 2020. <https://doi.org/10.1016/j.molstruc.2020.128764>
- [24] Erdoğan Ş., Safi Z.S., Kaya S., Özbakır Işın D., Guo L., Kaya C., “A computational study on corrosion inhibition performances of novel quinoline derivatives against the corrosion of iron”, *Journal of Molecular Structure*, 1134, 751-761, 2017. <https://doi.org/10.1016/j.molstruc.2017.01.037>
- [25] Wu S., Qi L., Ren Y., Ma H., “1,2,4-triazole-3-thione Schiff bases compounds: Crystal structure, hirshfeld surface analysis, DFT studies and biological evaluation”, *Journal of Molecular Structure*, 1219, 128591, 2020. <https://doi.org/10.1016/j.molstruc.2020.128591>
- [26] Madkour L.H., Kaya S., Guo L., Kaya C., “Quantum chemical calculations, molecular dynamic (MD) simulations and experimental studies of using some azo dyes as corrosion inhibitors for iron. Part 2: Biseazo dye derivatives”, *Journal of Molecular Structure*, 1163, 397-417, 2018. <https://doi.org/10.1016/j.molstruc.2018.03.013>



REVERSE-ENGINEERED DBI-ESSENCE FIELD IN THE RAINBOW GRAVITY

Fatma Figen BİNBAŸ¹ *¹Department of Physics, Faculty of Science, Dicle University, Diyarbakir, TURKEY* Corresponding author: figenb@dicle.edu.tr

Abstract: The current astrophysical data sets have implied that our universe has recently entered an accelerated expansion phase. In literature, it is commonly thought that the late-time speedy enlargement behavior is caused by mysterious dark contents (dark matter, dark energy, and dark radiation) that cannot be observed directly. Although Einstein's General Theory of Relativity has provided very successful theoretical explanations and predictions, it cannot explain the aforementioned unusual nature of the cosmos. This situation has led scientists to try to create a new theoretical model for the nature of dark content. The cosmological constant, scalar fields, unified energy densities, additional dimension ideas, and modified gravity theories are among the prominent point of view. In this research, the reverse-engineering method is mainly taken into account in the rainbow gravity formalism for the DBI-essence scalar field dark energy model. As it is known, scalar field models can be introduced with the help of some fundamental physics theories, but these theories do not provide a direct way to write explicitly the self-interaction potentials that we encounter in scalar field models. Therefore, the reverse-engineering method used in this research takes a significant role while writing the self-interaction potential of a scalar field model.

Keywords: Cosmology, Quantum Gravity, Scalar Field, DBI-essence.

Received: April 26, 2022

Accepted: June 14, 2022

1. Introduction

According to the astrophysical experiments completed in recent years [1-4], our universe has entered an extraordinary period, in which it expands faster than expected. Cosmological data published by the Planck Research Group [4] indicates that the distribution of contents in our universe is found to be 4.9 % ordinary (or baryonic) matter (stars, galaxies, and everything including us), 26.8 % dark matter, and 68.3 % dark energy. The General Theory of Relativity [5] is expressed as follows:

$$R_{\mu\nu} - \frac{1}{2}Rg_{\mu\nu} = 8\pi G[(\rho + p)U_{\mu}U_{\nu} + pg_{\mu\nu}]. \quad (1)$$

The left side of this equation expresses the geometric structure of the space-time fabric, while the right side contains information about the energy-matter distribution. The quantities $R_{\mu\nu}$, R , $g_{\mu\nu}$, G , ρ , p , and U_{μ} written in the above equation correspond to the Ricci tensor, Ricci scalar, metric tensor, universal gravitational constant, energy density, pressure, and four-velocity vector, respectively. The General Theory of Relativity, which has reached the age of 107 and offers very successful results in the theoretical context, includes only the ordinary matter effect among the dominant contents of our Universe. Naturally, the need to reorganize and expand Einstein's General Theory of Relativity has emerged to explain the current observational data theoretically. According to the studies presented in

the literature, the following methods come to the fore: (i) changing the left side of the equation (modified gravity) [6-8], using the cosmology constant [9], making use of scalar field models [10-13]), (ii) changing the right side of the equation (introducing dark matter and dark energy density definitions [14-16] or unified density models [17,18]). In this study, we mainly focus our attention on the reverse-engineering method, which comparatively connects a scalar field definition and the rainbow formalism of gravity, which is a modified gravity idea that has been studied extensively in the literature [22,24]. As we emphasized in the summary of our study, some fundamental physics theories allow us to propose various definitions of scalar fields, but they do not offer useful methods, by which we can obtain explicit solutions for the self-interaction potential introduced in a scalar field model [10-13]. On the other hand, the very recent observation of gravitational waves, which was estimated first by Einstein via the General Theory of Relativity Theory [19], has increased the need for a successful quantum gravity model [20,21]. In this context, the rainbow formalism of gravity [22-24] stands out as a remarkable quantum gravity idea proposed recently in the literature. This formalism is basically built on the idea that "the energy of a test particle should affect the fabric of space-time" [22,23]. In this study, we discuss the results obtained by substituting the Friedmann-Robertson-Walker (FRW) type rainbow metric in equation (1), together with the (Dirac-Born-Infeld) DBI-essence scalar field dark energy model and compare them via the reverse-engineering method.

In this study, the rainbow formalism and the DBI-essence scalar field model, which form the basis of the research, will be briefly introduced in the second section. Subsequently, our original calculations will be given in the third section. Finally, we will highlight the main results of our research and present some suggestions for possible future research in the final section.

2. Materials And Methods

2.1. Fundamentals of Rainbow Formalism

Within the scope of this formalism, Magueijo and Smolin [23] defined a deformed equivalence principle and presented a dispersion relation, which is valid also in curvilinear coordinates. From a mathematical point of view, the rainbow formalism is basically represented by the following relation [23]:

$$f^2(\varepsilon)E^2 - g^2(\varepsilon)p^2 = m^2 . \quad (2)$$

Here, the quantities E and m represent energy and mass, respectively, while $f(\varepsilon)$ and $g(\varepsilon)$ are called rainbow functions [22-24]. On the other hand, the parameter ε corresponds to the energy of a test particle and it is written as

$$\varepsilon = \frac{E}{E_{pl}} , \quad (3)$$

where E_{pl} stands for the Planck energy. Various definitions [25-30] have been proposed in literature for the rainbow functions (the quantities γ , β and n that appear in some equations are arbitrary parameters):

$$f(\varepsilon) = \frac{1}{1-\gamma\varepsilon}, \quad g(\varepsilon) = 1, \quad (4)$$

$$f(\varepsilon) = g(\varepsilon) = \frac{1}{1-\varepsilon}, \quad (5)$$

$$f(\varepsilon) = \sqrt{1-\varepsilon^2}, \quad g(\varepsilon) = 1, \quad (6)$$

$$f(\varepsilon) = 1, \quad g(\varepsilon) = 1 + \frac{\varepsilon}{2}, \quad (7)$$

$$f(\varepsilon) = e^{-\frac{\varepsilon^2}{2}}, \quad g(\varepsilon) = 1, \quad (8)$$

$$f(\varepsilon) = \frac{e^{\beta\varepsilon}-1}{\beta\varepsilon}, \quad g(\varepsilon) = 1, \quad (9)$$

$$f(\varepsilon) = 1, \quad g(\varepsilon) = 1 + \varepsilon^n. \quad (10)$$

The Friedmann-Robertson-Walker metric, which is the basis of cosmological studies and describes the geometric structure of the Universe, points to a homogeneous and isotropic structure and is expressed mathematically as follows [31]

$$ds^2 = -dt^2 + a^2(t)[dr^2 + r^2d\theta^2 + r^2\sin^2\theta d\phi^2] \quad (11)$$

where the $a(t)$ function is known as the scale factor and indicates an expanding geometry. Within the scope of the rainbow formalism of gravity, the replacements

$$dt \rightarrow \frac{dt}{f}, \quad dx \rightarrow \frac{dx}{g}, \quad dy \rightarrow \frac{dy}{g}, \quad dz \rightarrow \frac{dz}{g} \quad (12)$$

transforms the Friedmann-Robertson-Walker metric into its rainbow gravity version [22-24]:

$$ds^2 = -\frac{1}{f^2}dt^2 + \frac{a^2(t)}{g^2}[dr^2 + r^2d\theta^2 + r^2\sin^2\theta d\phi^2], \quad (13)$$

Thus, after using equation (13) in equation (1), the extended Friedmann equations are obtained as follows [22,23]:

$$H^2 = \frac{8\pi G}{3f^2}\rho, \quad (14)$$

$$\frac{dH}{dt} = -\frac{8\pi G}{f^2}(\rho + p). \quad (15)$$

The quantity $\mathbf{H} = \frac{1}{a} \frac{da}{dt}$ is known as the Hubble parameter in literature. Besides, after taking the above results into account at the same time, the following equation is obtained for the extended conservation equation [24]

$$\frac{d\rho}{dt} + 3H(\rho + p) = 0. \quad (16)$$

2.2. Fundamentals of the DBI-essence scalar field model

This type of scalar field is described by the action integral [32]:

$$S = - \int d^4x \sqrt{-g} \left[T(\phi) \left\{ \sqrt{1 - \frac{(\frac{d\phi}{dt})^2}{T(\phi)}} - 1 \right\} + V(\phi) \right]. \quad (17)$$

Here, ϕ is the scalar field, g is the determinant of the metric tensor, $V(\phi)$ is the self-interaction potential, and $T(\phi)$ is the warped brane tension. Within the scope of this model, the energy density and pressure quantities are written as follows [33]:

$$\rho_{DBI} = (\eta - 1)T(\phi) + V(\phi), \quad (18)$$

$$p_{DBI} = \left(\eta - \frac{1}{\eta}\right)T(\phi) - V(\phi), \quad (19)$$

where

$$\eta = \left(1 - \frac{(\frac{d\phi}{dt})^2}{T(\phi)}\right)^{-\frac{1}{2}} > 1. \quad (20)$$

Therefore, we see that it should be $\left(\frac{d\phi}{dt}\right)^2 > T(\phi)$ [33]. In addition to this, we get the subsequent relation by making use of equations (18) and (19),

$$\rho_{DBI} + p_{DBI} = \left(\eta - \frac{1}{\eta}\right)T(\phi). \quad (21)$$

Note that this quantity must always take positive values [33]. Finally, the equation-of-state parameter for the DBI-essence scalar field model is obtained as follows:

$$\omega_{DBI} = \frac{p_{DBI}}{\rho_{DBI}} = \frac{\frac{\eta^2-1}{\eta}T(\phi)-V(\phi)}{(\eta-1)T(\phi)+V(\phi)}. \quad (22)$$

We can now apply the reverse-engineering method, which is based on the idea of making a comparison between the rainbow gravity formalism and the DBI-essence scalar field model, to the preliminary definitions and calculations.

3. Results and Discussions

From equations (14) and (15), the following relations are obtained for the energy density ρ and the pressure p

$$\rho = \frac{3f^2}{8\pi G} H^2, \quad (23)$$

$$p = -\frac{f^2}{8\pi G} \left[\frac{dH}{dt} + 3H^2 \right]. \quad (24)$$

Thus, for the equation-of-state parameter, we reach the following result

$$\omega = \frac{p}{\rho} = -\frac{\frac{dH}{dt} + 3H^2}{3H^2}. \tag{25}$$

According to the reverse-engineering method, one can assume $\rho = \rho_{DBI}$ for the energy density, $p = p_{DBI}$ for the pressure, and $\omega = \omega_{DBI}$ for the equation-of-state parameter. According to these assumptions, we can write

$$\frac{d\phi}{dt} : \frac{\rho_{DBI} + p_{DBI}}{\eta} \rightarrow \frac{\rho + p}{\eta}, \tag{26}$$

$$T(\phi) : \frac{\left(\frac{d\phi}{dt}\right)^2 (\rho_{DBI} + p_{DBI})^2}{(\rho_{DBI} + p_{DBI})^2 - \left(\frac{d\phi}{dt}\right)^4} \rightarrow \frac{\left(\frac{d\phi}{dt}\right)^2 (\rho + p)^2}{(\rho + p)^2 - \left(\frac{d\phi}{dt}\right)^4} \tag{27}$$

$$V(\phi) : \frac{\left(\frac{d\phi}{dt}\right)^2 \rho_{DBI} - p_{DBI}(\rho_{DBI} + p_{DBI})}{\left(\frac{d\phi}{dt}\right)^2 + \rho_{DBI} + p_{DBI}} \rightarrow \frac{\left(\frac{d\phi}{dt}\right)^2 \rho - p(\rho + p)}{\left(\frac{d\phi}{dt}\right)^2 + \rho + p}. \tag{28}$$

When the expressions presented in equations (23) and (24) are used in equations (26), (27) and (28), the following results are obtained:

$$\frac{d\phi}{dt} = -\frac{f^2}{8\pi\eta G} \frac{dH}{dt}, \tag{29}$$

$$T(\phi) = \frac{f^4 \left(\frac{dH}{dt}\right)^2}{(8\pi G)^2 - \eta^2 f^4 \left(\frac{dH}{dt}\right)^2} \tag{30}$$

$$V(\phi) = \frac{3f^4 H^2 \frac{dH}{dt} - 8\pi G \eta^2 f^2 \left(\frac{dH}{dt} + 3H^2\right)}{f^2 \frac{dH}{dt} - 8\pi G \eta^2}. \tag{31}$$

At this stage, the results are given in equations (29), (30), and (31) can be used for a graphical analysis with the help of specific forms of rainbow functions (please check equations (4)-(10) introduced before) and some solutions of Hubble parameter. Three well-known Hubble parameter formulations are presented in Table 1.

Table 1. Custom scale factor and Hubble parameter selections

Phase	$a(t)$	$H(t)$
Radiation phase [34]	$a_0 t^{\frac{1}{2}}$	$\frac{1}{2t}$
Matter phase [35]	$a_0 t^{\frac{2}{3}}$	$\frac{2}{3t}$
Energy phase [35]	$a_0 e^{H_0 t}$	H_0

As an example, when we use the choice of rainbow functions presented in equation (6) and the energy phase solution of the Hubble parameter, we get the following results:

$$\phi = \phi_0 = \text{constant}, \tag{32}$$

$$T(\phi) = 0 \tag{33}$$

$$V(\phi) = 3(1 - \varepsilon^2)H_0^2. \tag{34}$$

4. Conclusions

The main purpose of this research is to apply a method that we can express mathematically the self-interaction potential quantity $V(\phi)$ of a scalar field dark energy model. In order to achieve this aim, the reverse-engineering between the rainbow gravity formalism and the DBI-essence scalar field definition has been studied. The effects of rainbow functions on the scalar field model have been clearly demonstrated from the calculations performed with the help of the rainbow gravity framework. It would be appropriate to emphasize here that it is possible to reach additional cosmological discussions by using the obtained theoretical results in a graphic analysis. On the other hand, we can expand our research by applying the comparative method introduced in this study to different scalar field models such as the tachyon [10], quintessence [12], k-essence [36], and the dilaton [37] fields.

Ethical Statements

The author declares that this document does not require an ethics committee approval or any special permission. Our study does not cause any harm to the environment.

Conflict of interest

The authors declare no conflict of interest.

Authors Contributions

FFB carried out calculations and wrote the first draft of the manuscript.

References

- [1] Bennet, C.L., et al., "First-Year Wilkinson Microwave Anisotropy Probe (WMAP) Observations: Preliminary Maps and Basic Results", *The Astrophysical Journal (Supplement)* 148, 1, 2003.
- [2] Tegmark, M., et al., "Cosmological parameters from SDSS and WMAP", *Physical Review D*, 69, 103501, 2004.
- [3] Perlmutter, S., et al., "Measurements of W and L from 42 High-Redshift Supernovae", *The Astrophysical Journal (Supplement)* 517, 2, 1999.
- [4] Ade, P.A.R., et al., "Planck 2013 results. XVI. Cosmological parameters", *Astronomy and Astrophysics*, 571, A16, 2014.
- [5] Einstein, A., "Zur Allgemeinen Relativitätstheorie", *Sitzungsber. Preus. Akad. Wiss. Berlin (Math. Phys.)*, 47, 778-786, 1915.
- [6] Sotiriou, T.P. and Faraoni, V., "f(R) theories of gravity", *Review of Modern Physics*, 82, 451, 2010.
- [7] Hehl, F.W., Von Der Heyde, P., Kerlick, G.D. and Nester, J.M., 1976, "General relativity with spin and torsion: Foundations and prospects", *Review of Modern Physics*, 48, 393, 1976.
- [8] Mikhail, M.I. and Wanas, M.I., "A generalized field theory. 1. Field equations", *Proceedings of Royal Society London Ser. A, The Journal of Mathematical Physics* 356, 471, 1977.
- [9] Copeland, E.J., Sami, M. and Tsujikawa, S., "Dynamics of dark energy", *International Journal of Modern Physics D*, 15, 1753, 2006.
- [10] Pasqua, A., Khodam-Mohammadi, A., Jamil, M. and Myrzakulov, R., "Interacting Ricci Dark Energy with Logarithmic Correction". *Astrophysics Space Science*, 340, 199, 2012.
- [11] Jamil, M., Karami, K. ve Sheykhi, A., "Restoring New Agegraphic Dark Energy in RS II Braneworld", *International Journal of Theoretical Physics*, 50, 3069, 2011.

- [12] Sheykhi, A. and Bagheri, A., “Quintessence Ghost Dark Energy Model”. *Europhysics Letters*, 95, 39000, 2011.
- [13] Sheykhi, A., Movahed, M.S. and Ebrahimi, E., “Tachyon Reconstruction of Ghost Dark Energy”, *Astrophysics and Space Science*, 339, 93. 2012
- [14] M. Salti, H. Yanar, O. Aydogdu, and K. Sogut, “Dynamics of ghost scalar fields in Kaluza–Klein cosmology”, *Astrophysics and Space Science* 362, 207, 2017.
- [15] Ebrahimi, E. and Sheykhi, A., “Scalar field reconstruction of power-law entropy-corrected holographic dark energy”, *Physica Scripta*. 04, 045016, 2011.
- [16] Veneziano, G., “U (1) without instantons”, *Nuclear Physics B* 159, 213, 1979.
- [17] Padmanabhan, T., “Cosmological Constant - the Weight of the Vacuum”, *Physics Reports*, 380, 235, 2003.
- [18] Cai, Y.F., Saridakis, E.N., Setare, M.R. and Xia, J.Q., “Quantum Cosmology: Theoretical implications and observations”, *Physics Reports*, 493, 1, 2010.
- [19] Abbott, B.P., et al., (LIGO Scientific Collaboration and Virgo Collaboration), “Observation of Gravitational Waves from a Binary Black Hole Merger”, *Physical Review Letters*, 116, 061102, 2016.
- [20] Kiefer, C., *Quantum Gravity, 2nd edition*, Oxford University Press, Oxford, 2007.
- [21] Carlip, S., “Quantum gravity: a progress report”, *Reports on Progress in Physics*, 64, 885, 2001.
- [22] Magueijo, J. and Smolin, L., “Gravity's Rainbow”, *Classical and Quantum Gravity*, 21, 1725, 2004,
- [23] Magueijo, J. and Smolin, L., “Generalized Lorentz invariance with an invariant energy scale”, *Physical Review D*, 67, 044017, 2003.
- [24] Ashour, A, Alcheikh, M. and Chamoun, N., “General modified Friedmann equations in Rainbow flat universe, by thermodynamics”, *European Physical Journal C*, 79, 127, 2019.
- [25] Ling, Y., Li, X. and Zhang, H., “Thermodynamics of Modified Black Holes From Gravity's Rainbow”, *Modern Physics Letters A*, 22, 2749,2007.
- [26] Leiva, C., Saavedra, J. and Villanueva, J., “Geodesic Structure of the Schwarzschild Black Hole in Rainbow Gravity”, *Modern Physics Letters A*, 24, 1443,2009.
- [27] Liu, C.Z. and Zhu, J.Y., “Hawking radiation and black hole entropy in a gravity’s rainbow”, *General Relativity and Gravitation*, 40, 1899, 2008.
- [28] Hendi, S.H., Faizal, M., Panah, B.E. and Panahiyan, S., “Charged dilatonic black holes in gravity’s rainbow”, *European Physical Journal C*, 76, 296, 2016.
- [29] Feng, Z.-W. and Yang, S.-Z., “Thermodynamic phase transition of a black hole in rainbow gravity”, *Physics Letters B*, 772,737-742,2017.
- [30] Amirabi, Z., Halilsoy, M. and Mazharimousavi, S.H., “Thin-shell wormholes in rainbow gravity”, *Modern Physics Letters A*, 33, 1850049, 2018.
- [31] Ellis, G.F.R. and van Elst, H., "Cosmological models (Cargèse lectures 1998)". In Marc Lachièze-Rey (ed.). Theoretical and Observational Cosmology. NATO Science Series C. 541. 1–116, 1999.

- [32] Martin, J. and Yamaguchi, M., “DBI-essence”, *Physical Review D*, 77, 123508, 2008.
- [33] Debnath, U., and Jamil, M., “Correspondence between DBI-essence and modified Chaplygin Gas and The Generalized Second Law Of Thermodynamics”, *Astrophysics and Space Science*. 335, 545, 2011.
- [34] Padmanabhan, T., “*Structure Formation in the Universe*”, Cambridge University Press, Cambridge, 1993.
- [35] Ryden, B., “*Introduction to Cosmology*”, Cambridge University Press, Cambridge, 2016.
- [36] Chiba, T., Okabe, T. and Yamaguchi, M., “Kinetically driven quintessence”, *Physical Review D* 62, 023511, 2000.
- [37] Piazza, F. and Tsujikawa, S., “Dilatonic ghost condensate as dark energy”, *Journal of Cosmology and Astroparticle Physics* 7, 4, 2004.

**CHARACTERIZATION OF $\text{Cu}_2\text{MnSnS}_4$ THIN FILMS FABRICATED BY SPIN COATING****Canan AYTUĞ AVA**^{*1, 2} **Şilan BATURAY**³ ¹ Dicle University, Science and Technology Application and Research Center, 21280, Diyarbakir, Turkey² Dicle University, Department of Physics, Institute of Natural Sciences, 21280, Diyarbakir, Turkey³ Dicle University, Faculty of Science, Department of Physics, 21280, Diyarbakir/Turkey* Corresponding author; cananaytug@hotmail.com

Abstract: $\text{Cu}_2\text{MnSnS}_4$ (CMTS) thin films are affected by several parameters related to different annealing including sulphur flux rate. In this paper, nontoxic CMTS samples were fabricated onto a soda glass lime substrate by spin-coating to investigate the effect of various sulphur flux rates on the crystal, topological and optical properties by using X-Ray diffraction, scanning electron microscopy, atomic force microscopy, and ultraviolet-visible spectrophotometer, respectively. The X-ray diffraction pattern showed that CMTS films had a main (112) oriented peak and crystallized in a stannite structure. The crystal parameters of CMTS thin films were changed depending on the increase of sulphur flux rate annealed at 550 °C for 90 minutes. The minimum value of dislocation value for CMTS film annealed 30 sccm sulphur flux rate showed the better crystallinity of the film. The scanning electron microscopy images of films showed a decrease in the particle size related to the increased flux of sulphur. AFM images showed that CMTS samples annealed at 40 sccm H_2S : Ar had some clumping in the surface topology while CMTS samples annealed at 30 sccm H_2S : Ar thin films were uniformly distributed. Ultraviolet-visible spectroscopy (Uv-vis) measurements of the thin films revealed that CMTS film absorbed a high amount of photons as the sulphur flux increased. The energy band gap for the CMTS films was 1.22 and 1.15 eV for 30 sccm and 40 sccm H_2S : Ar, respectively. This work showed that different sulphur flux has a significant effect on the structural and morphological properties of CMTS thin films.

Keywords: Sulphur Flux, Thin Film, Optical Properties, Absorbance

Received: March 30, 2022

Accepted: June 14, 2022

1. Introduction

Recently, the requirement for energy is rapidly increasing in both developed and developing countries due to rapid population growth, industrialization, and many other reasons. It is not possible to compensate for this demand with fossil fuels. Therefore, the use of renewable, cheap, and clean energy sources has become compulsory instead of fossil energy resources consumed rapidly and consequently polluting the environment. In recent years, solar cell technologies of nanostructure thin film based on chalcogene thin-film materials, particularly CuInSe_2 [1], CuInGa [2], and CdTe [3], are still used in most of the production of photovoltaic devices. Nevertheless, the scarcity of some materials including In and Te in the crust of earth limits the future of solar cells based on CIGS and CdTe , which the extremely expensive [4]. Another problem is that CdTe -based solar cells are a threat to both the environment and health because Cd is a toxic element [5]. Because of these problems, researchers have sought to find more abundant and harmless materials on the earth.

Therefore, direct band gap metal chalcogen thin films have greatly reduced production potential for both raw material and processing requirements in photovoltaic technology. Because $\text{Cu}_2\text{ZnSnS}_4$ (CZTS) is one of the most exciting alternatives as an absorber layer in thin-film solar cells [6]. As an alternative to quaternary $\text{Cu}_2\text{CoSnS}_4$ (CCTS), CuInGaS_2 (CIGS), photovoltaic absorbers have attracted considerable attention in recent years [7]. CMTS is a semiconductor with multiple applications [8,9]. Thus far, solar cells based on $\text{Cu}_2\text{MnSnS}_4$ absorbers with conversion efficiencies of up to PCE = 1.8% have been developed [10], which form a tetragonal crystal structure similar to kesterite. It has a direct bandgap at 1.61 eV and a high absorption coefficient [11]. Therefore, it may be resistant to cation disorder, similar to the stannite $\text{Cu}_2\text{FeSnS}_4$. Liang et al. describe the synthesis of stannite and wurtzite CMTS nanocrystals via a hot injection approach [12].

CMTS is an excellent p-type semiconducting material that has high absorption coefficient, direct energy band gap varying between 1.1 and 1.3 eV [13-15], and non-toxic and abundant elements in the earth. CMTS solar cells reached an 8.4% yield [16]. Zou et al. found that the nature of the sulfur precursor determines the formation and phase purity of the CZTS material synthesized by the hydrothermal reaction. Furthermore, this phase-control mechanism can be expanded to other quaternary Cu_2MSnS_4 ($\text{M} = \text{Cd}^{2+}, \text{Mn}^{2+}$) nanocrystal syntheses, where the relative reactivity of M^{2+} and the sulfur precursor plays a key role [17].

Shape-controlled topologies have a significant role in the thin film's properties in the nanoscale region. Also, a lot of metals can be employed as doping elements to improve the quality of crystalline thin films' properties with excellent physical and chemical properties of nanostructured thin films. There are various methods to accumulate CMTS absorbers. These methods include electrochemical technique, sol-gel spin coating method, pulsed laser fabrication, thermal evaporation chemical vapor deposition, and magnetron sputtering, [18-23]. The sol-gel spin coating technique has some advantages. Usually, the spin coating is less costly than other methods and requires a simple preliminary preparation. Also, the sol-gel spin coating is one of the best coating methods for obtaining homogeneous and controlled films. For instance, Liu et al. deposited both undoped and 10% Na-doped CZTS thin films using the spin coating technique. They have shown that Na doping can suppress deleterious antisite defects and increase the grain size of CZTS thin films. They also reported improving electrical properties (increase in carrier concentration, mobility, and conductivity due to the NaZn shallow acceptor defect. The study revealed that the power conversion efficiency of the CZTS-based solar cells increased by 44% after Na-doping [24].

Sulphur flux has a large impact on the structural and optical properties of CMTS film. Thus, to get more light on the understanding of the effect of sulphur flux on the physical properties of CMTS films, more experimental studies are necessary. Although there are studies on CMTS films, there is limited information on the effects of sulphur flux on the structural and optical properties of CMTS films using the spin coating technique. Maeda et al. studied the influence of sulfurization temperature on preheated CZTS thin films. They annealed the film between 350 and 600 °C for 1 h under a 5% $\text{H}_2\text{S} + \text{N}_2$ atmosphere. The structural properties of the films indicated that the suitable sulfurization temperature in this work is not lower than 400 °C because of the formation of secondary phases including Cu_xS and sulfurization at 560 °C is the optimum condition in terms of absorption coefficient [25].

The structure and microstructure of synthetic CMTS depend, among other things, on the nature of these precursors. The development of methods to synthesize CMTS as an absorber in solar cells containing abundant metals that are commonly found on Earth is important to the photovoltaic community due to the similarity of its crystal structure and bandgaps compared with CZTS/CZTSSe, and alongside its increased abundance of Mn compared to Zn [26].

We studied the influence of $\text{H}_2\text{S} : \text{Ar}$ (1:9) flow on the structural, topological, and optical properties of CMTS film. In this study, CMTS samples were formed on glass substrate by using the spin

coating method with different annealing conditions in order to get more information about $\text{Cu}_2\text{MnSnS}_4$ quaternary semiconductor which needed further widespread works on crystal structure, morphological and optical properties. The physical properties of CMTS thin films formed by different sulphur flux rates were investigated according to production conditions. The properties of the obtained thin film were analyzed by X-Ray diffraction (XRD) for crystal structure analysis, scanning electron microscopy (SEM), atomic force microscopy (AFM) for morphological properties, and ultraviolet-visible (UV-vis) spectrophotometry.

2. Experimental

2.1. Preparation of CZTS films

$\text{Cu}_2\text{MnSnS}_4$ films at various annealing conditions were deposited on well-cleaned glass substrates by the spin-coated method at a 240°C substrate temperature. CMTS thin films at two different annealing conditions were deposited by employing a solution containing 0.1 M cupric chloride (CuCl_2), 0.1 M manganese chloride (MnCl_2), and 0.1 M tin (II) chloride dihydrate ($\text{Cl}_2\text{Sn}\cdot 2\text{H}_2\text{O}$) as copper, manganese and tin source, respectively. 0.269 g of cupric chloride, 0.252 g of manganese chloride, and 0.451 g of tin (II) chloride dehydrate separately stirred in 20 ml of ethanol, glacial acetic acid (GAA), and a small amount of diethanolamine to regulate pH values for 3 h at 300 K. During the preparation of homogenous solutions, manganese chloride solution was added into cupric chloride solution, and finally, the corresponding amount of tin (II) chloride dihydrate solution was added to manganese chloride/cupric chloride solution. To obtain clear films and remove any residual waste, the SLG substrates were cleaned by boiling in sufficient quantities mixture of H_2O (distilled water), NH_3 (ammonia), and H_2O_2 (hydrogen peroxide) at 105°C and then in sufficient quantities mixture of H_2O , H_2O_2 , and HCl (hydrochloric acid) at 105°C before fabrication process. Then, each SLG substrate was cleaned in deionized water for 3 min and dried. After obtaining the final solutions and cleaning the substrates, the CMTS films with 2:1:1 stoichiometric ratios were spin-coated on substrates at a rate of 5000 rpm for 55 s in air condition. The final solutions were grown onto the substrate by layer and layer and obtained layers were preheated to 240°C for 10 min in air condition which was seen in Figure 1. Having obtained 10 layers of CMTS films, the obtained samples were gradually annealed in the furnace at 30 and 40 sccm H_2S : Ar (1:9) flows for 90 minutes at 550°C , respectively. The sample names were given CMTS (I) and CMTS (II) for 30 sccm and 40 sccm sulphur flux, respectively.

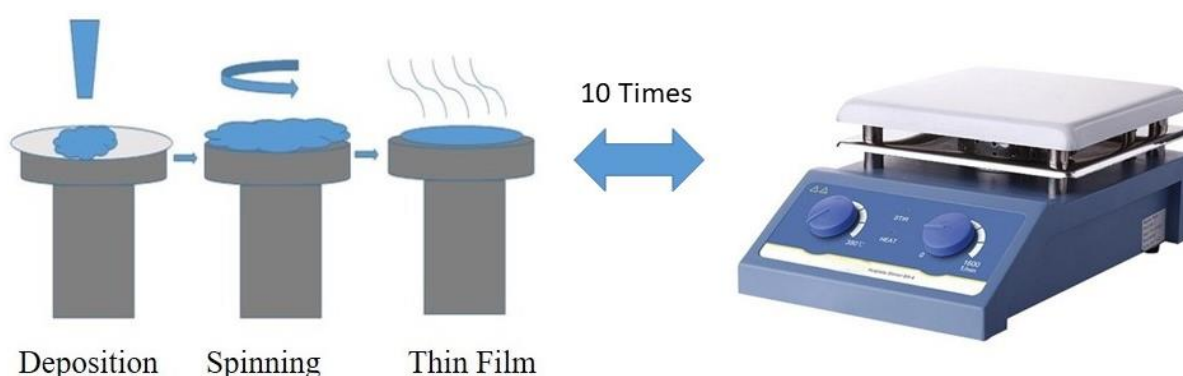


Figure 1. Spin coating processing of thin film

2.2. Characterization

The structural properties including phase identification and crystallographic construction of the obtained films were recorded via X-ray diffractometer patterns with monochromatic Cu K α radiation using a Bruker D8 Advance diffractometer. The effect of sulphur flux on the CMTS's structural, morphological, and optical properties was investigated in this study. The structural properties including phase identification and crystallographic construction of the obtained films were recorded via X-ray diffractometer patterns with monochromatic Cu K α radiation using a Bruker D8 Advance diffractometer in the 2θ ranges of 20–60°, step size = 0.02°, step time = 1 s, $\lambda = 1.54187\text{\AA}$ and 40 kV operating voltage as well as the current of 40 mA. The surface morphology of the films was investigated by SEM FEI Quanta 250 FEG scanning electron microscopy and Park System XE-100 atomic force microscopy AFM. The absorbance and the change of optical energy band gap of the obtained samples were recorded with a UV-Vis Spectrophotometer between the wavelength of 1100– 300nm.

3. Results and Discussion

3.1. Structural properties

XRD spectrum played a much more important role in determining the orientation of peaks and crystalline properties of the obtained samples. Figure 2 displays the XRD data of the CMTS film related to sulphur flux rate annealed in a quartz furnace at 550 °C. The XRD patterns of the CMTS(I) sample which exhibited $2\theta \approx 28.23^\circ$ could be indexed to the (112) planes of the stannite CMTS thin film, and the weak diffraction peaks at 46.64° and 47.13° could be indexed to the (220) and (204) planes of CMTS, respectively. As seen in Figure 2, the fact that the XRD patterns of the sample annealed at 40 sccm sulphur flux rate exhibiting a considerable sharpening peak which indicates a strong main peak around $2\theta \approx 28.72^\circ$ could be indexed to the (112) planes of the kesterite $\text{Cu}_2\text{MnSnS}_4$ thin film, and the weak diffraction peaks at 47.55°, and 56.40°, could be indexed to the (112), (204), and (312) planes of a single zinc-blende structure, respectively.

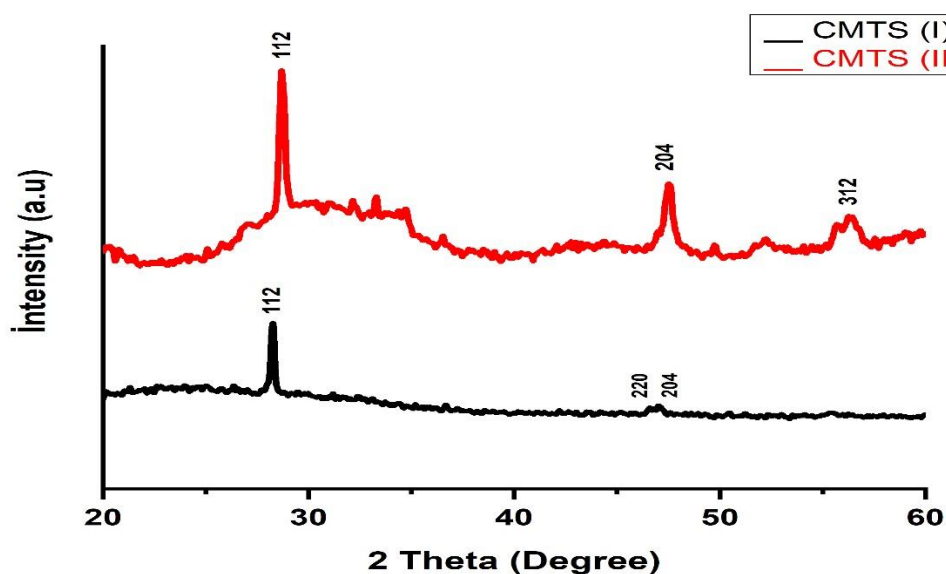


Figure 2. XRD pattern of CMTS thin film

These results showed that the samples crystallized in a single zinc-blende structure owing to the absence of (101), (220), (204), and (312) with the structure of kesterite $\text{Cu}_2\text{MnSnS}_4$. Yang et al. [27] indicated that CMTS films obtained by sol-gel method crystallized in a similar structure which was associated with the cations with the random distribution. All these films annealed at 30 and 40 sccm sulphur flux rate showed the main (112) oriented peak. The peak's intensity and full width at half maximum (FWHM) value of the main XRD diffraction peak became sharp and narrower with the increase in the sulphur flux rate, CMTS(I) indicating that (112) orientation had better crystallinity. The calculated interplanar spacing (d), the crystal size (D), the values of strain, and the dislocation density (δ) of all peaks for the CMTS thin films were given in Table 1. As seen in Table 1, the position of main peak 112 planes shifted from 28.23° to 28.72° for the films with increasing H_2S : Ar flow rate. This shift was attributed to the increase of sulphur flux rate effect on the crystal structure of the obtained CMTS samples. As the sulphur flux rate increased from 30 to 40 sccm, a decrease in the FWHM and a change in the intensity of the all CMTS peak obtained by XRD data could be seen in Figure 2. The D value of the CMTS thin film was the smallest (24.45 nm), corresponding to the (204) peak for 40 sccm H_2S : Ar flows. The Scherrer's equation which was used to determine the D value of obtained samples from the XRD data was described as:

$$D = k\lambda/\beta\cos\theta \quad (1)$$

where λ was the wavelength of the XRD measurement system ($\lambda = 1.540056 \text{ \AA}$), β was the maximum FWHM value of the peaks, θ was the Bragg's angle in degree, and k was the constant which showed shape factor ($k = 0.89$). As seen in Table 1, the D corresponding to the main planes for the sample annealed at 30 sccm (53.2 nm) was higher than the one acquired at 40 sccm sulphur flux rate (28.8 nm). The calculated results displaying the D value of the CMTS films changed with Sulphur flux rate. The largest crystal size value of the main peak showed the good crystalline quality of the sample.

Table 1. Crystal parameters of CMTS thin films grown by spin coating

Sample	2 θ (degree)	Calculated d (\AA)	FWHM (degree)	Crystal Size (\AA)	Strain	Orientation
CMTS (I)	28.23	3.16	0.16	5.32	0.28	112
	46.64	1.95	0.20	4.54	0.20	220
	47.13	1.93	0.24	3.71	0.24	204
CMTS (II)	28.72	3.11	0.30	2.88	0.51	112
	47.55	1.91	0.37	2.45	0.37	204
	56.40	1.63	0.26	3.63	0.21	312

d values of the all CMTS quaternary semiconductor were calculated by the Bragg's equation [28]:

$$2d\sin\theta = n\lambda \quad (2)$$

n was a constant which indicated the order of diffraction. The calculated interplanar spacing value of the 40 sccm sulphur flux rate thin films was lower than that of 30 sccm sulphur flux rate thin film (Table 1). n was a constant which indicated the order of diffraction. As seen in Table 1, the calculated interplanar spacing value of the CMTS(II) thin film was lower than that of the CMTS(I) thin film.

The δ value of CMTS film was calculated from the following relation [29]:

$$\delta = \frac{1}{D^2} \quad (3)$$

ε value of all films which is one of the significant factors negatively affecting the crystal structure was calculated by the following equation [30]:

$$\varepsilon = \beta \cos \theta / 4 \quad (4)$$

The calculated δ values of the main peak for 30 sccm sulphur flux rate changed between $3.54 \times 10^{14} \text{ m}^{-2}$ and $7.25 \times 10^{14} \text{ m}^{-2}$. The calculated δ values of the main peak for 40 sccm sulphur flux rate changed between $7.62 \times 10^{14} \text{ m}^{-2}$ and $12.09 \times 10^{14} \text{ m}^{-2}$. The minimum value of calculated δ obtained for CMTS film annealed 30 sccm sulphur flux showed better crystallinity of the film because calculated δ values were measurement of the amount of defect. As shown in Table 1, dislocation density displayed an increasing tendency from a value of $3.54 \times 10^{14} \text{ m}^{-2}$ to a value of $7.25 \times 10^{14} \text{ m}^{-2}$ and gave the smallest value of $3.54 \times 10^{14} \text{ m}^{-2}$ for the CMTS (I) thin film annealed at $550 \text{ }^\circ\text{C}$, corresponding to the maximum value of crystal size. Since the dislocation value was a number of defects in a crystal structure, therefore, the minimum dislocation value obtained in CMTS (I) film approved the good crystallinity of the thin film. Very similarly, the strain value of the CMTS (II) sample for the main peak increased for the samples. Very similarly, the strain value of the annealed at 40 sccm H_2S : Ar flows for the main peak increased for the samples. It was seen from these results that the increase of crystal size for CMTS thin film annealed at 30 sccm H_2S : Ar flows was owing to the decrease in strain value. The ε value was consistent with the enlargement of the d value of main plane. The formation of the defect center could be the induced presence of internal compressive strain [31]. A similar relationship between D and ε and δ was reported. Chen et al. reported that obtained CMTS films were grown by sol-gel technique and annealed with the increase of temperature [32]. It was indicated that while the D increased from 23.41 to 46.82 nm, the strain of the samples decreased from 9.7×10^{-3} to 1.4×10^{-3} and the δ value displayed a decrease from 18×10^{14} to $7 \times 10^{14} \text{ lines/m}^2$ and obtained the lowest value of $4.5 \times 10^{14} \text{ lines/m}^2$ for the samples annealed at $580 \text{ }^\circ\text{C}$ in the furnace.

3.2. Morphologic analyses

The induced surface changes by varying sulphur flux were studied by SEM, as shown in Figure 3(a-b). According to the SEM images in Figure 3 (a-b), the particle size reduction occurred when the annealing time duration was increased from 30 to 40 sccm sulphur flux rate. It could be suggested that an increase in the flux rate of sulphur could cause a decrease in particle size. Also, when the sulphur flux rate was increased from 30 to 40 sccm, the larger particles could be fragmented into smaller-sized particles. It was said that when the sulphur flux rate was increased, the particle growth deteriorated. The top observation SEM images displayed remarkable modifications with the variation of sulphur flux. Indeed, the film surface of the CMTS(II) sample was covered with randomly spread spherical grains in addition to visible agglomerated grains while the surface morphology of the CMTS(I) film appeared to be more uniform. These changes in surface morphology would have strong effects on optical properties including energy band gap and absorbance. Also, the SEM images of the samples were consistent with the crystal parameters acquired from XRD. In particular, there was a spongy growth containing tiny particles on the thin films [33] and larger particles were shaped on it. Conversely, region-by-region large particle size could occur at the high annealing temperature at high sulphur flux [33, 34]. The results from the study carried out by Olgar et al. of the surface topology of the thin films obtained by the sulphur flux rate at $550 \text{ }^\circ\text{C}$ annealed temperature utilizing different sulphurization times displayed similar results to our studies [35].

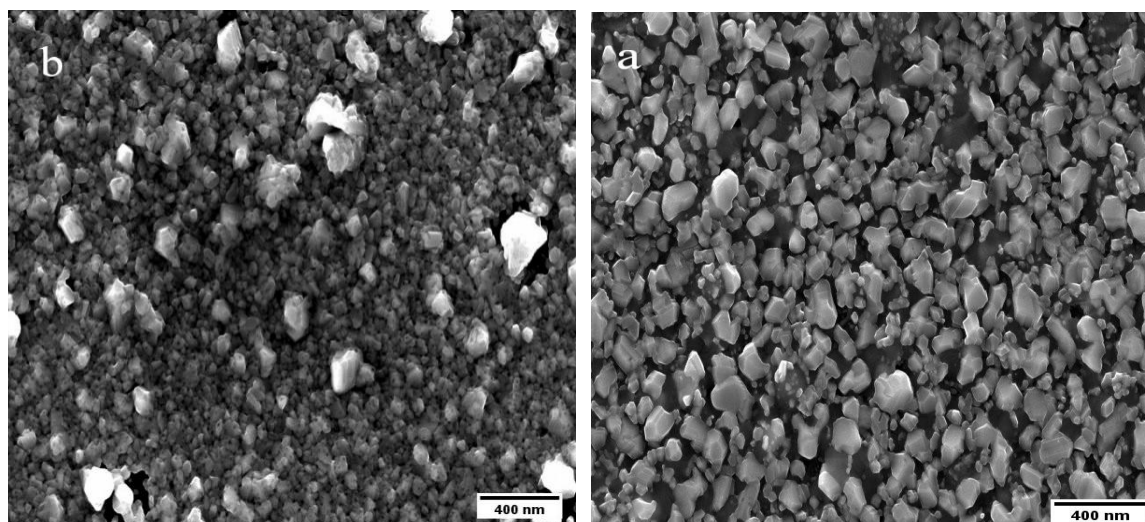


Figure 3 (a-b). a) SEM images of CMTS (I) film, b) SEM images of CMTS (II) film

AFM images were obtained using Park System XE-100 to get the correlation between sulphur flux rate and the film topology. All the AFM images morphology was gained by scanning square areas of $12,5 \mu\text{m} \times 12,5 \mu\text{m}$ at a temperature of 273 K. The figures showed the thin films with the structure of grain particles. The 3-D images of AFM of different annealing including sulphur flux rate were given in Figure 4. The figures indicated a $12,5 \mu\text{m} \times 12,5 \mu\text{m}$ area of the thin films with the structure of rod-like and grain particles. The results from obtained AFM images revealed that CMTS thin films were relatively smooth in the valley region while many crystals-like structures were in the hill region which displayed certain orientations. It was seen in AFM image that CMTS(II) sample had some clumping on its surface while the surface morphology of the CMTS(I) film appeared almost uniform. The CMTS film surface was not homogenous. It could be said that AFM images were consistent with the film structure acquired from SEM images.

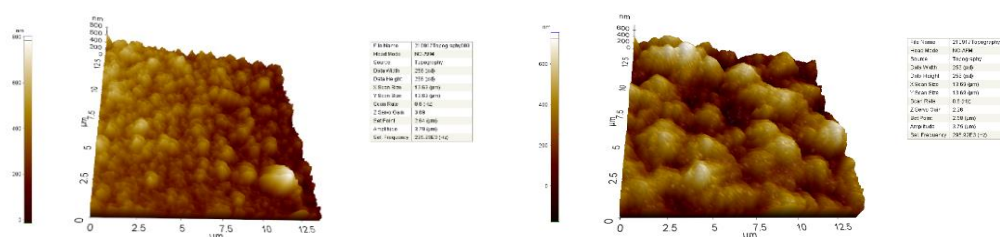


Figure 4. AFM images of CMTS(I) and CMTS(II) thin film, respectively

3.3. Optical properties

Absorbance and energy band gap is one of the most important optical parameters for CMTS thin film. Absorption of the thin films grown on substrates using spin-coating was measured in the range of 1100–300 nm under monochromatic light. The absorption spectrum of the samples implemented by spin coating was shown in Figure 5. It was observed that as the sulphur flux rate of the obtained films increased, they absorbed a high amount of photons. Photon absorption of obtained thin films was reduced in the near-infrared wavelength region.

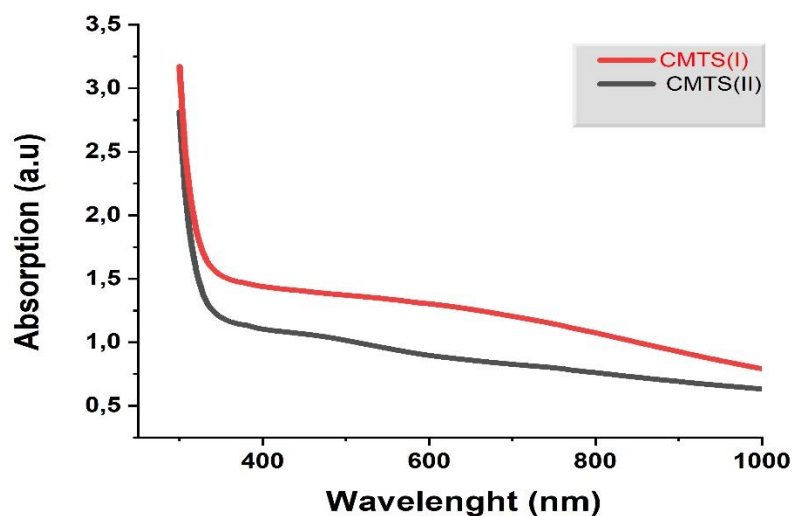


Figure 5. Absorption spectra of thin films

It could be said that the change in absorption values was a result of the different crystal nature of the films and the Moss-Burstein effect [36]. The obtained results showed that the optical properties of CMTS films were modified depending on the sulphur flux rate. The variation in the absorption value of the films indicated that CMTS films could be applied in various optical applications including optical windows and this sample was suitable material for UV filter production.

The band-gap (E_g) of the CMTS samples was calculated using the relation of Tauc [37].

$$\alpha h\nu = A(h\nu - E_g)^2 \quad (5)$$

where A is a constant, $h\nu$ is photon energy and the value of n was taken to be $1/2$. Figure 6. showed the plot of the optical energy band gap which was calculated by a straight line of $(\alpha h\nu)^2$ (versus $(h\nu)$) in Tauc plot. As seen in the figure, the energy band gap was found as 1.22 and 1.15 eV for CMTS(I) and CMTS(II) thin film, respectively. According to XRD and SEM results, the crystal size decreased and the density of grain increased with the increase of $H_2S: Ar$ (1:9) flows. Thus, the possibility of the scattering of the electron at grain boundaries decreases, and electronic shift from the valence band to the conduction band occurs more easily, which outcomes in the decreasing of energy band gap value.

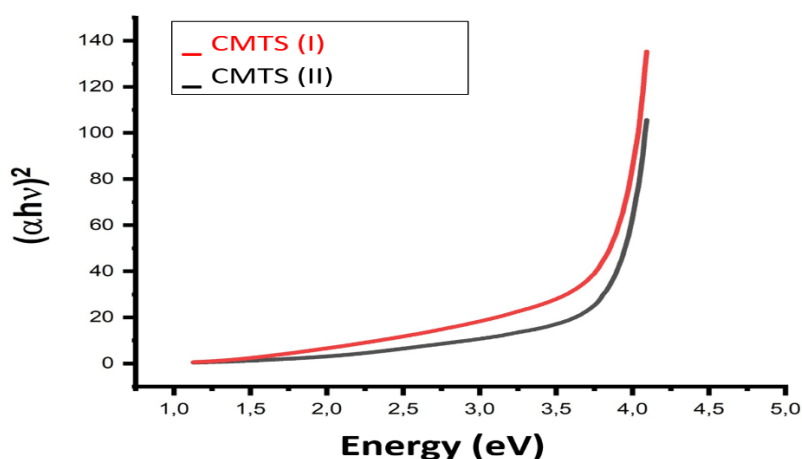


Figure 6. The energy band gap of thin films

The seen change in E_g value might be because of the difference in the crystallinity nature of the film. The decreasing of energy band gap values was owing to the effect of the change of crystalline quality in obtained films. Chen et al indicated that the (E_g) values of CMTS quaternary semiconductor films were changed between 1.62–1.14 eV related to the temperature of post-annealing [32]. Yu et al. [38] reported that the energy band gap decreased related to the rise of the Cu/(Mn + Sn) ratio which improved the photovoltaic performance. Paier et al. reported that the energy band gap of films changed to higher energies as Cu/(Zn+Sn) decreased [39]. This change was due to the fact that the valance band of films was composed of a linear combination with antibonding between Cu 3d orbital and S 3p orbitals. Optical properties of samples were detected using conversion from Cu 3d/S 3p levels into conduction band; this could be attributed to changes in the band gap.

4. Conclusion

In summary, CMTS films were grown on a substrate of soda-lime glass by a spin coating method and annealed at 550 °C for 90 minutes in the furnace depending on the sulphur flux. The effect of sulphur flux on the structural, morphological, and optical properties of the film was investigated. It was observed that the CMTS(I) thin-film had (112) oriented main peaks with good crystallinity and low strain value. The XRD parameters including crystal size, dislocation density, and microstrain values were changed with increasing the H₂S: Ar flow. The smallest value $3.54 \times 10^{14} \text{ m}^{-2}$ for the CMTS(I) thin film was annealed at 550 °C, corresponding to the maximum value of crystal size. The crystallinity of the CMTS thin film was considerably improved at 30 sccm H₂S: Ar flow. SEM images revealed that the larger particles could be fragmented into smaller-sized particles. AFM images revealed that CMTS thin films were relatively smooth in the valley region while many crystals-like structures were seen in the hill region. It was observed that the films absorbed a higher amount of photons as the sulphur flux increased and there is a decrease in the infrared region. E_g values of the films were calculated as 1.22 and 1.15 eV for CMTS(I) and CMTS(II), respectively. It is said that the H₂S: Ar flow was effective on the energy band gap and the crystalline quality in obtained films. As a result, CMTS(I) with optimal properties was determined to be used as an absorber layer in a solar cell and the variation in the absorption value of the films indicated that CMTS(I) flux could be also applied in various optical applications including optical windows and UV filter production. In this study, we experimentally showed that the cationic

substitution of Zn by Mn could change the physical properties including absorbance and energy band gap of CZTS material.

Acknowledgments

We thank Dicle University Science and Technology Application and Research Center (DUBTAM) for their support of our study.

Ethical Statements

The author declares that this study does not require ethics committee approval or any special permission and does not cause any harm to the environment.

Conflict of interest

The authors declare no conflict of interest.

Authors Contributions

CAA ve SB carried out the experiments and wrote the manuscript. The authors discussed the results and contributed to the final article.

References

- [1] A. Rockett, R. Birkmire, CuInSe₂ for photovoltaic applications, *Journal of Applied Physics* 70(7) R81-R97, 1991.
- [2] C.-Y. Su, W.-H. Ho, H.-C. Lin, C.-Y. Nieh, S.-C. Liang, The effects of the morphology on the CIGS thin films prepared by CuInGa single precursor, *Solar energy materials and solar cells* 95(1) 261-263, 2011.
- [3] J. Britt, C. Ferekides, Thin-film CdS/CdTe solar cell with 15.8% efficiency, *Applied physics letters* 62(22), 2851-2852, 1993.
- [4] S. Kahraman, S. Çetinkaya, M. Podlogar, S. Bernik, H. Çetinkara, H. Güder, Effects of the sulphurization temperature on sol gel-processed Cu₂ZnSnS₄ thin films, *Ceramics International* 39(8), 9285-9292, 2013.
- [5] X. Wu, High-efficiency polycrystalline CdTe thin-film solar cells, *Solar Energy* 77(6) 803-814, 2004.
- [6] J. K. Larsen, F. Larsson, T. Törndahl, N. Saini, L. Riekehr, Y. Ren, C. Platzer- Björkman, Cadmium free Cu₂ZnSnS₄ solar cells with 9.7% efficiency, *Advanced Energy Materials* 9(21), 1900439, 2019.
- [7] J.-S. Seol, S.-Y. Lee, J.-C. Lee, H.-D. Nam, K.-H. Kim, Electrical and optical properties of Cu₂ZnSnS₄ thin films prepared by rf magnetron sputtering process, *Solar energy materials and solar cells* 75(1-2), 155-162, 2003.
- [8] H. Guan, X. Wang, Y. Huang, Optical, photocatalytic and thermoelectric properties of Cu₂MeSnS₄ (Me= Mn 2, Fe 2, Co 2) nanocrystals via microwave-assisted solvothermal method, *Chalcogenide Letters* 15(9), 435-440, 2018.
- [9] H. Guan, H. Hou, M. Li, J. Cui, Photocatalytic and thermoelectric properties of Cu₂MnSnS₄ nanoparticles synthesized via solvothermal method, *Materials Letters* 188, 319-322, 2017.
- [10] X. Li, Z. Hou, S. Gao, Y. Zeng, J. Ao, Z. Zhou, Y. Zhang, B. Da, W. Liu, Y. Sun, Y. Zhang, Efficient optimization of the performance of Mn²⁺-doped kesterite solar cell: Machine learning aided synthesis of high efficient Cu₂(Mn, Zn)Sn(S, Se)₄ Solar Cells, *Solar RRL* 2(12), 1800198, 2018.

- [11] J. Yu, H. Deng, Q. Zhang, J. Tao, L. Sun, P. Yang, J. Chu, The role of sulfurization temperature on the morphological, structural and optical properties of electroplated $\text{Cu}_2\text{MnSnS}_4$ absorbers for photovoltaics, *Materials Letters* 233, 111-114, 2018.
- [12] K. Rudisch, W.F. Espinosa- García, J.M. Osorio- Guillén, C.M. Araujo, C. Platzer- Björkman, J.J. Scragg, Structural and electronic properties of $\text{Cu}_2\text{MnSnS}_4$ from experiment and First-Principles calculations, *Physica status solidi (b)* 256(7), 1800743, 2019.
- [13] X. Liang, P. Guo, G. Wang, R. Deng, D. Pan, X. Wei, Dilute magnetic semiconductor $\text{Cu}_2\text{MnSnS}_4$ nanocrystals with a novel zincblende and wurtzite structure, *RSC Advances* 2(12), 5044-5046, 2012.
- [14] Y. Cui, R. Deng, G. Wang, D. Pan, A general strategy for synthesis of quaternary semiconductor Cu_2MSnS_4 (M= Co^{2+} , Fe^{2+} , Ni^{2+} , Mn^{2+}) nanocrystals, *Journal of Materials Chemistry* 22(43), 23136-23140, 2012
- [15] M. Quintero, E. Moreno, S. Alvarez, J. Marquina, C. Rincón, E. Quintero, P. Grima, J.-A. Heano, M.A. Macías, Lattice parameter values and phase transitions for the $\text{Cu}_2\text{-II-IV-S}_4$ (Se_4)(II= Mn, Fe, Co; IV= Si, Ge, Sn) magnetic semiconductor compounds, *Rev. LatinAm. Metal. Mater.* 34(1), 2014.
- [16] T.K. Todorov, K.B. Reuter, D.B. Mitzi, High-efficiency solar cell with earth-abundant liquid-processed absorber, *Advanced Materials* 22(20), 156-159, 2010.
- [17] Y. Zou, X. Su, J. Jiang, Phase-controlled synthesis of $\text{Cu}_2\text{ZnSnS}_4$ nanocrystals: the role of reactivity between Zn and S, *Journal of the American Chemical Society* 135(49), 18377-18384, 2013.
- [18] P.K. Sarswat, M. Snure, M.L. Free, A. Tiwari, CZTS thin films on transparent conducting electrodes by electrochemical technique, *Thin Solid Films* 520(6), 1694-1697, 2012.
- [19] K. Tanaka, N. Moritake, H. Uchiki, Preparation of $\text{Cu}_2\text{ZnSnS}_4$ thin films by sulphurizing sol-gel deposited precursors, *Solar energy materials and solar cells* 91(13), 1199-1201, 2007.
- [20] S. Vanalakar, G. Agawane, S. Shin, M. Suryawanshi, K. Gurav, K. Jeon, P. Patil, C. Jeong, J. Kim, J. Kim, A review on pulsed laser deposited CZTS thin films for solar cell applications, *Journal of Alloys and Compounds* 619, 109-121, 2015.
- [21] Y. Lu, S. Wang, Z. Li, Z. Jiang, M. Yang, Q. Li, Effects of sputtering period on the performance of $\text{Cu}_2\text{ZnSnS}_4$ solar cells, *Physica B: Condensed Matter* 507, 35-40, 2017.
- [22] A. Tombak, Y.S. Ocak, M.F. Genişel, T. Kilicoglu, Electrical and optical properties of $\text{Cu}_2\text{ZnSnS}_4$ grown by a thermal co-evaporation method and its diode application, *Materials Science in Semiconductor Processing* 28, 98-102, 2014.
- [23] M.Z. Ansari, N. Khare, Structural and optical properties of CZTS thin films deposited by ultrasonically assisted chemical vapour deposition, *Journal of Physics D: Applied Physics* 47(18), 185101, 2014.
- [24] B. Liu, J. Guo, R. Hao, L. Wang, K. Gu, S. Sun, A. Aierken, Effect of Na doping on the performance and the band alignment of CZTS/CdS thin film solar cell, *Solar Energy* 201, 219-226, 2020.

- [25] K. Maeda, K. Tanaka, Y. Nakano, H. Uchiki, Annealing temperature dependence of properties of $\text{Cu}_2\text{ZnSnS}_4$ thin films prepared by sol-gel sulfurization method. *Japanese Journal of Applied Physics* 50(5S2), 05FB08, 2011.
- [26] E. Waluś, M. Manecki, G. Cios, T. Tokarski, Effect of a sulfur precursor on the hydrothermal synthesis of $\text{Cu}_2\text{MnSnS}_4$, *Materials* 14(13), 3457, 2021.
- [27] G. Yang, X. Zhai, Y. Li, B. Yao, Z. Ding, R. Deng, H. Zhao, L. Zhang, Z. Zhang, Synthesis and characterizations of $\text{Cu}_2\text{MgSnS}_4$ thin films with different sulphuration temperatures, *Materials Letters* 242, 58-61, 2019.
- [28] J. Shaikh, R.C. Pawar, R.S. Devan, Y.-R. Ma, P.P. Salvi, S.S. Kolekar, P.S. Patil, Synthesis and characterization of Ru doped CuO thin films for supercapacitor based on Bronsted acidic ionic liquid, *Electrochimica Acta* 56(5), 2127-2134, 2011.
- [29] V.T. Tiong, Y. Zhang, J. Bell, H. Wang, Phase-selective hydrothermal synthesis of $\text{Cu}_2\text{ZnSnS}_4$ nanocrystals: the effect of the sulphur precursor, *CrystEngComm* 16(20), 4306-4313, 2014.
- [30] M. Saleem, L. Fang, A. Wakeel, M. Rashad, C. Kong, Simple preparation and characterization of nano-crystalline zinc oxide thin films by sol-gel method on glass substrate, 2012.
- [31] J.J. Scragg, T. Ericson, X. Fontané, V. Izquierdo-Roca, A. Pérez-Rodríguez, T. Kubart, M. Edoff, C. Platzer-Björkman, Rapid annealing of reactively sputtered precursors for $\text{Cu}_2\text{ZnSnS}_4$ solar cells, *Progress in Photovoltaics: Research and Applications* 22(1), 10-17, 2014.
- [32] L. Chen, H. Deng, J. Tao, W. Zhou, L. Sun, F. Yue, P. Yang, J. Chu, Influence of annealing temperature on structural and optical properties of $\text{Cu}_2\text{MnSnS}_4$ thin films fabricated by sol-gel technique, *Journal of Alloys and Compounds* 640, 23-28, 2015.
- [33] J. Jiang, L. Zhang, W. Wang, R. Hong, The role of sulphur in the sulphurization of CZTS layer prepared by DC magnetron sputtering from a single quaternary ceramic target, *Ceramics International* 44(10), 11597-11602, 2018.
- [34] W. Wang, G. Wang, G. Chen, S. Chen, Z. Huang, The effect of sulphur vapor pressure on $\text{Cu}_2\text{ZnSnS}_4$ thin film growth for solar cells, *Solar Energy* 148 12-16, 2017.
- [35] M. Olgar, A. Seyhan, A. Sarp, R. Zan, Impact of sulphurization parameters on properties of CZTS thin films grown using quaternary target, *Journal of Materials Science: Materials in Electronics* 31(22), 20620-20631, 2020.
- [36] S. Manjunatha, R.H. Krishna, T. Thomas, B. Panigrahi, M. Dharmaprakash, Moss-Burstein effect in stable, cubic ZrO_2 : Eu^{+3} nanophosphors derived from rapid microwave-assisted solution-combustion technique, *Materials Research Bulletin* 98, 139-147, 2018.
- [37] J. Tauc, *Amorphous and liquid semiconductors*, Springer Science & Business Media, 2012.
- [38] J. Yu, H. Deng, Q. Zhang, J. Tao, L. Sun, P. Yang, J. Chu, The role of sulphurization temperature on the morphological, structural and optical properties of electroplated $\text{Cu}_2\text{MnSnS}_4$ absorbers for photovoltaics, *Materials Letters* 233, 111-114, 2018.
- [39] J. Paier, R. Asahi, A. Nagoya, G. Kresse, $\text{Cu}_2\text{ZnSnS}_4$ as a potential photovoltaic material: a hybrid Hartree-Fock density functional theory study, *Physical Review B* 79(11), 115126, 2009.

**EXPRESSION PATTERN OF BK CHANNELS UNDER VARIOUS OXIDATIVE STRESS CONDITIONS IN SKELETAL MUSCLES****Cagil COSKUN^{1*}**  **Figen A. CICEK¹**  **Onur TOKGÜN²**  **Isil OCAL¹** ¹Cukurova University Faculty of Medicine, Department of Biophysics Adana TURKEY²Pamukkale University Faculty of Medicine, Department of Medical Genetics, Denizli TURKEY

*Corresponding Author: ccoskun@cu.edu.tr

Abstract: BK (large conductance Ca^{2+} -activated potassium) channels are expressed in myocytes, but changes in their molecular levels in the presence of oxidative stress are not clear yet. Determination of the molecular effects of various oxidative stress conditions may reveal the possible mechanism and potential therapeutic effects. In the present study, isolated rat soleus muscle where *KCNMA1* genes encoding BK channel protein expressed widely in skeletal muscle, were exposed to cyclopiazonic acid (CPA) and hydrogen peroxide (H_2O_2) as oxidative stress inducers. A streptozotocin-induced diabetes mellitus model was also used to demonstrate the effects of an endogenous source of oxidative stress. Moreover, NS1619, a BK channel opener, was used to determine whether activation of the channel re-regulated the channel expression. After the incubation periods, *KCNMA1* gene expression levels in each group were determined by real-time PCR experiments. While CPA and H_2O_2 decreased *KCNMA1* expression significantly, the expression did not change under the systemic diabetes mellitus condition. However, the transcriptional level significantly decreased in diabetes in the presence of H_2O_2 . On the other hand, *KCNMA1* expression was re-regulated back to the control level by the addition of NS1619 in only H_2O_2 groups. The results demonstrated for the first time that acute oxidative stress, rather than systemic conditions, affects the *KCNMA1* gene expression level in skeletal muscles. The study also showed the effects of NS1619 on the regulation of the transcriptional levels of BK channel protein under hydrogen peroxide conditions.

Keywords: Skeletal muscle, BK channels, Oxidative Stress, *KCNMA1*, NS1619

Received: March 14, 2022

Accepted: June 1, 2022

1. Introduction

Large conductance Ca^{2+} activated K^+ (BK) channels, one of the diverse groups of potassium channels, have crucial roles in the regulation of membrane potentials. The channels are expressed in many cells, including muscles and nerves, and they are responsible for many physiological and pathophysiological processes due to their unique negative feedback mechanism in determining intracellular calcium concentration [1, 2]. Given their important role in vasodilation/vasoconstriction, functional changes in the channels in smooth muscles may result in arterial hypertension or hypoxia [3]. BK channels also control cardiac pacing and heart rhythm [4, 5]. Moreover, the channels located at presynaptic regions in the central nervous system (CNS) regulate neurotransmitter release and neuronal firing by modulating K^+ influx and the intracellular Ca^{2+} concentration [6, 7]. Therefore, an imbalance or dysregulation in the function of the channel may lead to important CNS diseases, such as epilepsy and cerebral ischemia [6]. The BK channels are also expressed in skeletal muscles, besides smooth and cardiac muscles. Dysregulations in normal BK channel activity are often associated with hyper/hypokalemic periodic paralysis [8]. In addition, the alpha subunit of the BK channels which is the

functional unit including the pore-forming structure is encoded by *KCNMA1* gene and is located on chromosome 10 (10q22.3) in humans [2]. Alterations in *KCNMA1* gene expression have also been linked to some diseases including temporal lobe epilepsy [9] and breast cancer [10]. Moreover, more than 10 *KCNMA1* mutations that change the normal activity of the BK channel, have been identified [2]. Considering the striking relations between BK channels and such diseases, targeting the regulation of these channels through gene therapy and activating/blocking the channels are important treatment approaches that should be developed in the future [8, 11, 12].

Reactive oxygen species (ROS) are maintained at relatively low levels in healthy tissues, and they participate in many physiological processes, such as apoptosis and protein phosphorylation. However, their production is balanced with antioxidant defense systems otherwise, excessive amounts of ROS can result in cellular damage, which is called “oxidative stress”. Moreover, there are many oxidative stress-related diseases, such as cancer, and cardiovascular or neurodegenerative diseases [13, 14]. ROS are generated in not only metabolic conditions but also in contraction activities in skeletal muscles [15]. However, an abnormal increase in the ROS level commonly leads to muscle fatigue associated with intense exercise. In an extreme situation, it can lead to muscle degeneration and muscle loss if oxidative stress increases further and is not prevented by antioxidant mechanisms [15, 16]. On the other hand, the modulatory effect of ROS on BK channels has been shown in many different cells and tissues [17]. Hydrogen peroxide (H_2O_2), which is a non-radical ROS, changes the opening probability and activities of the channels in HEK cells or the coronary artery [18, 19]. However, the effect of ROS on BK channels in skeletal muscles is not clear, even though it is well known that there is a significant expression of the channels in these muscles. It has been shown that BK channels are more expressed in slow-twitch rat fibers than in fast-twitch fibers [8, 12].

Oxidative stress can be induced endogenously or exogenously. One of the main associated diseases related to oxidative stress is diabetes. Excessive ROS production is linked to hyperglycemia and vice versa [20, 21]. While some chemicals are introduced exogenously, such diseases can be an endogenous source of oxidative stress. Therefore, the present study aimed to determine the effects of various endogenous and exogenous oxidative stress conditions on the *KCNMA1* gene in rat soleus muscles having slow-twitch fibers. On the other hand, NS1619, a BK channel activator, reverses the effects of oxidative stress on the channel in various conditions, while its effect at the gene level is unclear. Therefore, the present study also aimed to determine the effect of NS1619 on the channel gene expression.

2. Material and Methods

2.1. Animals

All experimental procedures involving animals in the study were approved by Cukurova University Local Ethics Committee on Animal Experiments (Decision Date: 24.08.2017; Decision Number: 7). In the present study, thirty-two adult male Wistar albino rats, weighing approximately 250-300 g, were kept in stable laboratory conditions with a 12h:12h photoperiod and 22 ± 1 °C room temperature during all animal experimental procedures. They were given free access to standard food pellets and water. Rats were equally and randomly divided into groups of controls and diabetes, before incubation processes.

2.2. Induction of diabetes by streptozotocin (STZ) injection

In the present study, animals in the diabetes groups were injected with 45 mg/kg STZ (Sigma S0130) as described earlier [22]. Rats in the control groups were injected with equivalent physiological saline. Blood glucose levels should be >250 mg/dL to define diabetes mellitus (DM) which is correlated

with hyperglycemia [23]. Hyperglycemic conditions in the diabetes groups were confirmed by measuring the blood glucose levels 3 days after the injection. The hyperglycemic indexes of the animals were checked every week for 4 weeks.

2.3. Exogenous incubations

After the rats were euthanized with an overdose of isoflurane, both soleus muscles of each rat were immediately dissected by sterile surgical techniques. Afterwards, the tissues were placed in an organ bath containing Krebs solution (112 mM NaCl, 5 mM KCl, 25 mM NaHCO₃, 1 mM NaH₂PO₄, 0.5 mM MgCl₂, 2.5 mM CaCl₂, and 11.5 mM glucose; pH 7.4) and were aerated with 95% O₂ and 5% CO₂ at 37°C. Chemicals used in the present study were added to the bath solution by an appropriate micropipette following a stabilization period for the tissues of about an hour. During the experiments, the tissues were incubated with 1 mM H₂O₂, 30 μM NS1619, or 20 μM cyclopiazonic acid (CPA), which produces oxidative stress [24].

After the end of the incubation period, the tissues were taken from the tissue bath, freeze shocked in liquid nitrogen, and stored at -80 °C.

2.4. mRNA expressions

In the present study, RNA isolation of the soleus tissues was performed by using a Nucleozol reagent (Macherey Nagel-MN). For this purpose, tissues were homogenized first with the help of a glass homogenizator containing 1 mL of the Nucleozol solution. RNA was isolated by following the steps of the kit instructor's manual, and cDNA samples were synthesized by using high-capacity cDNA reverse transcription kit (Applied Biosystems) in a total of 20 μL.

Expression levels of the *KCNMA1* gene in each group were determined by real-time PCR experiments. After the preparation of a 20 μL reaction mix containing 1 μL of cDNA sample, 10 μL of GoTaq qPCR master mix (Promega), 0,5 uL of each primer and 8 μL of RNase-free water, a conditional temperature program was performed (95 °C for 2 min for a cycle, 95 °C for 15s, and 60 °C for 60 s for 40 cycles) for the reaction mix in a Biorad CFX96 thermal cycler.

Expression levels in each group were determined by a relative quantification method known as the 2^{-ΔΔCt} method [25]. GAPDH was used as a housekeeping gene in the study.

KCNMA1 and GAPDH gene amplification primers used in the study are shown in Table 1.

Table 1. Primers used in the study

Primer Name	Genbank Accession Code	Primer sequences (5'→3')
KCNMA1-Forward	NM_031828.2	AAGGGCTGTCAACATCAACC
KCNMA1-Reverse		CTGTCCATTCCAGGAGGTGT
GAPDH-Forward	NM_017008.4	AAGATGGTGAAGGTCGGTGT
GAPDH-Reverse		TGACTGTGCCGTTGAACTTG

2.5. Statistics

In the study, one-way ANOVA (performed in GraphPad Prism 5.0) was used to indicate statistical significance between groups (p <0.05). Data analysis results have been presented as mean ± SEM.

3. Results

3.1. The effects of muscle incubations with H₂O₂ and H₂O₂ + NS1619 on the KCNMA1 expression level

Incubation of the soleus muscles with H₂O₂ (1 mM) for 60 minutes led to a statistically significant reduction in the BK channel expression at the transcriptional level (Fig 1). Hydrogen peroxide decreased the *KCNMA1* expression by 70% (0.296 ± 0.06). In order to determine the effects of NS1619 on oxidative stress via BK channels, muscles were incubated with H₂O₂ (1 mM) and NS1619 (30 μ M) (H₂O₂ + NS1619) in a tissue bath for an hour. The gene expression levels also decreased (0.747 ± 0.14) but the difference was not statistically significant when compared to that in the control group. More importantly, gene expression levels for H₂O₂ and H₂O₂ + NS1619 were significantly different.

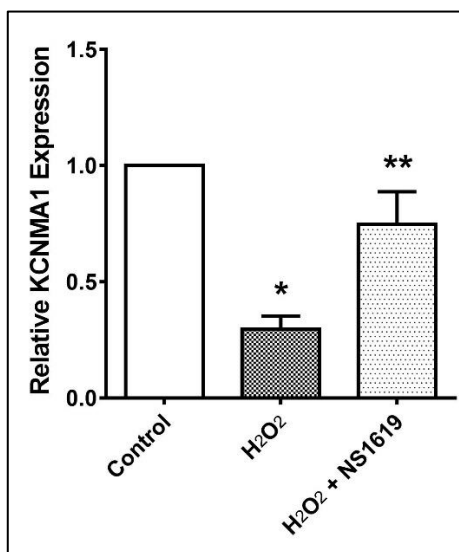


Figure 1. Effect of H₂O₂ and NS1619 on KCNMA1 expression. The soleus muscles were incubated with H₂O₂ (1 mM), and H₂O₂ (1 mM) + NS1619 (30 μ M). Each group's data were normalized to control data. Bars indicate mean \pm SEM, n = 6-8 (each measurement performed in duplicated). * demonstrate the difference between control and H₂O₂ ($p < 0.05$), and ** demonstrate the difference between H₂O₂ and H₂O₂ + NS1619 ($p < 0.05$).

3.2. The effects of CPA on the KCNMA1 gene expression level

Muscles were incubated for 1 hour with CPA, a SERCA (Sarco/Endoplasmic Reticulum CaATPase) inhibitor. The *KCNMA1* transcriptional level decreased with the presence of CPA (0.275 ± 0.07) (Fig 2). The difference was statistically significant when compared to that in the control group. In addition, the *KCNMA1* gene expression level was significantly different in the CPA + NS1619 group when compared to that in the control group, as the gene expression level was 0.473 ± 0.07 in the CPA + NS1619 group. In the meantime, there were no meaningful differences in terms of the BK channel transcriptional level between the CPA and CPA + NS1619 groups.

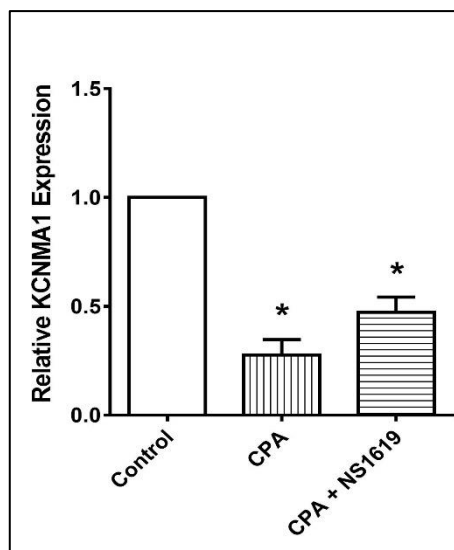


Figure 2. Effect of CPA and NS1619 on *KCNMA1* expression. The soleus muscles were incubated with CPA (20 μ M), and CPA (20 μ M) + NS1619 (30 μ M). Each group's data were normalized to control data. Bars indicate mean \pm SEM, n = 6-8 (each measurement performed duplicated). * demonstrate the difference between the control group and the other groups ($p < 0.05$).

3.3. *KCNMA1* gene expression level under diabetic conditions.

In the study, at first, the *KCNMA1* gene expression level in the soleus muscles in the STZ-induced diabetes groups was compared to that in the control group (Fig 3). Although the gene expression decreased under diabetic conditions (DM group: 0.848 ± 0.18), the difference was not statistically significant when compared to that in the control group. Then, the soleus muscles in the DM group were divided into the DM + H₂O₂ and DM + H₂O₂ + NS1619 groups, and each group was incubated with the stated chemicals for an hour. The gene expression in the DM + H₂O₂ group significantly decreased when compared to that in the control group (0.311 ± 0.04). Moreover, *KCNMA1* gene expression did not change significantly in the DM + H₂O₂ + NS1619 group when compared to that in the control group (1.009 ± 0.11). However, the difference between the DM + H₂O₂ and DM + H₂O₂ + NS1619 groups was statistically significant.

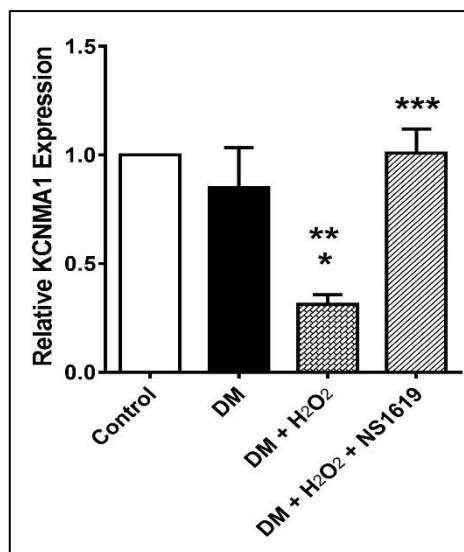


Figure 3. Relative *KCNMA1* expression under diabetic conditions. Each group's data were normalized to control data. DM soleus muscles were also incubated with H₂O₂ (1 mM), or H₂O₂ (1 mM) + NS1619 (30 μM). Bars indicate mean ± SEM, n = 6-8 (each measurement performed duplicated). * demonstrate the difference between the control and DM + H₂O₂ groups (p < 0.05), ** demonstrate the difference between the DM and DM + H₂O₂ groups (p < 0.05), and *** demonstrate the difference between the DM + H₂O₂ and DM + H₂O₂ + NS1619 groups (p < 0.05). DM: diabetes mellitus.

4. Discussion

The present study demonstrated the transcriptional effects of various oxidative stress conditions on BK channels in skeletal muscles in terms of the changes in the *KCNMA1* gene that encodes the channel protein. In addition, the effect of channel activation on this stress was also examined through changes in the *KCNMA1* expression level.

Oxidative stress was induced by 3 methods in this study. Hydrogen peroxide is widely used as an oxidative stress agent in many studies [26]. Its production is increased during normal skeletal muscle exercise [27]. Moreover, H₂O₂ affects the release of Ca²⁺ from sarcoplasmic reticulum vesicles via ryanodine binding in skeletal muscles dose-dependently [28]. Therefore, we used H₂O₂, which has such a direct effect on the functionality of skeletal muscles, to generate oxidative stress in this study. In addition, previous studies have also shown the effects of H₂O₂ on BK channels. Byckhlow et al. showed that 1 mM H₂O₂ changed the channel activity in human endothelial cells [29]. Another study showed that hydrogen peroxide affected the membrane potentials via BK channels [30].

The present study demonstrated that incubation with H₂O₂ significantly decreased the *KCNMA1* gene expression level in skeletal muscles. To the best of our knowledge, the data are the first to show the effects of oxidative stress on BK channels at the transcriptional level. However, there were no meaningful expression changes in the presence of both H₂O₂ and a BK channel opener, NS1619. The results strongly indicated that NS1619 abolished the transcriptional effects of H₂O₂ on BK channels in skeletal muscles. Previous studies have demonstrated that NS1619 protects cells from H₂O₂-induced cytotoxicity, including neurons, epithelial cells, and astrocytes [31-33]. However, the present study demonstrated the reverse effects of a BK channel opener on H₂O₂-induced transcriptional dysregulation of *KCNMA1*.

Another factor that causes oxidative stress is the increase in Ca^{2+} concentration [34, 35]. Furthermore, CPA triggers a robust Ca^{2+} increase by blocking Ca^{2+} -ATPase [36], and such blocking induces oxidative stress [24]. Therefore, in the present study, CPA was used as another oxidative stress agent, which significantly inhibited the *KCNMA1* gene expression. Although the presence of NS1619 hindered the decrease in the gene expression level, the expression level did not return to the control level in the CPA+NS1619 group. BK channels are regulated in various signal pathways in different cells [37-39]. Considering the fact that NS1619 incubation did not make any difference to the transcriptional levels of *KCNMA1* in the presence of CPA, unlike in the case of H_2O_2 , it could be claimed that NS1619 may show its transcriptional effects on BK channels via the mechanisms where H_2O_2 is active.

Previous studies have shown cells in systemic pathologies, such as diabetes mellitus, are exposed to oxidative stress at varying levels compared with healthy cells. In addition, many stress pathways are also activated in diabetes [40, 41]. Therefore, *KCNMA1* gene expression in the soleus muscles of diabetic rats was investigated, since diabetes was considered an oxidative stress inducer in the present study. Although the gene expression level decreased in the DM group, the change was not statistically significant. It is argued that various signaling pathways for a cell adapt to different stress conditions caused by DM or excessive ROS production [42]. Moreover, the findings of the present study may correlate with previous findings that the function of the BK channels may have been impaired, although the protein expression did not change [43]. In addition, a significant decrease in *KCNMA1* gene expression in diabetes with hydrogen peroxide may demonstrate that the transcriptional changes of the BK channel may result from the acute effect of hydrogen peroxide application. On the contrary, the metabolic system may have adapted the gene expression levels through feedback mechanisms in long-term diabetes conditions. In the present study, NS1619 reversed the gene expression level back to that in the control group in dual oxidative stress conditions (H_2O_2 plus diabetes). The results may again demonstrate that BK channel activation shows its regulatory effect via H_2O_2 active pathways. In previous studies, it was stated that NS1619 exerts its protective effect against cytotoxic agents through other pathways that are independent of the activation of the channel [44].

In conclusion, the present study showed that *KCNMA1* gene expression levels differed under various oxidative stress conditions. Moreover, the change in the expression could be dependent on the acute effects of oxidative stress. NS1619 re-regulated the channel expression back to levels seen in the control's under only hydrogen peroxide conditions. The results may suggest that this activator could be a useful potential therapeutic agent against diseases resulting from hydrogen-peroxide-induced oxidative stress. However, the topic requires further molecular research, since hydrogen peroxide could also have harmful effects as a DNA damager and apoptosis inducer for cells in addition to oxidative stress [45, 46]. Therefore, more experiments should be carried out in which the other effects of H_2O_2 are taken into account and evaluated.

Conflict of interest: The authors declare that there are no conflicts of interest

Compliance with Research and Publication Ethics: This study was carried out by obeying research and ethics rules.

Ethical statement: This study was approved by Cukurova University Local Ethics Committee on Animal Experiments. (Decision Date: 24.08.2017; Decision Number: 7)

Authors' Contributions:

C.C: Conceptualization, Methodology, Formal analysis, Data Curation, Investigation, Resources, Writing - Original draft preparation

F.A.C.: Conceptualization, Methodology, Formal analysis, Data Curation, Investigation, Writing - Original draft preparation

O.T.: Methodology, Resources, Formal analysis, Data Curation, Investigation, Writing - Original draft preparation,

I.O.: Methodology, Writing - Original draft preparation

All authors read and approved the final manuscript.

References

- [1] Cui, J., Yang, H., Lee, U.S., "Molecular mechanisms of BK channel activation", *Cell Mol Life Sci*, 66(5), 852-75, 2009.
- [2] Bailey, C.S., Moldenhauer, H.J., Park, S.M., Keros, S., Meredith, A.L., "KCNMA1-linked channelopathy", *J Gen Physiol*, 151(10), 1173-1189, 2019.
- [3] Carvalho-de-Souza, J.L., Varanda, W.A., Tostes, R.C., Chignalia, A.Z., "BK Channels in Cardiovascular Diseases and Aging", *Aging Dis*, 4(1), 38-49, 2013.
- [4] Imlach, W.L., Finch, S.C., Miller, J.H., Meredith, A.L., Dalziel, J.E., "A role for BK channels in heart rate regulation in rodents", *PLoS One*, 5(1), e8698, 2010.
- [5] Lai, M.H., Wu, Y., Gao, Z., Anderson, M.E., Dalziel, J.E., Meredith, A.L., "BK channels regulate sinoatrial node firing rate and cardiac pacing in vivo", *Am J Physiol Heart Circ Physiol*, 307(9), H1327-38, 2014.
- [6] Contet, C., Goulding, S.P., Kuljis, D.A., Barth, A.L., "BK Channels in the Central Nervous System", *Int Rev Neurobiol*, 128, 281-342, 2016.
- [7] Wang, Z.W., "Regulation of synaptic transmission by presynaptic CaMKII and BK channels", *Mol Neurobiol*, 38(2), 153-66, 2008.
- [8] Maqoud, F., Cetrone, M., Mele, A., Tricarico, D., "Molecular structure and function of big calcium-activated potassium channels in skeletal muscle: pharmacological perspectives", *Physiol Genomics*, 49(6), 306-317, 2017.
- [9] Ermolinsky, B., Arshadmansab, M.F., Pacheco Otalora, L.F., Zarei, M.M., Garrido-Sanabria, E.R., "Deficit of Kcnma1 mRNA expression in the dentate gyrus of epileptic rats", *Neuroreport*, 19(13), 1291-4, 2008.
- [10] Khaitan, D., et al., "Role of KCNMA1 gene in breast cancer invasion and metastasis to the brain", *BMC Cancer*, 9, 258, 2009.
- [11] Layne, J.J., Nausch, B., Olesen, S.P., Nelson, M.T., "BK channel activation by NS11021 decreases excitability and contractility of urinary bladder smooth muscle", *Am J Physiol Regul Integr Comp Physiol*, 298(2), R378-84, 2010.
- [12] Dinardo, M.M., Camerino, G., Mele, A., Latorre, R., Conte Camerino, D., Tricarico, D., "Splicing of the rSlo gene affects the molecular composition and drug response of Ca²⁺-activated K⁺ channels in skeletal muscle", *PLoS One*, 7(7), e40235, 2012.
- [13] Pizzino, G., et al., "Oxidative Stress: Harms and Benefits for Human Health", *Oxid Med Cell Longev*, 2017, 8416763, 2017.
- [14] Poprac, P., Jomova, K., Simunkova, M., Kollar, V., Rhodes, C.J., Valko, M., "Targeting Free Radicals in Oxidative Stress-Related Human Diseases", *Trends Pharmacol Sci*, 38(7), 592-607, 2017.

- [15] Jackson, M.J., Pollock, N., Staunton, C., Stretton, C., Vasilaki, A., McArdle, A., Oxidative stress in skeletal muscle: Unraveling the potential beneficial and deleterious roles of reactive oxygen species, in: *Oxidative Stress: Eustress and Distress* (Ed. H. Sies), Academic Press, London, 713-733, 2020.
- [16] Wan, J.-j., Qin, Z., Wang, P.-y., Sun, Y., Liu, X., "Muscle fatigue: general understanding and treatment", *Experimental & Molecular Medicine*, 49(10), e384-e384, 2017.
- [17] Hermann, A., Sitdikova, G.F., Weiger, T.M., "Oxidative Stress and Maxi Calcium-Activated Potassium (BK) Channels", *Biomolecules*, 5(3), 1870-911, 2015.
- [18] DiChiara, T.J., Reinhart, P.H., "Redox modulation of hsl α Ca²⁺-activated K⁺ channels", *J Neurosci*, 17(13), 4942-55, 1997.
- [19] Barlow, R.S., El-Mowafy, A.M., White, R.E., "H₂O₂ opens BK(Ca) channels via the PLA₂-arachidonic acid signaling cascade in coronary artery smooth muscle", *Am J Physiol Heart Circ Physiol*, 279(2), H475-83, 2000.
- [20] Ighodaro, O.M., "Molecular pathways associated with oxidative stress in diabetes mellitus", *Biomed Pharmacother*, 108, 656-662, 2018.
- [21] Qian, L.L., Liu, X.Y., Yu, Z.M., Wang, R.X., "BK Channel Dysfunction in Diabetic Coronary Artery: Role of the E3 Ubiquitin Ligases", *Front Physiol*, 11, 453, 2020.
- [22] Mert, T., Gunay, I., Ocal, I., "Neurobiological effects of pulsed magnetic field on diabetes-induced neuropathy", *Bioelectromagnetics*, 31(1), 39-47, 2010.
- [23] Craner, M.J., Klein, J.P., Renganathan, M., Black, J.A., Waxman, S.G., "Changes of sodium channel expression in experimental painful diabetic neuropathy", *Ann Neurol*, 52(6), 786-92, 2002.
- [24] Bonyadi, F., Hasanzadeh, S., Malekinejad, H., "Cyclopiazonic acid induced p53-dependent apoptosis in the testis of mice: Another male related risk factor of infertility", *Environ Toxicol*, 36(5), 903-913, 2021.
- [25] Livak, K.J., Schmittgen, T.D., "Analysis of relative gene expression data using real-time quantitative PCR and the 2^{-ΔΔC_T} Method", *Methods*, 25(4), 402-8, 2001.
- [26] Ransy, C., Vaz, C., Lombès, A., Bouillaud, F., "Use of H₂O₂ to Cause Oxidative Stress, the Catalase Issue", *International journal of molecular sciences*, 21(23), 9149, 2020.
- [27] Vasilaki, A., et al., "Free radical generation by skeletal muscle of adult and old mice: effect of contractile activity", *Aging Cell*, 5(2), 109-17, 2006.
- [28] Favero, T.G., Zable, A.C., Abramson, J.J., "Hydrogen peroxide stimulates the Ca²⁺ release channel from skeletal muscle sarcoplasmic reticulum", *J Biol Chem*, 270(43), 25557-63, 1995.
- [29] Bychkov, R., et al., "Hydrogen peroxide, potassium currents, and membrane potential in human endothelial cells", *Circulation*, 99(13), 1719-25, 1999.
- [30] Coskun, C., Buyuknacar, H.S., Cicek, F., Gunay, I., "BK channel openers NS1619 and NS11021 reverse hydrogen peroxide-induced membrane potential changes in skeletal muscle", *Journal of Receptors and Signal Transduction*, 40(5), 449-455, 2020.
- [31] Kang, J.H., Woo, J.S., "The Ca²⁺-activated K⁺ (BK) Channel-opener NS 1619 Prevents Hydrogen peroxide-induced Cell Death and Mitochondrial Dysfunction in Retinal Pigment Epithelial Cells", *Journal of Life Science*, 27(11), 1349-1356, 2017.

- [32] Gáspár, T., Katakam, P., Snipes, J.A., Kis, B., Domoki, F., Bari, F., Busija, D.W., "Delayed neuronal preconditioning by NS1619 is independent of calcium-activated potassium channels", *J Neurochem*, 105(4), 1115-28, 2008.
- [33] Coskun, C., Tokgun, O., "BK channel opener protects cell viability by regulating reactive oxygen levels in astrocyte cells", *General physiology and biophysics*, 40(5), 409-417, 2021.
- [34] Görlach, A., Bertram, K., Hudecova, S., Krizanova, O., "Calcium and ROS: A mutual interplay", *Redox Biol*, 6, 260-271, 2015.
- [35] Przygodzki, T., Sokal, A., Bryszewska, M., "Calcium ionophore A23187 action on cardiac myocytes is accompanied by enhanced production of reactive oxygen species", *Biochim Biophys Acta*, 1740(3), 481-8, 2005.
- [36] Mème, W., Huchet-Cadiou, C., Léoty, C., "Cyclopiazonic acid-induced changes in the contraction and Ca²⁺ transient of frog fast-twitch skeletal muscle", *Am J Physiol*, 274(1), C253-61, 1998.
- [37] Oeggerli, M., Tian, Y., Ruiz, C., Wijker, B., Sauter, G., Obermann, E., Güth, U., Zlobec, I., Sausbier, M., Kunzelmann, K., Bubendorf, L., "Role of KCNMA1 in Breast Cancer", *PLOS ONE*, 7(8), e41664, 2012.
- [38] O'Malley, D., Harvey, J., "Insulin activates native and recombinant large-conductance Ca(2+)-activated potassium channels via a mitogen-activated protein kinase-dependent process", *Mol Pharmacol*, 65(6), 1352-63, 2004.
- [39] Olsen, M.L., Weaver, A.K., Ritch, P.S., Sontheimer, H., "Modulation of glioma BK channels via erbB2", *J Neurosci Res*, 81(2), 179-89, 2005.
- [40] Good, A.L., Stoffers, D.A., "Stress-Induced Translational Regulation Mediated by RNA Binding Proteins: Key Links to β -Cell Failure in Diabetes", *Diabetes*, 69(4), 499-507, 2020.
- [41] Cicek, F.A., Toy, A., Tuncay, E., Can, B., Turan, B., "Beta-blocker timolol alleviates hyperglycemia-induced cardiac damage via inhibition of endoplasmic reticulum stress", *J Bioenerg Biomembr*, 46(5), 377-87, 2014.
- [42] Wellen, K.E., Thompson, C.B., "Cellular Metabolic Stress: Considering How Cells Respond to Nutrient Excess", *Molecular Cell*, 40(2), 323-332, 2010.
- [43] Nieves-Cintrón, M., et al., "Impaired BK(Ca) channel function in native vascular smooth muscle from humans with type 2 diabetes", *Sci Rep*, 7(1), 14058, 2017.
- [44] Gáspár, T., et al., "Immediate neuronal preconditioning by NS1619", *Brain Research*, 1285, 196-207, 2009.
- [45] Xiang, J., Wan, C., Guo, R., Guo, D., "Is Hydrogen Peroxide a Suitable Apoptosis Inducer for All Cell Types?", *Biomed Res Int*, 2016, 7343965, 2016.
- [46] Krohn, K., Maier, J., Paschke, R., "Mechanisms of disease: hydrogen peroxide, DNA damage, and mutagenesis in the development of thyroid tumors", *Nat Clin Pract Endocrinol Metab*, 3(10), 713-20, 2007.



INVESTIGATION OF GLOBOZOOSPERMIA'S MORPHOLOGICAL STRUCTURE AND DNA FRAGMENTATION IN OLIGOZOOSPERMIA CASES IN INFERTILE MALES

Zuhal ÇANKIRI¹  **Murat AKKUŞ¹**  **Eda YILDIZHAN¹**  **Dilara AKINCI¹** 
Firat AŞIR¹  **Onur DEDE²**  **Muhamet AFŞİN³** 

¹Department of Histology and Embryology, Faculty of Medicine, Dicle University, Diyarbakır, Turkey

²Department of Urology, Faculty of Medicine, Dicle University, Diyarbakır, Turkey

³Department of Biology, Faculty of Science, Dicle University, Diyarbakır, Turkey

Corresponding Author: zbcankiri@gmail.com

Abstract: Total globozoospermia is diagnosed by the presence of 100% round-headed spermatozoa without acrosomes. It is still unclear whether patients whose ejaculate contains both normal and globozoospermic cells (partial globozoospermia) suffer from a variation of the same syndrome. Affected men may experience decreased fertility and even infertility. In some cases, an increased number of cells with DNA fragmentation has also been observed in patients with globozoospermia. In this study, standard semen analysis methods in accordance with WHO criteria were applied to infertile male patient groups consisting of 20 normozoospermic and 20 oligozoospermic individuals who were admitted to our clinic. Age and sperm parameters (volume, vitality, concentration, total motility, and morphology) were determined and statistically analyzed in normozoospermic and oligozoospermic infertile men. Sperms were stained with the Eosin-Nigrosin method and were visualized under an immersion lens light microscope and evaluated for vitality. The slides were stained using sperm staining solutions with the Spermac technique and the sperms were evaluated morphologically. Sperm DNA fragmentation damage was evaluated by the acridine orange staining method. Our results revealed that sperm morphological features (Kruger test) and sperm DNA fragmentation, obtained with various staining techniques, are important in the clinical approach to male infertility and ART methods, and should be used together.

Keywords: Infertility, Oligozoospermia, Roundhead, Globozoospermia, DNA fragmentation

Received: December 23, 2021

Accepted: May 10, 2022

1. Introduction

World Health Organization (WHO) defines infertility as the inability to achieve pregnancy despite unprotected and regular sexual intercourse for 12 months or longer [1]. Despite the chance of conceiving in a healthy couple is 85-90% in twelve months and 75% in six months, this rate decreases to 20-25% in one month [2-6]. In women over 35 years of age, the inability to achieve pregnancy despite regular sexual intercourse for 6 months without protection is an indication to start the process of diagnosis and treatment [2, 6, 7]. The promising results of Assisted Reproductive Therapy (ART) and the increase in the number of couples using these methods have caused an increase in treatment applications and paved the way for developments in this field [8]. Evaluation of the female factor is an important criterion in diagnosis and treatment in infertile couples who admit for treatment [9]. It has been observed that the advanced age of the patient causes a decrease in the oocyte reserve and the quality and the number of

embryos, the frequency of aneuploidy, implantation rates, and an increase in the fragmentation rate in the embryo [10, 11].

1.1. Diagnostic Tests in Male Infertility

While semen analysis is at the beginning of the application to help the evaluation and diagnosis of men in terms of infertility, it is very important to evaluate non-sperm cells and determine the steps for diagnosis and treatment with functional tests.

Semen Analysis: During semen analysis; fresh semen obtained after at least 48 hours of sexual avoidance is evaluated. The number, motility, and morphological structure of sperm are determined by these analyzes [12].

- **Macroscopic Examination:** The priority in semen analysis is to start inspection with the unaided eye. In order to minimize the effect of environmental conditions on semen quality; analysis should be performed within the first 30-60 minutes after ejaculation [13]. During these examinations, color, liquefaction, viscosity, volume, and pH are evaluated.
- **Microscopic Examination:** For the examination of liquefied fresh semen preparations, the use of phase-contrast microscopy is recommended. During these examinations, concentration, vitality, motility, and morphology are evaluated [14,15].

Sperm DNA Damage (Sperm DNA Fragmentation = SDF)

Although there is not enough information about the causes and mechanisms of sperm DNA damage today, three fundamental mechanisms are mentioned. These are; anomalies in sperm chromatin packaging, apoptosis, and oxidative stress [16].

Total globozoospermia is diagnosed by the presence of 100% round-headed spermatozoa without acrosomes. In some cases, an increased number of cells with DNA fragmentation has also been observed. This study aims to determine the semen parameters, globozoospermia, and DNA fragmentation rates in normozoospermic and oligozoospermic cases and to investigate their relationship with male infertility.

2. Materials and Methods

Working Groups: Normozoospermic and oligozoospermic semen samples were obtained from patients aged 21-44 years who applied to Diyarbakır Dicle University Hospital Urology polyclinic. All patients were informed about patient data confidentiality and data sharing, and a written consent form was obtained from all the patients.

Semen Supply and Analysis: Semen samples were taken from patients who came to the urology outpatient clinic and abstained from sexual abstinence for 2-7 days. Parameters were evaluated such as duration of sexual abstinence, volume, color, viscosity, and liquefaction time.

Vitality Assessment by Eosin-Nigrosin Administration: One drop (1µl) of semen was mixed with two drops (2µl) of Eosin-Y in an experiment tube. After 30 seconds, 3 drops of Nigrosin were added and mixed gently. Thus, dead cells were stained red, and living cells were not.

Preparation of Sperm with Swim-Up Technique: The prepared tube was incubated at 37°C, at an angle of 45°, for 30-60 minutes. The supernatant was aspirated and discarded.

Evaluation of Sperm Concentration and Motility: It was evaluated according to WHO classification: Fast-forward motile sperm (+4), Slow-forward motile sperm (+3), In situ-motile sperm (+2), Immotile sperm (+1) [14].

Sperm Staining and Morphology Evaluation: The preparations were stained with the spermac method.

Evaluation of Sperm DNA Fragmentation: Sperm samples fixed with Carnoy fixative for one hour were stained with AO dye for 5 minutes in the dark and examined under a fluorescence microscope.

Statistical Analysis

The normality control of the data was tested with the Kolmogorov Smirnov Test. The student's T-test was used for statistical analysis. The level of significance was accepted as a $p=0.05$ limit.

3. Results

Forty voluntary infertile male individuals were included in this prospective study. Semen analyzes were performed on a total of 40 patients, 20 of them were normozoospermic patients and the rest of them were oligozoospermic study group patients, who met the study criteria. Sperm samples were evaluated morphologically and DNA fragmentation indexes were investigated.

3.1. Vitality in Normozoospermic and Oligozoospermic Cases

Sperms stained with the Eosin-Nigrosin method were evaluated for vitality. Live and dead sperms were visualized under the x100 immersion objective light microscope (Figure 1).

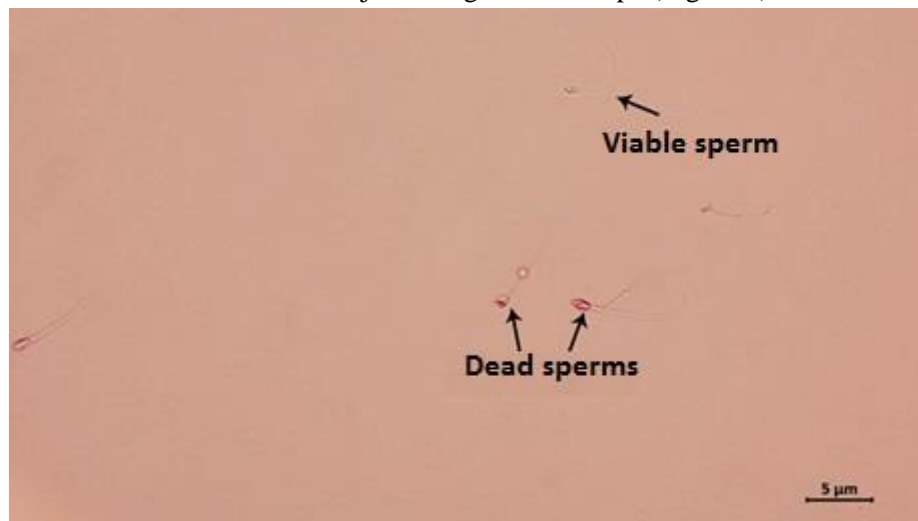


Figure 1. Live and dead sperms

3.2. Morphology in Normozoospermic and Oligozoospermic Cases

Sperms stained with the spermac method were evaluated morphologically. Normal (Figure 2) and abnormal morphological sperms were visualized under an x100 immersion objective light microscope (Figure 3).

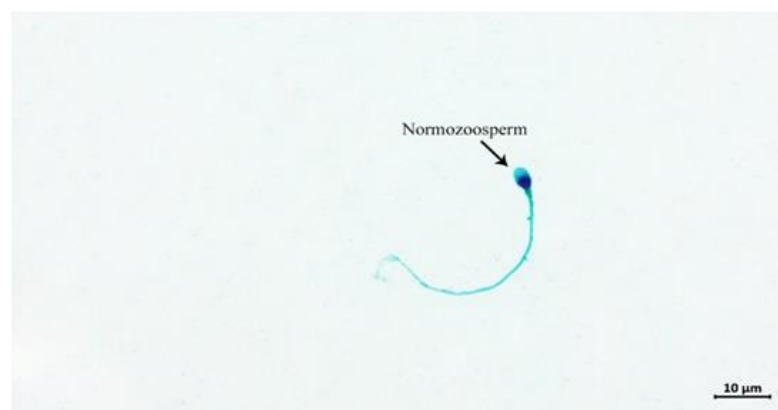


Figure 2. Normal morphological sperm

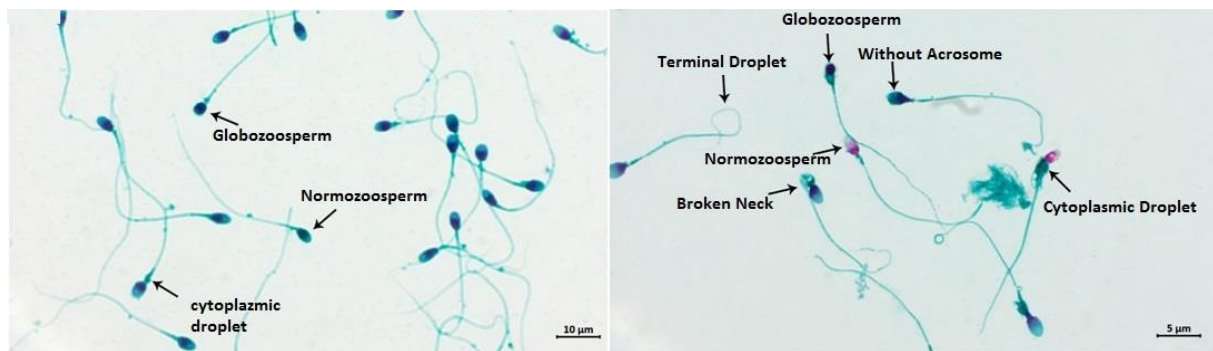


Figure 3. Abnormal morphological sperms

3.3. DNA Fragmentation in Normozoospermic and Oligozoospermic Cases

Sperm stained with acridine orange method were evaluated for DNA fragmentation. By looking at one hundred sperm, the percentages of damaged and healthy sperm were calculated. It was visualized by fluorescence microscopy with an x100 immersion objective (Figure 4).

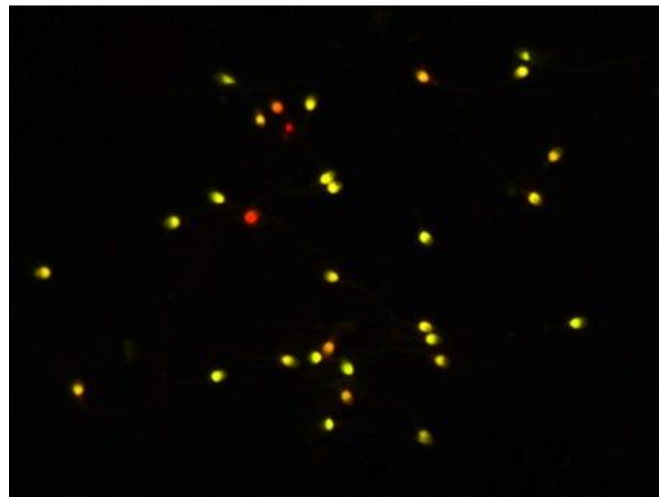


Figure 4. Sperm stained with acridine orange method

3.4. Statistical Findings

The statistical analysis results of the mean values of age, sperm parameters, globozoospermia incidence, and DNA fragmentation in normozoospermic and oligozoospermic infertile men are presented in Table 1.

The mean ages of normozoospermic and oligozoospermic infertile men were found to be 28.80 ± 5.473 years and 29.05 ± 3.348 years, respectively, and there was no statistically significant difference between the groups ($p = 0.86$) (Table 1).

While the sperm volume was $1,700 \pm .9921$ ml in normozoospermic infertile men, it was found as $1,700 \pm .8176$ ml in oligozoospermic men, and no significant difference was found ($p = 1.00$) (Table 1). The mean sperm concentration of normozoospermic and oligozoospermic infertile men was $83,945 \pm 45.4547$ 10⁶/ml and $10,910 \pm 3.6092$ 10⁶/ml, respectively, with a statistically significant difference ($p = 0.000$) (Table 1).

Total motility was found to be significantly higher in normozoospermic men (62.80 ± 19.691) compared to oligozoospermic individuals ($44.35\% \pm 6.368$) ($p = 0.001$). Sperm morphology rates (Kruger) were found to be significantly higher in normozoospermic males ($11.40 \pm 6.870\%$) than in

oligozoospermics ($5.15 \pm 4.246\%$) ($p=0.001$). The mean vitality percentages of normozoospermic and oligozoospermic infertile men were found to be $71.80 \pm 13.387\%$ and $65.30 \pm 15.941\%$, respectively, and no significant difference was detected ($p = 0.17$).

In addition, the mean rate of globozoospermia in normozoospermic and oligozoospermic male groups was $2.3500 \pm 2.27746\%$ and $19.7778 \pm 20.09597\%$, respectively, and it was determined that there was a significant difference between the groups ($p = 0.001$) (Table 1). Sperm DNA fragmentation rates were $16.55 \pm 6.304\%$ and $22.75\% \pm 10.627\%$ in normozoospermic and oligozoospermic male groups, respectively, and were significantly higher in oligozoospermic males compared to normozoospermic males ($p = 0.03$). (Table 1).

Table 1. Statistical analysis results of age, sperm parameters, the incidence of globozoospermia and mean values of DNA fragmentation in normozoospermic and oligozoospermic infertile men.

	Groups	n	mean	Standard deviation	Student's T
Age	N	20	28,80	5,473	t=-0,174
	O	20	29,05	3,348	p=0,86, NS
Volume (ml)	N	20	1,700	,9921	t=00
	O	20	1,700	,8176	p=1,00, NS
sperm concentration (Million/ ml)	N	20	83,945	45,4547	t=7,163
	O	20	10,910	3,6092	p=0,000, S
Total motility (%)	N	20	62,80	19,691	t=3,987
	O	20	44,35	6,368	p=0,001, S
Morphology (Kruger) (%)	N	20	11,40	6,870	t=3,461
	O	20	5,15	4,246	p=0,002, S
Vitality (%)	N	20	71,80	13,387	t=1,317
	O	20	65,30	15,941	p=0,17, NS
Globozoospermia rate (%)	N	20	2,3500	2,27746	t=-3,854
	O	20	19,7778	20,09597	P=0,001, S
DNA fragmentation index (%)	N	20	16,55	6,304	t=-2,244
	O	20	22,75	10,627	p=0,03, S

t: Student T-test; p: Mann Whitney p değeri; NS: nonsignificant, S: significant; n: number of subjects; N: normozoospermic group; O: oligozoospermic group.

4. Discussion

Globozoospermia is a rare but serious condition that can cause male infertility and is characterized by sperm morphology disorder. Globozoospermia was first defined as 'Rundkopfspermatozoen', which means round-headed spermatozoa in German, in the light of light microscopic analyzes performed by Myhöfer in 1965 [17]. In the case reports published in the following years, the morphological and etiological aspects of globozoospermia were emphasized [18]. Despite all this time, the genes responsible for globozoospermia or the patterns of heredity remain unclear [19].

It has been reported that there are many differences between normozoospermic and oligozoospermic infertile men in terms of various semen parameters such as volume, motility, and vitality [20]. In these studies, it was reported that semen volume was different between the groups, but this difference was not statistically significant. In our study, we found that sperm volume differed between the groups, but this difference was not statistically significant.

Schirren et al. reported the first case of globozoospermia after examination of 2200 patients undergoing routine andrological screening, indicating an incidence of less than 0.05%. Later, the same study group reported the incidence of globozoospermia in andrological patients by correcting it to 0.1% [21]. In subsequent studies, the incidence of this irregularity among infertile men has been suggested to be between <0.05% and 0.1% in different studies [22, 23]. However, Holstein et al. reported patients with only 20-60% round-headed spermatozoa in their ejaculate [24]. In our study, 100% of globozoospermia cases were not found in both normozoospermic and oligozoospermic infertile cases. Globozoospermia was observed at a rate ranging from 1% to 7% in 7 cases out of 20 normozoospermic cases and between 4% and 96% in all 20 oligozoospermic cases. The results of our study are in agreement with the information reported by Siddique et al in the literature that “morphological anomalies are generally more common in oligozoospermia when compared to normozoospermia” [25]. Male infertility can be caused by low sperm count, low sperm quality, or both [25]. Similar to the studies in the literature, our results revealed that sperm motility and concentration decrease and the rate of globozoospermia increases in infertile men [26].

In our study; sperm samples of the patients were examined based on Kruger criteria and evaluated morphologically. However, it is known that this conventional semen analysis does not reflect the fertility status of a man alone [22, 27]. Sperm with normal morphology and motility may have approximately 8% abnormal chromatin/ DNA [22]. It has been reported that infertile men with normal sperm parameters may also have high levels of DNA damage [28]. In addition to these conventional routine analyzes, information on the fragmentation rates of DNA is obtained by using the AO method in semen samples obtained from oligozoospermic and normozoospermic infertile groups. In our study, DNA fragmentation was investigated using the AO method in normozoospermic and oligozoospermic infertile male groups, and DNA fragmentation was significantly higher in the oligozoospermic group, in line with the literature.

Fragmentation rates of DNA are important for appropriate sperm selection in ART, because the use of sperm with abnormal DNA during the IVF program leads to a significant decrease in the success rate [22, 27]. As seen in our study results, globozoospermia is probably associated with DNA damage, like other sperm morphological abnormalities.

5. Conclusion

Based on the results we obtained, in addition to conventional approaches, sperm should be stained with various staining methods such as spermac staining to examine their morphological features and analyze sperm DNA fragmentation. As a result of these analyzes, the relationship between the incidence of globozoospermia and DNA fragmentation can be demonstrated. But it is necessary to study in larger series in order to clearly demonstrate this relationship.

Ethical statement

This work was approved by Dicle University Research Ethics Committee. Approval number and date: 2020/74; 06.02.2020

Financial support

This study was financially supported by Dicle University Scientific Research Projects Commission Headquarters (DUBAP, Project No: TIP.20.028).

Conflict of interest

The authors declare that they have no conflicts of interest.

Authors' Contributions

Z.Ç: Writing - Original draft preparation

M.A: Methodology

E.Y: Formal analysis, Writing

D.A: Conceptualization, Methodology

F.A: Investigation

O.D: Resources

M.AF: Investigation

All authors read and approved the final manuscript.

References

- [1] Zegers Hochschild F. et al. "International Committee for Monitoring Assisted Reproductive Technology (ICMART) and the World Health Organization (WHO) revised glossary of ART terminology, 2009", *Fertil Steril.*, 92(5), 1520-4, 2009.
- [2] Beck WW, Uçar A (Çev.Ed.), Kadın Hastalıkları ve Doğum, Nobel Tıp Kitapevleri, İstanbul, 1998, p. 359-368
- [3] Yao MWM ve Schust JD. Berek JS (Çev.Ed.), İnfertilite. Novak Jinekoloji, Nobel Tıp Kitapevleri Ltd. Şti., İstanbul, 2004, p. 973-1045
- [4] Bankowski JB ve Vlahos N. İnfertilite ve üremeye yardımcı teknolojiler, John Hopkins Jinekoloji ve Obstetrik El Kitabı, Atlas Kitapçılık Tic. Ltd. Şti., Ankara, 2005, p.376-383
- [5] Rowe PJ, Comhaire FH, Hargreave TB ve Mahmoud AMA. Orhon E (Çev.Ed.), İnfertil Erkeklerin Standart Araştırma Tanı ve Tedavileri İçin Dünya Sağlık Örgütü El Kitabı, Cambridge University Press,Londra, 2000
- [6] Çivi S. Nedim Çiçek (Çev.Ed.), İnfertilite Epidemiyolojisi, Palme Yayıncılık, Ankara, 2007, p. 1-10
- [7] Wright KP, Johnson JV, Gibbs RS, Karlan BY, Haney AF (Çev.Ed.), İnfertilite, Güneş Tıp Kitapevleri, Ankara, 2010, p. 705-715
- [8] Speroff L, Glass NH, Kase RG. Clinical Gynecologic Endocrinology and Infertility. 7 nd edition, Lippincott Williams & Wilkins, Baltimore, 2007
- [9] Smith S, Pfeifer SM, Collins JA., "Diagnosis and management of female infertility", *JAMA*, 290(13), 1767-1770, 2003.
- [10] Hull MG, Fleming CF, Hughes AO, McDermott A., "The age-related decline in female fecundity: a quantitative controlled study of implanting capacity and survival of individual embryos after in vitro fertilization", *Fertil Steril*, 65(4), 783-90, 1996.
- [11] Ziebe S, et al., "Embryo quality and developmental potential is compromised by age", *Acta Obstet Gynecol Scand*, 80(2), 169-174 2001.
- [12] Nagvenkar P, Desai K, Hinduja I, Zaveri K., "Chromosomal studies in infertile men with oligozoospermia & non-obstructive azoospermia", *Indian J MedRes*, 122 (1), 34-42, 2005.
- [13] Kadioğlu A, Kendirci M, Aktan G, Yaman Ö, Çayan S. WHO Laboratuar El Kitabı. İnsan Semeninin İncelenmesi ve İşlemlerden Geçirilmesi. Türk Üroloji Derneği. 2011, ISBN:978-975-00112-4-5.

- [14] World Health Organization. WHO Laboratory Manual for the Examination and Processing of Human Semen, 5th edition. Geneva, World Health Organization, 2010.
- [15] Eliasson R Analysis of Semen in Behrman SJ and Kistner RW (Çev. Ed.) Progress in Infertility, 2nd Edition. Little, Brown, Boston 1975: 691-714
- [16] Agarwal A, Allamaneni SS., “Sperm DNA damage assessment: a test whose time has come”, *Fertil Steril*, 84(4), 850-3, 2005.
- [17] Satar DA. ve Narin R., “Globozoospermi”, *Cukurova Medical Journal*, 39(1), 1-6, 2014.
- [18] Wolff H, Schill W, MoritzP., “Round-headed spermatozoa:A rare andrologic finding (globe-headed spermatozoa,globozoospermia)”, *Der Hautarzt; Zeitschrift Fur Dermatologie, Venerologie, Und Verwandte Gebiete*, 27(3), 111–116, 1976.
- [19] Dam AH, Feenstra I, Westphal JR, Ramos L, van Golde RJ, Kremer JAM. “Globozoospermi are visited”, *Hum Reprod Update*, 13, 63-75, 2007.
- [20] Menteşeoğlu P, Tangal S, Yiğman M, Haliloğlu AH, Pabuçcu EG, Çağlar GS, “The Correlation Between Semen Parameters and Galectin-3 Levels of Infertile Men”, *Turkish Journal of Reproductive Medicine and Surgery*, 5(1), 1-5, 2021.
- [21] Schirren CG, Holstein AF, Schirren C., “Über die Morphogenese der kopfigen Spermatozoen des Menschen”, *Andrologia*, 3, 117–25, 1971.
- [22] Fesahat F, Henkel R, Agarwal A., “Globozoospermia syndrome: An update”, *Andrologia*, 52(2), e13459, 2020.
- [23] Kalahanis J, Rousso D, Kourtis A, Mavromatidis G, Makedos G, Panidis D, “Round-headed spermatozoa in semen specimens from fertile and subfertile men”, *The Journal of Reproductive Medicine*, 47(6), 489–493, 2002.
- [24] Holstein AF, Schirren CG, Schirren C and Mauss J, “Round headed spermatozoa: a cause of male infertility”, *Dtsch Med Wochenschr*, 98, 61–62, 1973.
- [25] Siddique RA, et al., “Sperm abnormalities and DNA fragmentation visavis mammalian male infertility – a review. “, *Wayamba Journal of Animal Science*, 3, 174-189, 2011.
- [26] Eskandari N, Tavalae M, Zohrabi D, Nasr-Esfahani MH, “Association between total globozoospermia and sperm chromatin defects”, *Andrologia*, 50(2), e12843, 2018.
- [27] Cho CL, Agarwal A, “Role of sperm DNA fragmentation in male factor infertility: A systematic review”, *Arab Journal of Urology*, 16(1), 21–34, 2018.
- [28] Agarwal A, Bragais FM, Sabanegh E., “Assessing sperm function”, *Urologic Clinics of North America*, 35(2), 157–171, 2008

**MODELLING OF THE SOLAR CELL BASED ON Cu_2SnS_3 THIN FILM PRODUCED BY SPRAY PYROLYSIS****Serap YIGIT GEZGIN¹** **İlhan CANDAN²** **Silan BATURAY²** **Hamdi Sukur KILIC^{1,3,4,*}** ¹ Department of Physics, Faculty of Science, University of Selçuk, 42031 Selçuklu, Konya, Turkey² Department of Physics, Faculty of Science, Dicle University, Diyarbakir, Turkey³ Directorate of High Technology Research and Application Center, University of Selçuk, 42031 Selçuklu, Konya, Turkey⁴ Directorate of Laser-Induced Proton Therapy Application and Research Center, University of Selçuk, 42031 Selçuklu, Konya, Turkey

*Corresponding author e-mail: hamdisukurkilic@selcuk.edu.tr

Abstract: Cu_2SnS_3 (CTS) thin film has been produced for 30 sccm sulphur flux rate at 30 minutes annealing durations at 550 °C temperature. CTS thin film's crystalline structure has been investigated and crystalline size, lattice parameters, dislocation density and microstrain, crystalline number have also been determined. The CTS thin film's morphological and optical properties have been examined and thoroughly interpreted. Mo/CTS/CdS/AZO/Al solar cell has been modeled based on CTS thin film produced at the present work, using SCAPS-1D simulation program. V_{oc} , J_{sc} , FF, conversion efficiency, and photovoltaic parameters have been determined depending on neutral defect density at the interface, coefficient of radiative recombination, Auger electron/hole capture's coefficient, and operation temperature of CTS solar cell. As a consequence of the simulation study, the ideal efficiency of CTS solar cell has been determined to be 3.72 % and all the data obtained in this study have been presented, interpreted, and concluded to be original results.

Keywords: CTS, solar cell, SCAPS-1D, simulation

Received: April 18, 2022

Accepted: June 16, 2022

1. Introduction

The photovoltaic (PV) market is based on solar cells manufactured with Silicon (Si), Copper Indium Gallium Selenum (CIGS), and Cadmium Tellur (CdTe) materials. Some prominent disadvantages of these mentioned elements are the high cost of In, Ga, and Te and the high processing cost of Si as well as the toxicity of the Cd element. Some materials such as $\text{Cu}_2\text{ZnSnS}_4$ (CZTS) have attracted great attention, which has properties such as low cost, easy to process, and being environmentally friendly. However, in recent years, since CZTS consists of many elements and its second phases are easily formed, research studies have been carried out on Cu_2SnS_3 (CTS) material for use in PV field. CTS is a p-type semiconductor with band gap values ranging from 0.9 to 1.7 eV and a high absorption coefficient ($>10^4 \text{ cm}^{-1}$) [1]. Due to different arrangements of atoms in a lattice structure of CTS, different phases such as $\text{Cu}_4\text{Sn}_7\text{S}_{16}$, Cu_4SnS_4 , Cu_3SnS_4 structure can also occur [2]. These phases can be considered a candidate for use as an absorber layer in solar cells.

The theoretically calculated efficiency of CTS solar cells is determined at about 30%. The reported highest power conversion efficiencies of CTS solar cell belongs to 6% Ge-doped CTS [3] and 5.24% Na-doped CTS [4] solar cells. Defects, voids, and second phases in CTS thin film cause some

limitations on efficiency. In order to overcome this problem, some parameters of technical and experimental apparatuses used in the thin film production are of great importance. Many techniques are described to achieve Cu_2SnS_3 thin films, for instance, reactive radio frequency magnetron sputtering [5], co-evaporation [6], wet chemical process [7], and spray pyrolysis [8]. Nonetheless, merely a limited number of studies have been reported on sprayed Cu_2SnS_3 materials [9]. In comparison to other methods, the Spin coating technique has numerous benefits including low production cost, easy deposition over large-area, and relatively simpler composition adjustment. Therefore, it is particularly more suitable for thin-film fabrication [10].

In recent years, simulation software used to calculate the efficiency of solar cells with the usage of layers forming solar cells has great importance. One of the most commonly used software in this field is SCAPS-1D (one-dimensional simulation software) only which among others calculates PV parameters of solar cell using physical parameters such as energy band gap, dielectric permittivity, the electron affinity of layers constructing solar cell, thin film thickness, the work function of contacts, etc [11, 12]. SCAPS-1D was developed at Gent University in the Department of Electronics and Information Systems. Depending on parameters such as operation temperature, Auger electron/hole capture coefficient, and interfacial defect density [13], PV parameters of solar cells can be calculated, and thus, a reliable prediction can be made on the performance of the solar cell.

In this study, CTS thin films have been grown for 30 sccm sulphur flux rate at 30 minutes annealing durations at 550 °C temperature. The structural, optical, and crystalline properties of thin film have been determined and interpreted. It is important to determine how the experimentally produced thin film will affect the efficiency by modelling it in the solar cell structure using the characteristic parameters of thin film. At this point, Mo/CTS/CdS/AZO/Al structure has been formed with the most ideal CTS thin film determined by using SCAPS-1D simulation program to show the effect of this thin film on the efficiency of CTS thin film solar cell. PV parameters of CTS solar cells have been calculated and their curves have been plotted, depending on temperature, Auger electron/hole capture coefficient, and interfacial defect density. It has been determined that PV performance of CTS solar cells depends on defects, recombination mechanism, and operation temperature. Thus, based on these parameters which significantly affect the efficiency, it has reached the conclusion that it is possible to obtain consistent interpretations of behaviour of solar cells. As a result, since CTS is a new material in solar cell applications, such a study on CTS solar cells with SCAPS program is very rare in literature, and it can be predicted that this study shed light on the experimental efficiency improvement studies of solar cells.

2. Materials and Methods

2.1. Experimental

CTS thin films have been fabricated on a glass substrate using a solution comprising 0.389 g copper(II) acetate ($\text{Cu}(\text{CH}_3\text{COO})_2 \cdot \text{H}_2\text{O}$), 0.220 g tin(II) chloride dehydrate ($\text{SnCl}_2 \cdot 2\text{H}_2\text{O}$), and 0.444 g thiourea ($\text{CH}_4\text{N}_2\text{S}$) deposited under optimized conditions with different Sulphur flux rate and time. All chemicals are separately dissolved in a mixture of ethanol and glacial acetic acid for 6h at room temperature in magnetic stirring. Firstly, thiourea solution was slowly mixed into copper(II) acetate solution, then, tin(II) chloride dehydrate was poured into the thiourea/copper(II) acetate solution. Finally, obtained solutions were stirred at room temperature for 4h until a homogenous clear solution was obtained. To regulate pH values, a few drops of diethanolamine were added to the mixture solution for the final solution. The molar ratios of Cu/Sn/S elements in solutions were adjusted due to a ratio of 2/1/6. Thiourea has volatile nature at high temperatures [14]. Therefore, this component was added twice to avoid any possible loss of sulphur.

Before the deposition process, glass substrates were washed by boiling in sufficient quantities of a mixture of H₂O, NH₃, and H₂O₂ at 105 °C, and then, in sufficient quantities of a mixture of H₂O, H₂O₂, and HCl at 105 °C to eliminate any residual waste. Then, glass substrates were cleaned in deionized water for 3 min and later dried. After obtaining final solutions and cleaning of substrates, the obtained solution was deposited via spin coating at a rate of 1500 rpm for 63 s in air. Final solutions were deposited onto the glass substrate layer by layer, and each layer was preheated to 220 °C for 10 min. After this process, obtained films were annealed under 30 and 40 sccm (standard cubic centimeters per minute) in 10 % H₂S + 90 % Ar atmosphere at 550 °C temperature in the furnace. CTS thin films were annealed under 30 sccm 10 % H₂S + 90 % Ar atmosphere at 550 °C temperatures for 15, 30 and 60 min and 40 sccm 10 % H₂S + 90 % Ar atmosphere at 550 °C temperatures for 15, 30 and 60 min, respectively. The obtained sample has been labelled and is demonstrated in Table 1 with Sulphur flux rate and time.

Table 1. Fabrication parameters for CTS film.

Thin films	Sulphur annealing temperature and time	Sulphur flux rate
CTS	550 °C for 30 min	30 sccm H ₂ S: Ar

The effect of Sulfurization on the structural, morphological, optical, and photoluminescence properties of CTS thin film have been studied in this work. The crystalline properties of acquired CTS film have been studied by X-Ray Diffractometer (XRD) unit (Bruker D8 Advance) operated at 40 kV and 40 mA. XRD was set up with a range of θ -2 θ in steps of 0.02° to analyse the structural and phase purity analysis of CTS thin film structure. In addition, obtained films were investigated by using Confocal Raman Microscope and the obtained results were analysed. The surface topology and EDX measurements of all obtained films were obtained by FEI Quanta 250 FEG Scanning Electron Microscopy (FEI Co., Eindhoven, Netherlands). Conclusions of transmittance, energy band gap, and Urbach energy of thin films were analysed by Shimadzu UV-3600 spectrophotometer (Shimadzu, Tokyo, Japan) between 300-1100 nm.

2.2. Numerical Modelling and Material Parameters

SCAPS-1D software calculates PV parameters (V_{oc} , I_{sc} , FF, and η) of solar cells using physical parameters such as dielectric permittivity, band gap, the electron affinity of semiconductor layers in solar cells, work function of contacts, etc [15]. This software, which is a package program, performs a calculation procedure based on the solution of the Poisson equation (Eq. (1)), hole and electron continuity equations (Eq. (2) and Eq. (3)) [16], respectively:

$$\frac{\partial}{\partial x} (\epsilon_0 \epsilon_r \frac{\partial \Psi}{\partial x}) = -q \left(p - n + N_D^+ - N_A^- + \frac{\rho_{def}}{q} \right) \quad (1)$$

$$-\frac{\partial J_p}{\partial x} - U_p + G = \frac{\partial p}{\partial x} \quad (2)$$

$$-\frac{\partial J_n}{\partial x} - U_n + G = \frac{\partial n}{\partial x} \quad (3)$$

where ϵ_r and ϵ_0 are permittivity of semiconductor and vacuum, respectively, Ψ is electrostatic potential, N_A^- and N_D^+ indicate densities of ionized impurities of acceptors and donors, n and p are carrier concentrations of electrons and holes, and ρ_{def} is charge density of defects, J_p and J_n indicate hole and electron current densities, respectively, and G is generation rate.

Calculation of PV parameters of optical devices such as p-n heterojunction solar cells, perovskite solar cells, and dye solar cells can be performed courtesy of SCAP-1D software.

3. Results and Discussion

3.1. XRD and Raman Analyses

CTS thin film has been formed in tetragonal Cu_2SnS_3 crystal structures as seen XRD pattern and Raman spectrum in Figures 1a and 1b. (112), (200), (220) and (312) crystalline orientates in CTS thin film have been formed on $2\theta = 28.8^\circ, 33.3^\circ, 47.6^\circ, 56.4^\circ$ angles, respectively. The crystal sizes of CTS films have been calculated by the Scherer equation:

$$S = 0.94\lambda/\beta\cos\theta \quad (4)$$

where S, λ, β , and θ parameters are the size of crystalline, X-Ray wavelength, full-width at half-maximum (FWHM) of diffraction peak, and angle of Bragg diffraction, respectively. The main crystalline size of CTS was calculated to be 55.56 nm.

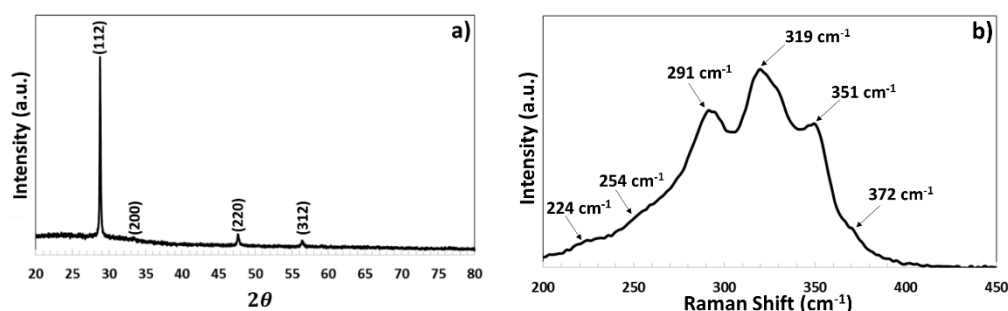


Figure 1. XRD pattern and Raman spectrum of CTS thin film

The micro-strain and dislocation density of CTS thin film [17, 18] were obtained by Eq. (5) and Eq. (6) as following:

$$\varepsilon = \frac{\beta\cos\theta}{4} \quad (5)$$

$$\delta = \frac{1}{D^2} \quad (6)$$

The microstrain (ε) and dislocation density (δ), which express the formation of trap, vacancy, dangling bond, and defects in CTS thin film that negatively affect the development of the crystal structure. ε and δ values have been determined to be 0.65×10^{-3} and 3.24×10^{16} lines/m², respectively (as given in Table 2). The large crystal size leads to that there are few defects and traps in the grain boundary of thin film which ensures that ε and δ are low. Thus, minority charge carriers in CTS thin film have a longer lifetime and this leads to the higher efficiency of solar cells produced based on the absorber layer.

The crystal number per unit surface area (N) is calculated by Eq. (7),

$$N = \frac{T}{D^3} \quad (7)$$

where T is the thickness of CTS thin film. N value expresses the crystallization amount, which varies depending on the thickness and crystal size. The average thickness of CTS thin film has been measured to be $\sim 1 \mu\text{m}$. N values of thin film have been calculated as $0.58 \times 10^{16} \text{ m}^{-2}$ (Table 2). The large crystal size relative to film thickness which causes the crystalline number to be somewhat small.

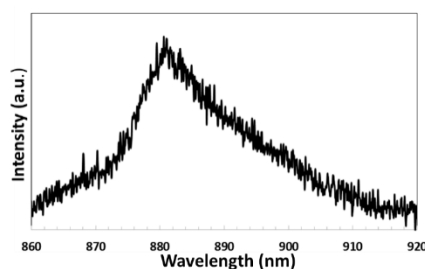
Table 2. Crystalline size, dislocation density, micro-strain, and crystalline number of CTS thin film

Sample	Crystalline Size (nm)	Dislocation density $\times 10^{16}$ (lines/m ²)	Micro-strain $\times 10^{-3}$	Crystalline Number $\times 10^{16}$ (m ²)
CTS	55.56	3.24	0.65	0.58

Raman spectrum in Figure 1b indicates that phase structures formed in CTS thin film in the 200-450 nm wavelength range. The monoclinic Cu₂SnS₃ (254 cm⁻¹ [19], 291 cm⁻¹[2], 372 cm⁻¹ [2]), tetragonal Cu₂SnS₃ (319 cm⁻¹ and 351 cm⁻¹[2]) and SnS phase (224 cm⁻¹) formations have been occurred in CTS thin film. Due to dominant peaks on 319 cm⁻¹ and 291cm⁻¹, it can be stated that CTS thin film is predominantly tetragonal phase structure which is compatible with the XRD pattern.

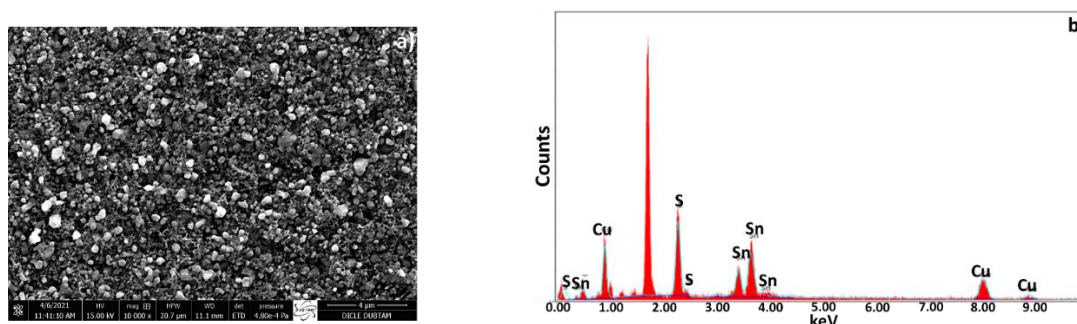
3.2. Photoluminescence Analyses

Photoluminescence (PL) is based on the principle that electrons are excited to upper energy levels by absorbing light incident on thin film, and then electron emits photons when it relaxes to a lower energy level. PL spectra of CTS thin film are presented in Figure 2. CTS thin film exhibits emission between 860 nm and 920 nm and PL has occurred at 1.40 eV (881 nm) under excitation. This energy is slightly above its band gap. Furthermore, PL formation of about 1.4 eV leading an increase in J_{sc} and power conversion efficiency in the solar cell.

**Figure 2.** PL spectrum of CTS thin film

3.3. Morphologic and EDX Analyses

According to the SEM image in Figure 3a, CTS thin film consists of dense particles and particle size is a distribution between 300-500 nm indicating non-homogeneous particle size distribution.

**Figure 3.** SEM image and EDX spectrum of CTS thin film

As seen in the EDX spectrum given in Figure 3b and Table 3, CTS thin film is Cu-poor and Sn-rich. Copper vacancies (V_{Cu}), which act like acceptor defects, enhance the p-type conductivity of CTS thin film and improve the efficiency of the solar cell. However, when Sn atoms occupy V_{Cu} vacancies [20, 21], Sn_{Cu} donor defects form which can act as a recombination centre, and increase n-type

conductivity. In addition, the amount of elemental sulphur is high because the thin film is annealed under sulphur flux for a long time and at a high temperature.

Table 3. The atomic weight rates of elements in CTS thin film

Sample	Cu(%)	Sn(%)	S(%)	Cu/Sn	S/metal
CTS	25.65	15.25	59.10	1.68	1.44

3.4. Optical Analyses

The light absorbance of CTS thin film is decreased slightly towards to near-infrared region, as shown in Figure 4a. However, it showed a similar absorbance in visible and near-infrared regions. Tauc equation denoted by Eq. (8) that is used to obtain band gap of thin film:

$$\alpha h\nu = A(h\nu - E_g)^{1/2} \quad (8)$$

where $h\nu$ is photon energy, E_g is thin film energy band gap, A is a constant. E_g is obtained by a straight line of $(\alpha h\nu)^2$ versus $(h\nu)$ in Tauc plot in Figure 4b. CTS thin film's band gap has been determined to be 1.12 eV. This value proves that thin film absorbs a high number of photons in longer wavelength regions and is compatible with a band gap of Cu_2SnS_3 given in the literature [22].

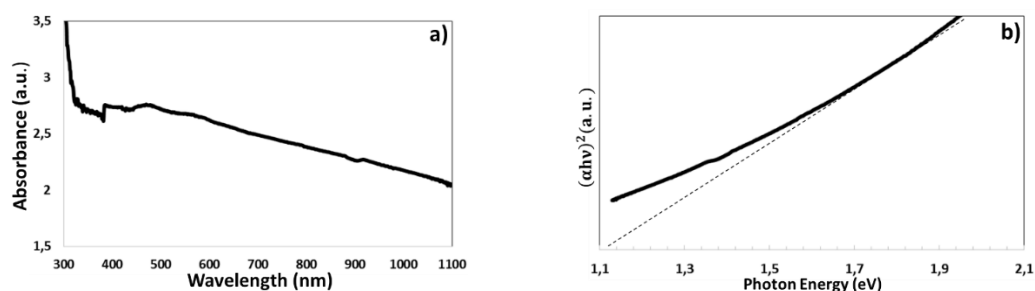


Figure 4. a) Absorption spectra and b) Tauc plot of CTS thin film

The thin film's absorption coefficient is determined by Eq. (9):

$$\alpha = 2.303(A/T) \quad (9)$$

T is the thickness of thin film and A is the absorbance of material. As expressed in the spectrum sketched in Fig. 5, CTS thin film has an absorption coefficient greater than $5.5 \times 10^4 \text{ cm}^{-1}$ in the visible region and this result is compatible with Cu_2SnS_3 absorption coefficients reported in the literature [1]. It has been observed that the absorption coefficient decreases towards to near-infrared region.

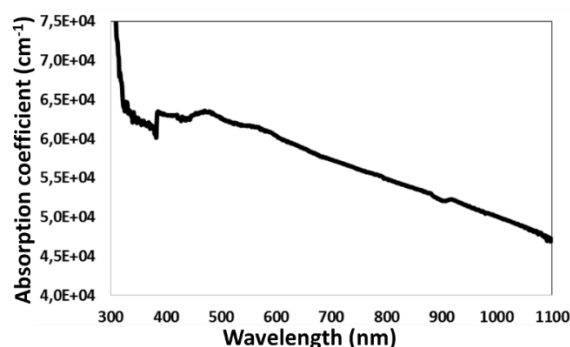


Figure 5. Absorption coefficient spectrum of CTS thin film

3.5. SCAPS-1D Simulation Program

3.5.1 Simulation of Mo/CTS/CdS/AZO/Al thin film solar cell

Absorber layers of solar cells, such as CTS, significantly affect power conversion efficiency. In many studies reported in the literature, only one layer of the solar cell was experimentally produced and the efficiency of the solar cell was determined by the physical parameters of that layer [15, 25, 26]. In this study, CTS thin film was determined to be the most ideal thin film depending on crystal structure and minimum defect conditions in CTS thin films.

Table 4. The physical parameters used in the modelling of Mo/CTS/CdS/AZO/Al solar cell

Layers	AZO [23]	CdS [24]	CTS [23]
Band Gap (eV)	3.3	2.4	1.12
Electron affinity (eV)	4.6	4.4	4.5
Dielectric permittivity (relative)	9	10	10
CB effective density of states (cm ⁻³)	2.20x10 ¹⁸	1.80x10 ¹⁸	2.20x10 ¹⁸
VB effective density of states (cm ⁻³)	1.80x10 ¹⁹	2.40x10 ¹⁹	1.80x10 ¹⁹
Electron/Hole thermal velocity (cm/s)	1.00x10 ⁷	1.00x10 ⁷	1.00x10 ⁷
Electron/Hole mobility (cm ² /Vs)	100/25	100/25	100/25
Shallow donor density (cm ⁻³)	1.00x10 ²⁰	1.00x10 ¹⁸	0
Shallow acceptor density (cm ⁻³)	0	0	1.00x10 ¹⁶
Thickness	200 nm	50 nm	1 μm
Contacts	Back Contact (Mo)	Front Contact (Al)	
Metal work function (eV)	5.00	4.08	
Surface recombination velocity of electrons (cm/s)	1x10 ⁷	1x10 ⁵	
Surface recombination velocity of holes (cm/s)	1x10 ⁵	1x10 ⁷	

Therefore, we have formed Mo/CTS/CdS/AZO/Al solar cell structure based on CTS thin film absorber layer (in Figure 6), using SCAPS-1D program. The absorption coefficient spectrum file (shown in Figure 5) with 1 μm thickness and 1.12 eV band gap of CTS thin film was processed by SCAPS-1D simulation. Since Aluminium has a low work function, Al metal contact is preferred due to the possibility of exhibiting ohmic behaviour for the AZO semiconductor. We have calculated and interpreted PV performance depending on interface defect density, radiative recombination, Auger recombination, and operation temperature (parameters significantly change the efficiency) of Mo/CTS/CdS/AZO/Al the solar cell. Theoretically calculated results have been given below. Thus, by taking basic parameters of other layers for the simulated structures, the PV parameters of the solar cell are determined. This will provide a reliable and accurate path for the experimental operation of this type of solar cell. Physical parameters of layers forming CTS the solar cell in our model are given in Table 4.

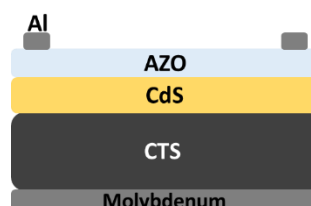


Figure 6. Mo/CTS/CdS/AZO/Al modelled by SCAPS-1D simulation

3.5.2 The effect of defect density (N_t) at the interface CTS/CdS of the solar cell

A high density of defect points can be localised at the interface between CTS and CdS layers leading to recombination centres [27]. Neutral defects can also occur at the interface of the second phase. The neutral defects acting as centres of Shockley-Read-Hall (SHR) recombination cause a certain decrease in the efficiency of the solar cell. These defects, located close to band edges, contribute to SHR recombination since the carrier is likely to return to its respective bands for shallow levels. Besides these, neutral defects can also be caused by lattice mismatch of CTS and CdS semiconductors in contact with each other [28, 29]. PV parameters of CTS solar cell versus interfacial neutral defect density (in 10^{10} and 10^{18} cm^{-3}) are given in Figure 7. According to these curves, V_{OC} and I_{SC} PV parameters of CTS the solar cell decreased after 1.10^{13} cm^{-3} of neutral defect densities.

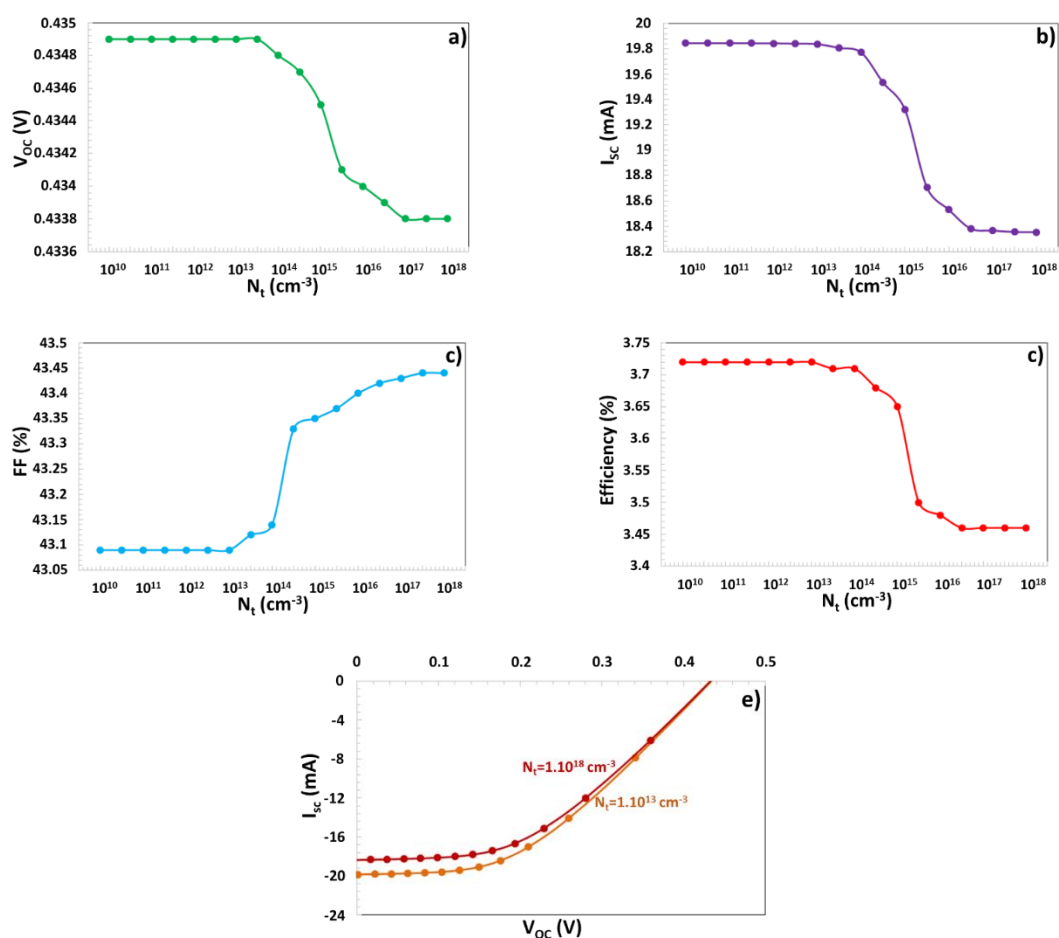


Figure 7. a) V_{oc} , b) I_{sc} , c) FF, d) Efficiency curves and e) I_{sc} depending on the interfacial defect density (N_t (cm^{-3})) at CTS/CdS of the solar cell.

Power conversion efficiency (shown in Figure 7e) of the solar cell for 1.10^{13} cm^{-3} defect density is 3.72 %. As seen in Figure 7d, after a neutral defect density of 1.10^{13} cm^{-3} , there was a sudden drop in the efficiency of the CTS solar cell. It has been noticed that the efficiency of the solar cell has remained constant at 3.46 % between 1.10^{17} and 1.10^{18} cm^{-3} of defect density [30]. As a result, neutral defect density should not be less than 1.10^{13} cm^{-3} . Therefore, it has been concluded that there is no reduction in power conversion efficiency.

3.5.3 Recombination mechanism for Mo/CTS-A2/CdS/AZO/Al solar cell

The recombination mechanism consists of three types of recombination radiative recombination, Auger recombination, and SRH recombination. These recombination mechanisms have a great influence on the PV performance of multilayer solar cells. In this study, the radiative recombination coefficient and Auger coefficient were evaluated. When an electron in the conduction band is transferred to the valence band, it emits a photon. The recombination of electrons and holes in this process is expressed as radiative recombination [31]. The efficiency spectra of the CTS solar cell depending on radiative recombination coefficient (Br (cm^3/s)) is given in Figure 8a and efficiency remains almost constant between 10^{-12} and 10^{-8} cm^3/s , it drops abruptly with 10^{-8} cm^3/s . For efficiency not to decrease, the Br value must be less than 10^{-8} cm^3/s . Auger recombination is a non-radiative event, which has a large effect on small band gap semiconductors.

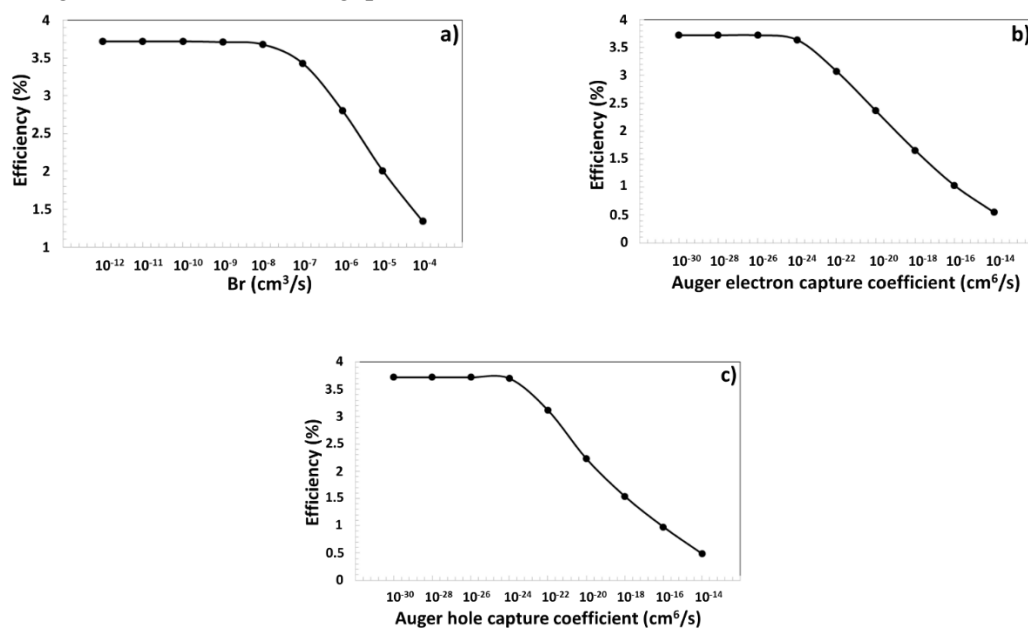


Figure 8. The efficiency curve of CTS solar cell depends on a) radiative recombination coefficient (Br), b) Auger electron and c) hole capture coefficient

When an electron and hole recombine with excess energy, an electron rises to the conduction band, or the hole transitions deeper into the valence band, but no light is produced [32, 33]. This process is known as Auger recombination. As seen in Figure 8b and 8c, when Auger electron and hole capture coefficients increase from 10^{-26} to 10^{-14} cm^6/s and 10^{-24} to 10^{-14} cm^6/s , respectively, efficiency values decrease. Therefore, these values should not be exceeded in order to avoid a significant decrease in the efficiency of the solar cell.

3.5.4 The effect of the operating temperature on CTS solar cell

Operation temperature adversely affects the performance of solar cells due to PV characteristics based on operation temperature between 240 °K and 400 °K in Figure 9, V_{OC} and FF values of CTS solar cell decreases as operation temperature increases. So, with increasing operation temperature, the band gap of the semiconductor decreases. In other words, the crystal lattice of the thin film broadens and the interatomic bonds are weakened. Weak bonds between atoms express that very low energy is required to break a bond and take an electron from the conduction band. Thus, the recombination rate of electron-hole pair between conduction and valence band increases. It limits access of minority charge carriers to

the depletion region. Moreover, an increase in dark current causes an increment in leakage current and reduces the V_{OC} value [23, 34-36]. Furthermore, the energy of carriers increases even more and they become unstable as operation temperature increases. Therefore, carriers undergo recombination before they can reach the depletion region, this case reduces I_{SC} and V_{OC} values [36]. As a result, an increment in operation temperature deteriorates the performance of the solar cell. The efficiency of the solar cell was calculated to be 3.72 % for room temperature (300 K) [37-39].

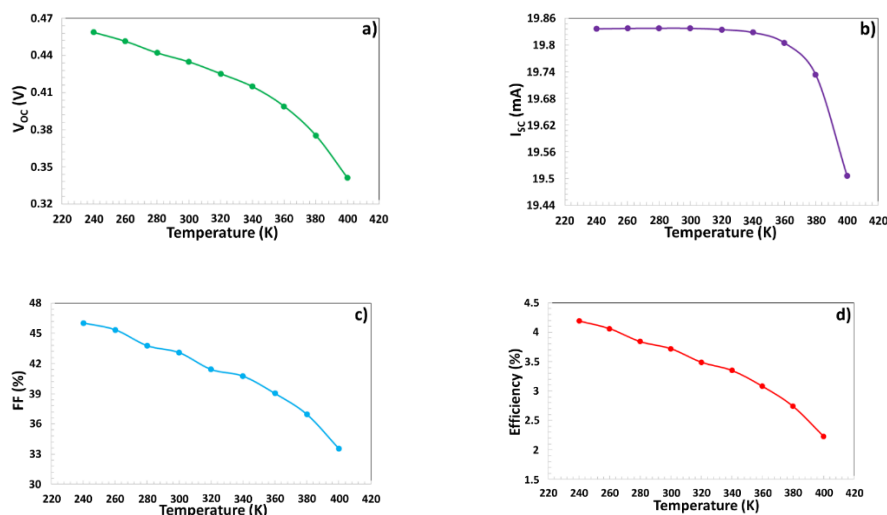


Figure 9. Effect of the operating temperature on a) V_{OC} , b) I_{SC} , c) FF, and d) efficiency parameters of CTS solar cell

4. Conclusion

CTS thin films were produced for 30 and 40 sccm sulphur flux rates in 15, 30, and 60 minutes annealing time durations at a constant 550 °C temperature. CTS thin film has been formed in tetragonal in Cu_2SnS_3 crystalline structure. Crystalline size, dislocation density, microstrain, and the crystalline number of CTS structure have been calculated to be 55.56 nm, 3.24×10^{16} lines/m², 0.65×10^{-3} , and 0.58×10^{16} m⁻², respectively. CTS thin film consists of particles with dense and inhomogeneous size distribution. CTS thin film is Cu-poor and Sn rich, which has a band gap of 1.12 eV.

Mo/CTS/CdS/AZO/Al solar cell based on CTS layer was modelled using SCAPS-1D software. V_{OC} and I_{SC} PV parameters of CTS the solar cell were decreased with 10^{13} cm⁻³ of neutral defect density. Efficiency corresponding to this defect density is 3.72 %. Radiative recombination coefficient and Auger electron/hole capture recombination coefficient have been calculated: radiative recombination coefficient dropped abruptly beyond 10^{-8} cm³/s value. For efficiency not to decrease, the B_r value must be higher than 10^{-8} cm³/s. When Auger electron and hole capture coefficients increase from 10^{-26} to 10^{-14} cm⁶/s and 10^{-24} to 10^{-14} cm⁶/s, respectively, efficiency values decrease. As the operation temperature increases, the V_{OC} and FF of the solar cell decrease. CTS solar cell shows an efficiency value of 3.72 % at room temperature.

Acknowledgments

The authors wish to kindly thank; Dr. Marc Burgelman's group, the University of Gent, Belgium for providing the SCAPS-1D simulation program. Selcuk University Scientific Research Project (BAP) Coordination for the support with the number 15201070 and 19401140 projects, Selçuk University, High Technology Research and Application Centre (İL-TEK), and SULTAN Centre for infrastructure. Dicle

University Scientific Research Project (BAP) Coordination for the support with the number FEN.18.007 project,

Ethical Statements

The author declares that this document does not require an ethics committee approval or any special permission. Our study does not cause any harm to the environment.

Conflict of interest

The authors declare no conflict of interest.

Authors Contributions

SYG carried out calculations and wrote the first draft of the manuscript. IC and SB carried out the experiments. HSK supervised the projects. All authors discussed the results and contributed to the final manuscript.

References

- [1] S. Rahaman, M. K. Singha, M. A. Sunil, and K. Ghosh, "Effect of copper concentration on CTS thin films for solar cell absorber layer and photocatalysis applications," *Superlattices and Microstructures*, 145, 106589, 2020.
- [2] V. R. M. Reddy *et al.*, "Review on Cu₂SnS₃, Cu₃SnS₄, and Cu₄SnS₄ thin films and their photovoltaic performance," *Journal of Industrial and Engineering Chemistry*, 76, 39-74, 2019.
- [3] M. Umehara, Y. Takeda, T. Motohiro, T. Sakai, H. Awano, and R. Maekawa, "Cu₂Sn_{1-x}GexS₃ (x= 0.17) thin-film solar cells with high conversion efficiency of 6.0%," *Applied Physics Express*, 6(4), 045501, 2013.
- [4] A. Kanai and M. Sugiyama, "Na induction effects for J–V properties of Cu₂SnS₃ (CTS) solar cells and fabrication of a CTS solar cell over-5.2% efficiency," *Solar Energy Materials and Solar Cells*, 231, 111315, 2021.
- [5] J. Zhou, L. You, S. Li, and Y. Yang, "Preparation and characterization of Cu₂ZnSnS₄ microparticles via a facile solution route," *Materials Letters*, 81, 248-250, 2012.
- [6] Z. Seboui, A. Gassoumi, and N. Kamoun-Turki, "Evolution of sprayed Cu₂ZnSnS₄," *Materials science in semiconductor processing*, 26, 360-366, 2014.
- [7] K. Tanaka, Y. Fukui, N. Moritake, and H. Uchiki, "Chemical composition dependence of morphological and optical properties of Cu₂ZnSnS₄ thin films deposited by sol-gel sulfurization and Cu₂ZnSnS₄ thin film solar cell efficiency," *Solar Energy Materials and Solar Cells*, 95(3), 838-842, 2011.
- [8] K. Woo, Y. Kim, and J. Moon, "A non-toxic, solution-processed, earth-abundant absorbing layer for thin-film solar cells," *Energy & Environmental Science*, 5(1), 5340-5345, 2012.
- [9] Y. Wang and H. Gong, "Cu₂ZnSnS₄ synthesized through a green and economic process," *Journal of alloys and compounds*, 509(40), 9627-9630, 2011.
- [10] S. Rabaoui, H. Dahman, N. Ben Mansour, and L. El Mir, "Structural, optical and electrical properties of Cu₂SnS₃ nanoparticles synthesized by simple solvothermal technique," *Journal of Materials Science: Materials in Electronics*, 26(2), 1119-1124, 2015.
- [11] A. C. Piñón Reyes *et al.*, "Study of a lead-free perovskite solar cell using CZTS as HTL to achieve a 20% PCE by SCAPS-1D simulation," *Micromachines*, 12(12), 1508, 2021.

- [12] T. AlZoubi, A. Moghrabi, M. Moustafa, and S. Yasin, "Efficiency boost of CZTS solar cells based on double-absorber architecture: Device modeling and analysis," *Solar Energy*, 225, 44-52, 2021.
- [13] A. Houimi, S. Y. Gezgin, B. Mercimek, and H. Ş. Kılıç, "Numerical analysis of CZTS/n-Si solar cells using SCAPS-1D. A comparative study between experimental and calculated outputs," *Optical Materials*, 121, 111544, 2021.
- [14] M. Sreejith, D. Deepu, C. S. Kartha, K. Rajeevkumar, and K. Vijayakumar, "Tuning the properties of sprayed CuZnS films for fabrication of solar cell," *Applied physics letters*, 105(20), 202107, 2014.
- [15] Y. Khaissa *et al.*, "Experimental and numerical simulation of deposition time effect on ZnS thin films for CZTS-based solar cells," *Optical and Quantum Electronics*, 53(9), 1-21, 2021.
- [16] M. Burgelman, K. Decock, A. Niemegeers, J. Verschraegen, and S. Degrave, "SCAPS manual," ed: February, 2016.
- [17] P. K. Kalita, B. Sarma, and H. Das, "Structural characterization of vacuum evaporated ZnSe thin films," *Bulletin of Materials Science*, 23(4), 313-317, 2000.
- [18] S. Prabahar and M. Dhanam, "CdS thin films from two different chemical baths—structural and optical analysis," *Journal of Crystal Growth*, 285(1-2), 41-48, 2005.
- [19] T. Raadik *et al.*, "Temperature-dependent photoreflectance study of Cu₂SnS₃ thin films produced by pulsed laser deposition," *Applied Physics Letters*, 110(26), 261105, 2017.
- [20] P. Zhao and S. Cheng, "Influence of sulfurization temperature on photoelectric properties Cu₂SnS₃ thin films deposited by magnetron sputtering," *Advances in Materials Science and Engineering*, 2013, 2013.
- [21] E. Hossain *et al.*, "Effects of sulfurization temperature on structural, morphological, and optoelectronic properties of CTS thin films solar cells," *Chalcogenide Letters*, 15(10), 499-507, 2018.
- [22] D. Tiwari, T. K. Chaudhuri, T. Shripathi, U. Deshpande, and R. Rawat, "Non-toxic, earth-abundant 2% efficient Cu₂SnS₃ solar cell based on tetragonal films direct-coated from single metal-organic precursor solution," *Solar Energy Materials and Solar Cells*, 113, 165-170, 2013.
- [23] A. D. Adewoyin, M. A. Olopade, O. O. Oyebola, and M. A. Chendo, "Development of CZTGS/CZTS tandem thin film solar cell using SCAPS-1D," *Optik*, 176, 132-142, 2019.
- [24] B. Barman and P. Kalita, "Influence of back surface field layer on enhancing the efficiency of CIGS solar cell," *Solar Energy*, 216, 329-337, 2021.
- [25] M. A. Shafi *et al.*, "Optimization of Electrodeposition Time on the Properties of Cu₂ZnSnS₄ Thin Films for Thin Film Solar Cell Applications," 2021.
- [26] N. Khemiri, S. Chamekh, and M. Kanzari, "Properties of thermally evaporated CZTS thin films and numerical simulation of earth-abundant and non toxic CZTS/Zn (S, O) based solar cells," *Solar Energy*, 207, 496-502, 2020.
- [27] L. Et-taya, T. Ouslimane, and A. Benami, "Numerical analysis of earth-abundant Cu₂ZnSn (S_xSe_{1-x})₄ solar cells based on Spectroscopic Ellipsometry results by using SCAPS-1D," *Solar Energy*, 201, 827-835, 2020.

- [28] A. Srivastava, P. Dua, T. Lenka, and S. Tripathy, "Numerical simulations on CZTS/CZTSe based solar cell with ZnSe as an alternative buffer layer using SCAPS-1D," *Materials Today: Proceedings of*, 43, 3735-3739, 2021.
- [29] S. Meher, L. Balakrishnan, and Z. Alex, "Analysis of Cu₂ZnSnS₄/CdS based photovoltaic cell: a numerical simulation approach," *Superlattices and Microstructures*, 100, 703-722, 2016.
- [30] A. Mohandes, M. Moradi, and H. Nadgaran, "Numerical simulation of inorganic Cs₂AgBiBr₆ as a lead-free perovskite using device simulation SCAPS-1D," *Optical and Quantum Electronics*, 53(6), 1-22, 2021.
- [31] V. Raj, F. Rougieux, L. Fu, H. H. Tan, and C. Jagadish, "Design of Ultrathin InP Solar Cell Using Carrier Selective Contacts," *IEEE Journal of Photovoltaics*, 10(6), 1657-1666, 2020.
- [32] H. Fu and Y. Zhao, "Efficiency droop in GaInN/GaN LEDs," in *Nitride Semiconductor Light-Emitting Diodes (LEDs)*: Elsevier, 299-325, 2018.
- [33] F. Staub, U. Rau, and T. Kirchartz, "Statistics of the Auger recombination of electrons and holes via defect levels in the band gap—application to lead-halide perovskites," *ACS Omega*, 3(7), 8009-8016, 2018.
- [34] P. Roy, S. Tiwari, and A. Khare, "An investigation on the influence of temperature variation on the performance of tin (Sn) based perovskite solar cells using various transport layers and absorber layers," *Results in Optics*, 4, 100083, 2021.
- [35] M. Abderrezek, M. Fathi, and F. Djahli, "Comparative study of temperature effect on thin film solar cells," 2018.
- [36] H. Zhang, S. Cheng, J. Yu, H. Zhou, and H. Jia, "Prospects of Zn (O, S) as an alternative buffer layer for Cu₂ZnSnS₄ thin-film solar cells from numerical simulation," *Micro & Nano Letters*, 11(7), 386-390, 2016.
- [37] L. I. Nykyruy et al. "Evaluation of CdS/CdTe thin film solar cells: SCAPS thickness simulation and analysis of optical properties." *Optical Materials*, 92, 319-329, 2019.
- [38] A. D. Adewoyin, et al. "Development of CZTGS/CZTS tandem thin film solar cell using SCAPS-1D." *Optik*, 176, 132-142, 2019.
- [39] Zyoud, Samer H., et al. "Numerical modeling of high conversion efficiency FTO/ZnO/CdS/CZTS/MO thin film-based solar cells: Using SCAPS-1D software." *Crystals*, 11(12), 1468, 2021.